Numerical Study on Flame-Wall Interaction in Gas and Spray Combustion

Reo Kai

2022

Numerical Study on Flame-Wall Interaction in Gas and Spray Combustion

Reo Kai

A thesis submitted to Kyoto University
for the degree of Doctor of Philosophy in Engineering

2022

Acknowledgments

The research described in this thesis was carried out in the Department of Mechanical Engineering and Science at Kyoto University's Graduate School of Engineering, under the supervision of Professor Ryoichi Kurose. The author would like to express his most heartfelt gratitude to the professor for all the helpful suggestions to his study, and constant encouragement.

The author gives his thanks to Professor Kazuyoshi Nakabe and Professor Hiroshi Iwai for many valuable and critical comments to his study.

The author is deeply grateful to Professor Abhishek Lakshman Pillaii for the helpful discussions and suggestions for his study, and encouragement.

The author thanks Professor Mitsuhiro Matsumoto and Professor Hidenobu Wakabayashi for the many useful comments to his research.

The author is deeply grateful to Mr. Ryo Masuda, Mr. Takato Ikedo, Mr. Kazuhisa Inagaki of Toyota Central Research and Development Labs. for the helpful discussions and practical advice for his research.

The author is deeply grateful to Professor Nilanjan Chakraborty and Dr. Umair Ahmed of Newcastle University for the helpful discussions and constructive suggestions for his research.

The author thanks Mr. Takuya Murata and Mr. Azusa Takahashi for their help in his research.

The author feels gratitude to the past and present members of Thermal Science and Engineering Laboratory.

This research was partially supported by MEXT (Ministry of Education, Culture,

Sports, Science and Technology) as "Priority issue on Post-K computer" (Accelerated Development of Innovative Clean Energy Systems), by MEXT (Ministry of Education, Culture, Sports, Science and Technology) as "Program for Promoting Researches on the Supercomputer Fugaku" (Digital Twins of Real World's Clean Energy Systems with Integrated Utilization of Super-simulation and AI), and by MEXT Grant in Aid (No.19H02076). The author is also grateful to Mori Manufacturing Research and Technology Foundation for the financial support.

Finally, the author would like to express the deepest appreciation to his parents for the infinite support and constant affection.

Contents

Chapter 1

Introduction

1.1 Background and motivation for this study

According to the United Nations Environment Programme (UNEP) annual emissions gap report [1], global greenhouse gas emissions should be cut drastically in the next decade to limit the adverse consequences of climate change. Therefore, to mitigate the challenges of climate change, it is necessary to suppress the anthropogenic CO_2 emissions, most of which arise from the burning of fossil fuels. In this regard, many governments across the globe are expected to set ambitious new commitments to slash their CO_2 emissions, as part of the 2015 Paris Agreement [2] at the 21st Conference of the Parties (COP21) to the United Nations Framework Convention on Climate Change (UNFCC). However, all energy outlooks [3, 4] acknowledge that combustion will play an indispensable role in the energy sector for the foreseeable future. Therefore, it is strongly required to reduce the CO_2 emissions from combustion devices, such as automobile engines, jet engines, gas turbine engines, and furnaces. This means that it is strongly required to increase the thermal efficiency for these combustion devices. In these combustion devices, combustion generally takes place in a combustion chamber, in which flames interact with walls. Such flame-wall interaction (FWI) has a strong effect on the overall thermal efficiency of combustion devices, because the heat loss through the chamber wall is one of the main causes of thermal efficiency deterioration. Therefore,

the fundamental physical understanding of the FWI plays a pivotal role in the design of modern combustors.

For turbulent flames, which are often formed in practical combustion devices, FWI includes coupling phenomena between walls and turbulence, and between flames and turbulence. The outline of the interactions between flames, walls, and turbulence is explained as follows [5]. The wall is heated by the flames, while the flames in the vicinity of the wall are strongly affected by the heat flux through the wall, which leads to flame quenching. Moreover, the flames modify the flow field near the wall, which in turn influences the wall heat flux [5]. Hence, in the combustor, the presence of walls generates the wall turbulence and alters the turbulence structure, which is further affected by the presence of the flame near the wall [6]. However, the detailed information on the behavior of turbulence and combustion processes during FWI is limited, and consequently, the modeling is currently in its infancy.

There are many experimental and numerical studies on the FWI for laminar and turbulent flames. These studies have mainly investigated the wall heat flux behavior, which influences not only the improvement of the thermal efficiency but also the lifetime of the combustor, flame quenching in the vicinity of the wall, pollutant formation from flames in the vicinity of the wall, the development of turbulent combustion model for the near-wall region, and flashback.

To improve the thermal efficiency by reducing the heat loss through the wall, many studies (e.g. [7, 8]) have investigated the use of ceramic materials with a low thermal conductivity for heat insulation, such as Zirconia, especially for automobile engines. Because the surface temperature on such insulation walls is kept high, the gas temperature gradient on the insulation wall becomes low, which reduces the cooling loss. Although such insulations can reduce the cooling loss, during the intake and compression strokes, the unburnt gas temperature increases owing to the high wall surface temperature. This causes an increase in the NOx emissions and knocking leading to the destruction of the engine [9]. To overcome these problems, new insulation materials with lower thermal conductivity and volumetric heat capacity than the conventional ones have been

developed [9–11]. Because the surface temperature changes easily depending on the gas temperature owing to the low volumetric heat capacity, the surface temperature increases when the flame hits the wall, and remains low during the intake and compression strokes. The effectiveness of such new insulation materials on the reduction in the heat loss through the wall have been confirmed experimentally and numerically [9–12]. However, its detailed temporal behavior, and the effects of fuel composition and ambient pressure on the reduction in wall heat flux have not been investigated, despite of their importance.

In addition to the wall properties, the flow field also affects the FWI, as mentioned above. To understand the FWI under a statistically steady-state within the turbulent boundary layer, wall interaction of turbulent premixed V-shaped flame in the turbulent boundary layer has also been analyzed [21–24] where the flames obliquely interact with walls. Jainski et al. [25] measured the flame surface density (FSD), which is an important quantity for turbulent reaction model, from experimental data for the FWI of turbulent V-shaped methane-air flame. Kosaka et al. [26] experimentally investigated the correlations between local heat release rate, flame curvature, and wall-normal quenching distance for the FWI of V-shaped methane- and dimethyl ether-air flames. Zentgraf et al. [27] experimentally investigated the correlations between CO and CO_2 and temperature near the wall for V-shaped dimethyl ether-air FWI. In numerical studies, in contrast, Alshaalan and Rutland [6, 28] performed direct numerical simulation (DNS) of turbulent-channel-Couette flow at $Re_\tau = 38$ and investigated the effect of streamwise vortices on wall heat flux, and the statistical behaviors of turbulent scalar flux and FSD; moreover they proposed modifications to the mean reaction closure. Gruber et al. [22] carried out three-dimensional complex chemistry DNS of turbulent V-shaped hydrogen-air flame interaction with isothermal inert walls to analyze the flame structure and flame propagation in the near-wall region along the statistical behavior of the wall heat release rate. Ahmed et al. [23] performed three-dimensional DNS of V-flame in the turbulent channel flow at $Re_\tau = 110$ interacting with adiabatic and isothermal inert walls and demonstrated the effects of wall boundary condition on the surface density

function (SDF) evolution in boundary layer during premixed FWI. Ahmed et al. [21] assessed the applicability of Bray-Moss-Libby formulation for oblique quenching of turbulent V-shaped premixed flames and for statistically planar premixed flame propagation across the turbulent boundary layer toward an inert isothermal wall. Jiang et al. [24] performed three-dimensional DNS of V-flame in turbulent channel flow interacting with two different isothermal walls and investigated CO formation near the wall. Although all the analyses provided significant physical and modeling insights for turbulent premixed FWI, these studies were conducted for moderate values of friction Reynolds number (i.e., $Re_\tau < 180$) and thus it is necessary to analyze the fundamental aspects of FWI in turbulent boundary layers for higher values of Re_τ.

It is also important to investigate the FWI for turbulent spray flames, which are observed in the actual engines such as compression ignition (CI) engines and jet engines, in addition to FWI for gas flames. Some studies have investigated the relationship between Reynold number Re and wall heat flux especially for under CI engine-like conditions. If the heat loss through the combustion chamber wall could be accurately predicted in the early design stages, then the optimal combustion conditions for reducing heat loss can be devised, thereby achieving significant savings in the engine design cycle time. Normally, heat loss through the wall in IC engines is estimated based on the principle of convective heat transfer, where the dimensionless average Nusselt number Nu (corresponding to the average heat flux at the wall surface assuming quasi-steady state conditions) is a function of two other dimensionless parameters, that is the Reynolds number Re and the Prandtl number Pr. In this regard, since the 20th century, many researchers have performed IC engine experiments, using both spark ignition (SI) and compression ignition (CI) engines [13–18], and empirical equations/correlations (derived from their experimental data) of the form $Nu \propto Re^n$ have been proposed. Some researchers have proposed values for the correlation index n based on the experiments, such as Oguri ($n = 0.5$) [14], Annand ($n = 0.7$) [15], Sitkei and Ramanaiah ($n = 0.7$) [17], Hohenberg [18] ($n = 0.8$), Inagaki et al. [19] ($n = 0.4$), Mahmud et al. [20] ($n = 0.8$). Hence, it is evident from the above-mentioned experimental investigations that, there is an appreciable variation

in the proposed value of the correlation index n, indicating the lack of a clear consensus on the relation between Nu and Re corresponding to wall heat loss during spray FWI process.

Therefore, in this study the FWI characteristics of laminar premixed flame, turbulent premixed flame, and turbulent spray flame have been investigated using numerical simulations without any turbulence model. The aim is to attain further understanding of the FWI characteristics under various combustion conditions. First, the influence of wall material on the premixed FWI is investigated. Numerical simulations of premixed flames propagating toward two different types of walls, i.e., insulation wall and Al alloy wall, are performed while incorporating conjugate heat transfer to investigate how the insulation material reduces the wall heat flux. The effects of fuel composition and ambient pressure on the reduction of the wall heat flux are also investigated. Second, the influence of turbulence on the premixed FWI is investigated. A three-dimensional DNS of turbulent premixed V-flame interacting with an isothermal inert wall in a wall-bounded turbulent channel flow at $Re_\tau = 395$ for the stoichiometric methane-air flame is performed, and the statistics of near-wall SDF in a turbulent channel flow is investigated. Finally, the influence of turbulence on the spray FWI is investigated. DNS of n-dodecane spray flame impinging on the wall are performed for different injection velocity conditions to investigate the relationship between Re and Nu.

1.2 Thesis outline

This thesis consists of five chapters.

Chapter 1, the present chapter, describes the background and motivation for the study, and outline of this thesis.

Chapter 2 describes the characteristics of reduction in wall heat loss by heat insulation wall. The effects of fuel properties (C1 to C3 alkanes and H_2), equivalence ratios (ϕ = 0.6, 0.8, 1.0, and 1.2), and ambient pressure conditions (1, 2, and 4 MPa) on the reduction in the wall heat loss are investigated by one- and two- dimensional numerical simulations of propagating premixed flames incorporating conjugate heat transfer. For the simulations to investigate the effects of fuel and equivalence ratio, the detailed chemical reaction mechanisms that consider 70 chemical species and 321 reactions for the alkane combustion [29], and 9 chemical species and 19 reactions for H_2 combustion [30] are used. For the simulations to investigate the effect of pressure, a two-step global reaction model [31] is used to calculate the methane reaction.

Chapter 3 describes statistical behavior of the near-wall surface density function in a turbulent channel flow. A three-dimensional DNS of turbulent premixed V-flame interacting with an isothermal inert wall in the wall-bounded turbulent channel flow at $Re_\tau = 395$ for the stoichiometric methane-air flame is performed. For the calculation of the methane reactions, a two-step global reaction model [31] is used.

Chapter 4 describes the FWI for the spray flame impinging on the wall. The relationship between Re and Nu is investigated using DNS of n-dodecane spray flame impinging on the wall for different injection velocity conditions. As a turbulent combustion model, a non-adiabatic flamelet progress variable (NA-FPV) approach [32] is employed. For the generation of the flamelet database, a detailed chemical reaction mechanism consisting 255 chemical species and 2289 reactions [33] is considered to represent the n-dodecane reaction.

Chapter 5 summarizes all the investigations carried out in this study and recommendations for possible future extensions of the present study are provided.

References

[1] United Nations Environment Programme, 2019.

[2] United Nations Framework Convention on Climate Change, 2015.

[3] International Energy Agency, 2015.

[4] Annual Energy Outlook 2015 with projections to 2040. *U.S. Energy Information Administration*, DOE/EIA–0383(2015), 2015.

[5] T. Poinsot and D. Veynante. Theoretical and numerical combustion, 2005.

[6] T. M. Alshaalan and C. J. Rutland. Turbulence, scalar transport, and reaction rates in flame-wall interaction. In *Symposium (International) on Combustion*, volume 27, 793–799. Elsevier, 1998.

[7] W. Bryzik and R. Kamo. Tacom/cummins adiabatic engine program. *SAE transactions*, 1063–1087, 1983.

[8] K. Osawa, R. Kamo, and E. Valdmanis. Performance of thin thermal barrier coating on small aluminum block diesel engine. Technical report, SAE Technical Paper, 1991.

[9] Y. Wakisaka, M. Inayoshi, K. Fukui, H. Kosaka, Y. Hotta, A. Kawaguchi, and N. Takada. Reduction of heat loss and improvement of thermal efficiency by application of "temperature swing" insulation to direct-injection diesel engines. *SAE International Journal of Engines*, 9(3):1449–1459, 2016.

[10] H. Fujimoto, H. Yamamoto, M. Fujimoto, and H. Yamashita. A study on improvement of indicated thermal efficiency of ICE using high compression ratio and reduction of cooling loss. Technical report, SAE Technical Paper, 2011.

[11] H. Kosaka, Y. Wakisaka, Y. Nomura, Y. Hotta, M. Koike, K. Nakakita, and A. Kawaguchi. Concept of "temperature swing heat insulation" in combustion

chamber walls, and appropriate thermo-physical properties for heat insulation coat. *SAE International Journal of Engines*, 6(1):142–149, 2013.

[12] A. Kikusato, K. Jin, and Y. Daisho. A numerical simulation study on improving the thermal efficiency of a spark ignited engine—part 1: Modeling of a spark ignited engine combustion to predict engine performance considering flame propagation, knock, and combustion chamber wall—. *SAE International Journal of Engines*, 7(1):96–105, 2014.

[13] G. Eichelberg. Some new investigations on old combustion engine problems. *Engineering*, 148:446–463, 1939.

[14] T. Oguri. On the coefficient of heat transfer between gases and cylinder walls of the spark-ignition engine. *Bulletin of JSME*, 3:363–369, 1960.

[15] W. J. D. Annand. Heat transfer in the cylinders of reciprocating internal combustion engines. *Proceedings of the Institution of Mechanical Engineers*, 177:973–990, 1963.

[16] G. Woschni. A universally applicable equation for the instantaneous heat transfer coefficient in the internal combustion engine. In *SAE Technical Paper*. SAE International, 02 1967.

[17] G. Sitkei and G. V. Ramanaiah. A rational approach for calculation of heat transfer in diesel engines. In *SAE Technical Paper*. SAE International, 02 1972.

[18] G. F. Hohenberg. Advanced approaches for heat transfer calculations. In *SAE Technical Paper*. SAE International, 02 1979.

[19] K. Inagaki, J. Mizuta, and T. Hashizume. Theoretical study on spray design for small-bore-size diesel engines (fourth report). *Transactions of Society of Automotive Engineers of Japan*, 47:1297–1303 (in Japanese), 2016.

[20] R. Mahmud, T. Kurisu, K. Nishida, Y. Ogata, J. Kanzaki, and O. Akgol. Effects of injection pressure and impingement distance on flat-wall impinging spray flame and

its heat flux under diesel engine-like condition. *Advances in Mechanical Engineering*, 11:1–15, 2019.

[21] U. Ahmed, N. Chakraborty, and M. Klein. Assessment of bray moss libby formulation for premixed flame-wall interaction within turbulent boundary layers: Influence of flow configuration. *Combustion and Flame*, 233:111575, 2021.

[22] A. Gruber, R. Sankaran, E. Hawkes, and J. Chen. Turbulent flame–wall interaction: a direct numerical simulation study. *Journal of Fluid Mechanics*, 658:5–32, 2010.

[23] U. Ahmed, N. Chakraborty, and M. Klein. Scalar gradient and strain rate statistics in oblique premixed flame–wall interaction within turbulent channel flows. *Flow, Turbulence and Combustion*, 106(2):701–732, 2021.

[24] B. Jiang, D. Brouzet, M. Talei, R. L. Gordon, Q. Cazeres, and B. Cuenot. Turbulent flame-wall interactions for flames diluted by hot combustion products. *Combustion and Flame*, 230:111432, 2021.

[25] C. Jainski, M. Rißmann, B. Böhm, and A. Dreizler. Experimental investigation of flame surface density and mean reaction rate during flame–wall interaction. *Proceedings of the Combustion Institute*, 36(2):1827–1834, 2017.

[26] H. Kosaka, F. Zentgraf, A. Scholtissek, C. Hasse, and A. Dreizler. Effect of flame-wall interaction on local heat release of methane and dme combustion in a side-wall quenching geometry. *Flow, Turbulence and Combustion*, 104(4):1029–1046, 2020.

[27] F. Zentgraf, P. Johe, A. D. Cutler, R. S. Barlow, B. Böhm, and A. Dreizler. Classification of flame prehistory and quenching topology in a side-wall quenching burner at low-intensity turbulence by correlating transport effects with co2, co and temperature. *Combustion and Flame*, 111681, 2021.

[28] T. Alshaalan and C. J. Rutland. Wall heat flux in turbulent premixed reacting flow. *Combustion science and technology*, 174(1):135–165, 2002.

[29] "Chemical-Kinetic Mechanisms for Combustion Applications", San Diego Mechanism web page, Mechanical and Aerospace Engineering (Combustion Research), University of California at San Diego, `http://web.eng.ucsd.edu/mae/groups/combustion/sdmech/sandiego20161214/sandiego20161214_mechCK.txt` .

[30] M. Ó Conaire, H. J. Curran, J. M. Simmie, W. J. Pitz, and C. K. Westbrook. A comprehensive modeling study of hydrogen oxidation. *International journal of chemical kinetics*, 36(11):603–622, 2004.

[31] B. Franzelli, E. Riber, M. Sanjosé, and T. Poinsot. A two-step chemical scheme for kerosene–air premixed flames. *Combustion and Flame*, 157(7):1364–1373, 2010.

[32] A. Kishimoto, H. Moriai, K. Takenaka, T. Nishiie, M. Adachi, A. Ogawara, and R. Kurose. Application of a nonadiabatic flamelet/progress-variable approach to large-eddy simulation of H2/O2 combustion under a pressurized condition. *J. Heat Transfer*, 139:124501, 2017.

[33] K. Narayanaswamy, P. Pepiot, and H. Pitsch. A chemical mechanism for low to high temperature oxidation of n-dodecane as a component of transportation fuel surrogates. *Combustion and Flame*, 161:866–884, 2014.

Chapter 2

Conjugate heat transfer analysis of premixed flame-wall interaction

2.1 Introduction

In this chapter, heat flux through the wall is investigated by performing conjugate heat transfer analysis.

Global warming has been a critical issue in the world for several decades, and many countries have been asked to reduce their greenhouse gas emissions. In 2010, such emissions from the transport sector were reported to occupy 14% of the global greenhouse gas emissions produced by economic sector [1]. Hence, the reduction of CO_2 emission from automobile engines is inevitable. To improve the thermal efficiency of automobile engines, it is important to reduce the cooling loss of burnt gas outward through the engine cylinder wall. Recently, to achieve this, new insulations with lower thermal conductivity and volumetric heat capacity than the conventional insulations, such as Zirconium, and therefore easily change the wall surface temperature depending on the gas temperature, have been developed [2–4]. It is expected that such new insulations enhance the temperature increase of the wall surface when the flame approaches the wall, and make the magnitude of the gradient of the gas temperature on the wall gentle, which accordingly leads to suppress the heat loss through the wall. In addition, as these

advanced insulations tend to keep the wall surface temperature low during the intake and compression strokes, they are expected to reduce the NOx emissions and prevent knocking, which could lead to the destruction of the internal combustion engine [3].

In fact, the effects of the insulations on the heat transfer through the wall have been investigated experimentally and numerically [2–5]. Some previous experiments have verified that the temperature on the wall surface changes following the gas temperature, and the wall heat flux is reduced by the insulation [2, 3]. Also, Wakisaka et al. [3] numerically examined the effects of exhaust gas recirculation rate, injection timing, and surface roughness on the performance of the insulation. However, as they employed a wall model and did not focus on the detailed flame behavior near the wall, the reduction mechanism of the wall heat flux has not been well clarified yet.

To elucidate the flame-wall interaction (FWI) (e.g., [6–11]), in particular, the flame-"non-isothermal" wall interaction in detail, conjugate heat transfer (CHT) analysis, which solves the heat transfer both for the reactive fluid and solid wall, is useful. Mari et al. [6] performed the CHT analysis of a hydrogen/oxygen flame under supercritical pressure condition. They found that under such a high pressure condition, the increase in the wall temperature is not negligible and causes the quenching distance to decrease and the maximum wall heat flux to increase. Further, there also exist studies for methane/air premixed flame [7–9]. Shahi et al. [7] conducted numerical simulations of the heat transfer between oscillating methane/air partially premixed flame and the wall in the can type combustor with and without CHT analysis. They showed the importance of the CHT model to accurately predict the frequency of the unstable combustor mode. Moreover, some researchers carried out the numeircal simulartions of engine in–cylinder combustion with CHT analyses, and invesitigated heat transfer between reactive flow and chamber wall [10, 11]. However, there exist few studies in which the effect of the wall material on the flame behavior was investigated. Especially, no study has researched on the effects of pressure and turbulence on the heat flux on the insulation wall. Moreover, the effect of the equivalence ratio has not been investigated despite its importance. The equivalence ratio in sparked-ignition (SI) engines varies depending on

the engine load during driving, moreover, lean burn SI engines have been developed to achieve high thermal efficiency (e.g. [12–14]). In addition, the effects of fuel properties have not been well understood as well, although some hydrocarbon fuels were examined in the previous studies using different experimental and numerical setups. To reduce the pollutant emissions, H_2 has been considered as an alternative or additional fuel (e.g. [12, 14, 15]), which can also be used in HCCI (Homogeneous Charge Compression Ignition) engines (e.g. [16, 17]). The H_2 flame shows a high heat release rate in the vicinity of the wall, although the reaction rate of H_2 vanishes close to the wall [18]. Hence, it is also important to investigate the H_2 flame behavior in the vicinity of the insulation wall, as well as the hydrocarbon fuel flame behavior.

In this study, the CHT analyses of premixed flames propagating toward walls are performed without employing any wall model in terms of one- and two-dimensional (1D and 2D) numerical simulations, and the FWI is investigated in detail. In the 1D numerical simulations, the effects of wall material, i.e., the insulation and Al alloy, on the wall heat flux are investigated for different fuels (C1 to C3 alkanes and H_2) at different equivalence ratios ($\phi = 0.6$, 0.8, 1.0, and 1.2) under different ambient pressure conditions (1, 2, and 4 MPa). In the 2D numerical simulations, on the other hand, the effect of turbulence on the wall heat flux is investigated.

2.2 Effect of fuel composition

2.2.1 Numerical simulation

In this study, to investigate the effects of the equivalence ratio and fuel properties on heat flux through the insulation wall, CHT analyses of the premixed flame propagating toward the wall are performed in terms of one-dimensional numerical simulations. To simply treat the combustion in the engine cylinder numerically, one-dimensional numerical simulation is sometime applied (e.g. [19, 20]).

2.2.1.1 Governing equations

For the reactive flow calculation, the conservation equations of mass, momentum, energy and mass fractions of chemical species are solved as follows

$$\frac{\partial \rho}{\partial t} + \nabla \cdot (\rho \boldsymbol{u}) = 0, \tag{2.1}$$

$$\frac{\partial \rho \boldsymbol{u}}{\partial t} + \nabla \cdot (\rho \boldsymbol{u}\boldsymbol{u}) = -\nabla p + \nabla \cdot \boldsymbol{\tau}, \tag{2.2}$$

$$\frac{\partial \rho h}{\partial t} + \nabla \cdot (\rho h \boldsymbol{u}) = \frac{\partial p}{\partial t} + \boldsymbol{u} \cdot \nabla p + \boldsymbol{\tau} : \nabla \boldsymbol{u} + \nabla \cdot \left[\rho\alpha \left\{ \nabla h - \sum_k (h_k \nabla Y_k) \right\} - \rho \sum_k (h_k Y_k \boldsymbol{V_k}) \right], \tag{2.3}$$

$$\frac{\partial \rho Y_k}{\partial t} + \nabla \cdot (\rho Y_k \boldsymbol{u}) = -\nabla \cdot (\rho Y_k \boldsymbol{V_k}) + \rho \dot{\omega}_k, \tag{2.4}$$

along with the equation of state for ideal gas. Here, ρ is the density, $\boldsymbol{u}$ is the velocity, p is the pressure, $\boldsymbol{\tau}$ is the viscous stress tensor, h is the specific enthalpy, α is the thermal diffusivity, Y is the mass fraction, $\boldsymbol{V}$ is the diffusion velocity, and $\dot{\omega}$ is the reaction rate. The subscript k represents the species k. In the Eqs. (2.10) and (2.11), to consider the preferential diffusion effect, $\boldsymbol{V_k}$ is obtained by solving the following Stefan-Maxwell equation.

$$\nabla X_k = \sum_{j \neq k} \left\{ \frac{X_j X_k}{D_{jk}} (\boldsymbol{V_j} - \boldsymbol{V_k}) \right\}, \tag{2.5}$$

where X is the mole fraction and D_{jk} is the binary diffusion coefficient of species j into species k. In this study, C1 to C3 alkanes and H_2 are considered as a fuel. To describe the combustion reactions of alkanes and H_2, the UCSD mechanism (70 species and 318 reactions) [21] and the Conaire mechanism (9 species and 19 reactions) [22] are used, respectively.

For the calculation of heat conduction in the wall, unsteady heat equation is solved.

$$\rho_s c_s \frac{\partial T_s}{\partial t} = \nabla \cdot (\lambda_s \nabla T_s). \tag{2.6}$$

Here, c is the heat capacity, T is the temperature, λ is the thermal conductivity. The subscript s represents the solid wall. To couple these calculations, the wall surface temperature is obtained by considering heat balance on the gas wall interface without any wall model.

2.2.1.2 Computatioinal setup

Figure 2.12 shows the schematic of the computational domain. The domain is composed of gas and wall parts, and the origin is at the gas-wall interface. The length of the gas part is 2.55 mm and the thickness of the wall is 0.1 mm, which is same as the previous experiment [3]. To investigate the effects of fuel and equivalence ratio on the performance of heat insulation, C1 to C3 alkanes and H_2 are considered as a fuel, and simulations are performed under various equivalence ratio conditions, $\phi = 0.6$, 0.8, 1.0 and 1.2. Totally, 16 cases are conducted. The numerical simulations are performed on a staggered grid. The grid size of the gas phase is $\Delta x = 1.5\,\mu$m for the alkane flames and $\Delta x = 0.5\,\mu$m for the hydrogen flames. With these grid size, the flames are resolved at least by 20 points. On the other hand, the grid size of the wall is $\Delta x_s = 2\,\mu$m. To simulate the combustion condition in the SI engine, the unburnt gas temperature of fuel/air premixed gas and the ambient pressure are 400 K and 2 MPa, respectively. For the ignition, burnt gas temperature and composition are set from $x = 2.0$ mm to the right boundary. Initial flow velocity is 0 m/s for whole domain.

As a wall material, a heat insulation material with low thermal conductivity and low volumetric heat capacity is considered. The thermal properties of such material called SiRPA (Sillica Reinforced Porous Anodized Aluminum) [3] is referred for the properties of the heat insulation material. Additionally, for the purpose of the comparison, Al alloy, named Lo-Ex, used for the automobile engine cylinder [23] is also considered. The thermal properties of these materials are summarized in Table 2.1. In this study, temperature dependence of the thermal properties of the wall is neglected. Initial wall temperature is uniform at 400 K. The flame is ignited at right boundary and propagates toward the wall. At left boundary of the wall, temperature is fixed at 400 K same as the temperature of cooling water used in the practical SI engine, and at right boundary of the wall, wall surface temperature is calculated to fulfill the heat balance as mentioned above. For the gas phase calculation, at outlet boundary, pressure is fixed at ambient pressure and Neumann condition is applied for other properties, and at gas-wall interface, enthalpy and density are calculated by using the wall surface temperature, velocity is

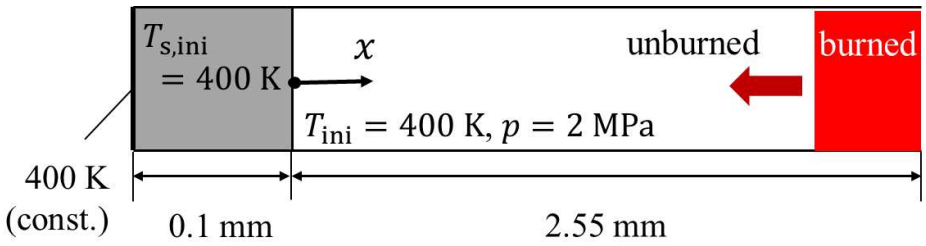

Figure 2.1: Schematic of computational domain.

Table 2.1: Volumetric heat capacity, $\rho_s c_s$, thermal conductivity, λ_s, and thermal diffusivity, α_s, of insulation material [3]
and Al alloy [23].

Material	Insulation material	Al alloy
$\rho_s c_s$ [J/(m^3·K)]	1.3×10^6	2.6×10^6
λ_s [W/(m·K)]	0.67	121.0
α_s [m^2/s]	5.2×10^{-7}	4.7×10^{-5}

fixed 0 m/s and Neumann condition is applied for other properties.

2.2.1.3 Numerical procedure

Numerical simulations are performed by using an in-house thermal flow analysis code called FK^3 [24]. This code is pressure-based semi-implicit solver for compressible flows and the fractional-step method based on characteristic splitting is employed [25]. The convective term in the conservation equation of momentum is evaluated using second order central difference scheme, while convective terms in conservation equations of scalars are solved using fifth order WENO (Weighted Essentially Non-Oscillatory) scheme [26]. For the discretization of the convective terms near the wall, low order one-sided difference scheme is used. For both of the reactive flow and heat conduction calculations, the

spatial derivatives of the diffusion terms are evaluated by second order central difference scheme. The time integration of the convective terms is conducted by third order explicit TVD (total variation diminishing) Runge-Kutta scheme [27]. The chemical reaction is integrated using VODE [28]. For all thermodynamic properties and transport properties of the gas phase, their temperature dependence are considered and thermodynamic properties are calculated by using NASA polynomials and transport properties are calculated according to CHEMKIN [29, 30]. On the other hand, the temperature dependence of the solid wall properties are not considered since the temperature rising in the wall is relatively small.

The CPU time for each case was up to 40,000 hours for alkane flame and 170 hours for H_2 flame by a parallel computing using 50 cores (actual time was 800 and 3.5 hours, respectively) on Cray XC40 supercomputer at Kyoto University.

2.2.2 Results and discussion

2.2.2.1 Effect of insulation wall on wall heat flux (CH_4 at $\phi = 1.0$)

Figure 2.2 shows the time variations of distributions of gas temperature T and temperature inside the wall T_s for CH_4 flame at $\phi = 1.0$ with the insulation wall. In this paper, time $\tau = 0\,\mathrm{ms}$ is defined at the instant when the wall heat flux q_{wall} reaches its maximum value. The flame propagates toward the wall, and after $\tau = 0\,\mathrm{ms}$, T in the vicinity of the wall decreases with time because of the heat loss. The obtained laminar burning velocity is 14.16 cm/s and agrees well with the experiment [31]. For T_s in the insulation wall, it starts to increase from $\tau = -0.5\,\mathrm{ms}$ and keeps increasing until $\tau = 3\,\mathrm{ms}$. In this time duration, T_s near the wall surface increases rapidly, and then high temperature gradually conducts inside the wall. This increase in T_s is more than that inside the Al alloy wall owing to lower thermal conductivity and lower volumetric heat capacity.

This difference is observed in terms of wall surface temperature T_{wall}, as shown in Fig. 2.3. T_{wall} increases about 55 K on the insulation wall, and thereafter it hardly changes with time. On the other hand, T_{wall} on the Al alloy wall increases less than 2 K

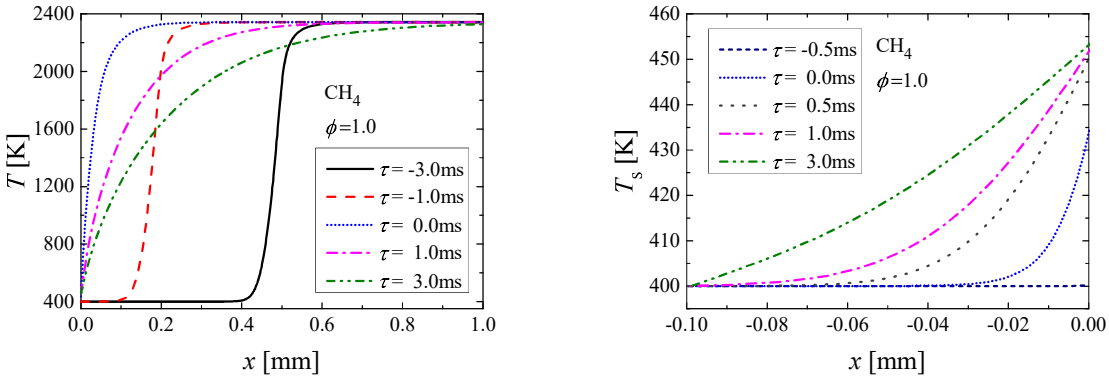

(a) (b)

Figure 2.2: Time variations of distributions of (a) gas temperature, T, and (b) temperature inside wall, T_s, for CH_4 flame at $\phi = 1.0$ with insulation wall.

and then decreases to 400 K.

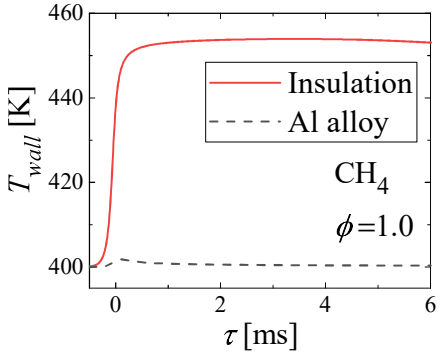

Figure 2.3: Comparisons of time variations of wall surface temperature, T_{wall}, between two wall materials for CH_4 flame at $\phi = 1.0$.

To see how this increase in T_{wall} on the insulation wall affects the behavior of wall heat flux q_{wall}, the time variations of q_{wall} are compared in Fig.2.4. Figure 2.4(a) shows the time variations of q_{wall} on the insulation and Al alloy walls. Although T_{wall} increases drastically on the inuslation wall, the behaviors of q_{wall} on both insultion and Al alloy walls look almost the same in this figure. Hence, to focus on the difference of q_{wall}

between two wall materials, Fig.2.4(b) shows the time variation of the reduction of q_{wall} due to the insulation defined as $q_{wall,Al} - q_{wall,ins}$. In this paper, subscripts ins and Al represent values obtained by the simulations using the insulation and Al alloy walls, respectively. During most of the time, $q_{wall,Al} - q_{wall,ins}$ is positive value, which means that q_{wall} is reduced due to the insulation, however, around $\tau = 0\,\mathrm{ms}$, $q_{wall,Al} - q_{wall,ins}$ is negative contrary to the expectation although $T_{wall,ins}$ increases.

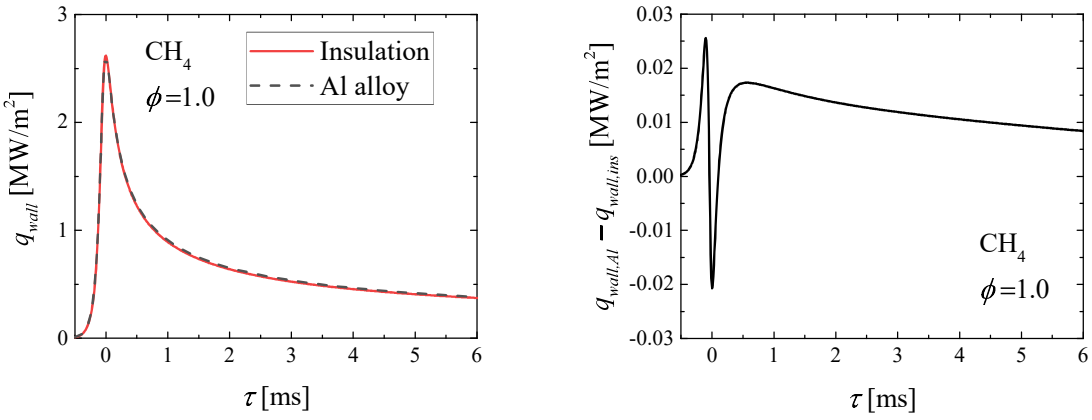

Figure 2.4: (a) Comparison of time variations of wall heat flux, q_{wall}, between two wall materials for CH_4 flame at $\phi = 1.0$ and (b) time variation of reduction of q_{wall} due to insulation wall, $q_{wall,Al} - q_{wall,ins}$.

To investigate how the insulation wall affects the q_{wall} in more detail, Fig.2.5 shows the time variations of the ratios of q_{wall}, gas thermal conductivity λ_{wall} and gas temperature gradient $(\partial T/\partial x)_{wall}$ on the insulation wall surface to those on the Al alloy wall surface. Hereafter, the ratio of property f_{wall} is represented by $r(f)$. It is noted that the magnitude of q_{wall} is calculated by products of λ_{wall} and $(\partial T/\partial x)_{wall}$. As shown in this figure, as $T_{wall,ins}$ increases with time, although $r(\partial T/\partial x)$ decreases, $r(\lambda)$ increases. This increase in $r(\lambda)$ weakens the reduction of q_{wall} due to the insulation. Around $\tau = 0\,\mathrm{ms}$, since $q_{wall,ins}$ is larger than $q_{wall,Al}$ as shown in Fig.2.4(b), $r(q)$ takes a peak value which slightly exceeds 1.

To clarify the mechanism of this unexpected behavior, the time variations of $r(\lambda)$ and $r(\partial T/\partial x)$ are discussed respectively. Regarding $r(\lambda)$, λ_{wall} is calculated from T_{wall} and gas composition on the wall. Because the time variations of gas composition on both the walls are almost the same, it is assumed that only the difference in T_{wall} between two wall materials affects the difference in λ_{wall} between two wall materials. Hence, $r(\lambda)$ steeply increases as $T_{wall,ins}$ also steeply increases before $\tau = 0\,\mathrm{ms}$. After $\tau = 0\,\mathrm{ms}$, the increases in both $T_{wall,ins}$ and $r(\lambda)$ becomes milder. On the other hand, in terms of $r(\partial T/\partial x)$, it starts to decrease before $\tau = 0\,\mathrm{ms}$, and it keeps decreasing after $r(\lambda)$ and $T_{wall,ins}$ hardly change. In addition, the decreasing speed of $r(\partial T/\partial x)$ is more gentle than increasing speed of $r(\lambda)$. To investigate this behavior of $r(\partial T/\partial x)$, Fig. 2.6 shows the time variations of $(\partial T/\partial x)_{wall,ins}$, $(\partial T/\partial x)_{wall,Al}$ and the reduction of $(\partial T/\partial x)_{wall}$ due to the insulation, namely $(\partial T/\partial x)_{wall,Al} - (\partial T/\partial x)_{wall,ins}$. Both $(\partial T/\partial x)_{wall,ins}$ and $(\partial T/\partial x)_{wall,Al}$ steeply increase before $\tau = 0\,\mathrm{ms}$, and then after decrease exponentially, regardless of the wall material. Awing to this sharp increase in $(\partial T/\partial x)_{wall}$ before $\tau = 0\,\mathrm{ms}$, the decrease in $r(\partial T/\partial x)$ is suppressed although $(\partial T/\partial x)_{wall,Al} - (\partial T/\partial x)_{wall,ins}$ increases. Thus, $r(q)$ increases before $\tau = 0\,\mathrm{ms}$. Furthermore, as shown in Fig. 2.6, $(\partial T/\partial x)_{wall,Al} - (\partial T/\partial x)_{wall,ins}$ also decreases after $\tau = 0\,\mathrm{ms}$. However, the decreasing rates of $(\partial T/\partial x)_{wall,Al} - (\partial T/\partial x)_{wall,ins}$is smaller than those of $(\partial T/\partial x)_{wall,Al}$ and $(\partial T/\partial x)_{wall,ins}$, especially until $\tau = 0.5\,\mathrm{ms}$. Hence, $r(\partial T/\partial x)$ keeps decreasing after $r(\lambda)$ and $T_{wall,ins}$ hardly change, and thus, $r(q)$ decreases after $\tau = 0\,\mathrm{ms}$. Consequently, $r(q)$ slightly exceeds 1 at $\tau = 0\,\mathrm{ms}$. Here it is noted that because q_{wall} reaches its maximum value at $\tau = 0\,\mathrm{ms}$, the behavior of $r(q)$ around this time instant strongly affects the total heat loss reduction.

2.2.2.2 Effects of equivalence ratio and fuel composition

To evaluate the heat loss reduction due to the insulation, heat loss reduction rate Λ is defined as

$$\Lambda = 1 - \frac{\int q_{wall,ins} d\tau}{\int q_{wall,Al} d\tau}. \tag{2.7}$$

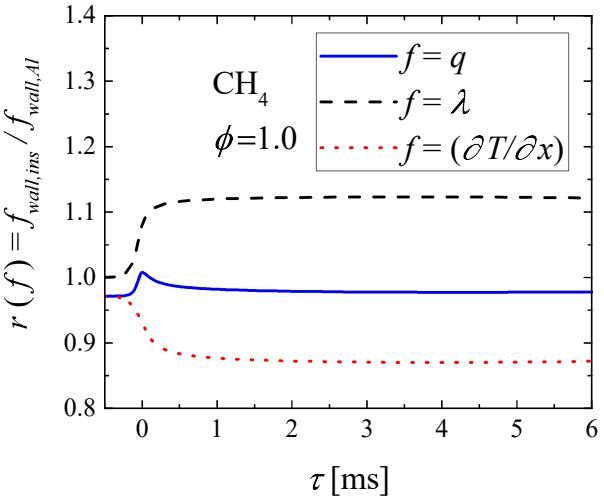

Figure 2.5: Time variations of ratios, $r(f)$, of some properties, f, at insulation wall surface to those at Al alloy wall surface for CH_4 flame at $\phi = 1.0$. (Solid line: f is heat flux, q, Broken line: f is gas thermal conductivity, λ, Dotted line: f is gas temperature gradient, $(\partial T/\partial x)$)

Figure 2.7 compares the time variations of Λ at different equivalence ratios for CH_4, C_2H_6, C_3H_8 and H_2 flames. As for the effect of the equivalence ratio, Λ becomes higher both with increase and decrease in the equivalence ratio from the stoichiometric ratio, regardless of the fuels. The value of Λ reaches up to 2.1% at $\tau = 6$ ms, and this order matches well with the existing experiment [32].

To investigate this reason, Fig.2.8 compares the time variations of $T_{wall,ins}$, $q_{wall,ins}$ and $q_{wall,Al} - q_{wall,ins}$ among at different equivalence ratios for CH_4 and H_2 flames. Furthermore, Fig. 2.9 shows those time variations for CH_4 flame at $\phi = 0.6$, because the flame propagates slower than those at the other equivalence ratios, and it is difficult to compare in the same graph. For CH_4 flames, at $\phi = 0.6$, 0.8 and 1.2, compared with at $\phi = 1.0$, $T_{wall,ins}$ increases slower and less owing to the lower maximum value of q_{wall}. As explained earlier, the time variation of the reduction of q_{wall} due to the insulation is related to the behaviors of λ_{wall} and $(\partial T/\partial x)_{wall}$.

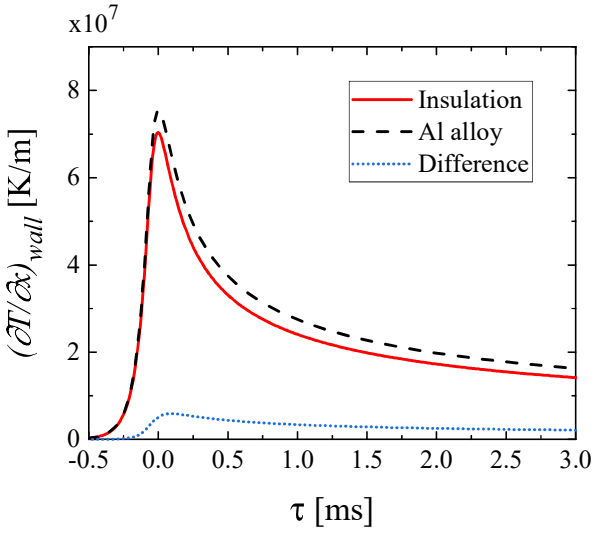

Figure 2.6: Comparison of time variations of gas temperature gradient at wall surface, $(\partial T/\partial x)_{wall}$, between two wall materials for CH_4 flame at $\phi = 1.0$ and reduction of $(\partial T/\partial x)_{wall}$ due to insulation wall, $(\partial T/\partial x)_{wall,Al} - (\partial T/\partial x)_{wall,ins}$.

Hence, Fig.2.10 compares the time variations of $r(\lambda)$ and $r(\partial T/\partial x)$ at different equivalence ratios for CH_4 flames around $\tau = 0$ ms. For $r(\lambda)$, at $\tau = 0$ ms, values at $\phi = 0.6$, 0.8, 1.2 are smaller than that at $\phi = 1.0$ due to the lower $T_{wall,ins}$. On the other hand, for $r(\partial T/\partial x)$, at $\phi = 0.6$, 0.8, 1.2, because of lower $T_{wall,ins}$, the reduction of $(\partial T/\partial x)_{wall}$ becomes smaller, however, at such condition the peak of $(\partial T/\partial x)_{wall}$ at $\tau = 0$ ms is also smaller. Hence $r(\partial T/\partial x)$ changes smaller compared to $r(\lambda)$ at $\tau = 0$ ms. This value is about 0.93 regardless of the equivalence ratio and fuel composition. As a results, at $\phi = 0.6$, 0.8 and 1.2, the decrease in the reduction of q_{wall} at $\tau = 0$ ms becomes smaller. This smaller reduction of q_{wall} makes Λ value immediately after $\tau = 0$ ms higher than that at $\phi = 1.0$. Furthermore, this magnitude relation does not change with time. This indicates that the decrease in the reduction of q_{wall} at $\tau = 0$ ms strongly affects the magnitude relation of Λ among different equivalence ratios after several milliseconds. Hence, Λ for CH_4 flame at $\tau = 6$ ms becomes higher both with increase and decrease in the equivalence ratio from the stoichiometric ratio. For C_2H_6 and C_3H_8 flames, the similar tendencies are observed.

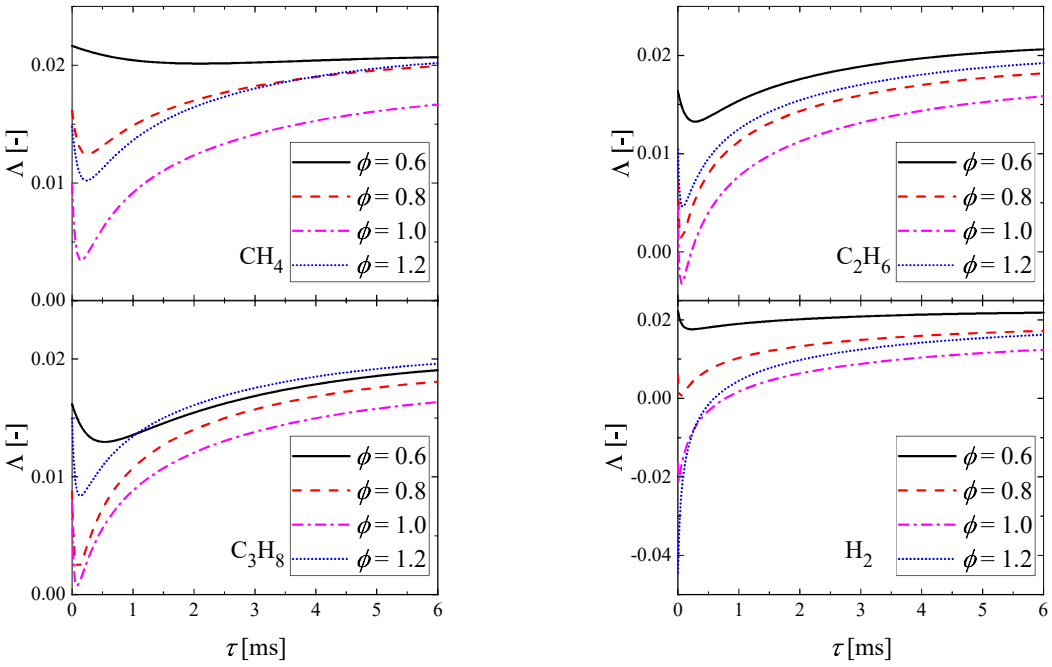

Figure 2.7: Comparisons of time variations of heat loss reduction rate, Λ, at different equivalence ratios of $\phi = 0.6$, 0.8, 1.0 and 1.2 for CH_4, C_2H_6, C_3H_8 and H_2 flames.

In contrast, the profiles of H_2 flames in Fig.2.8 show different tendency from CH_4 and other alkane flames. For H_2 flames, different from CH_4 flames, at $\phi = 1.2$, $T_{wall,ins}$ and $q_{wall,ins}$ increase faster and more than those at $\phi = 1.0$ because of the faster laminar burning velocity and steeper temperature gradient. Owing to this, as shown in Fig.2.7, Λ for H_2 flame at $\phi = 1.2$ is smaller than at $\phi = 1.0$ immediately after $\tau = 0$ ms. However, thereafter magnitude relation is reversed at $\tau = 0.3$ ms, and then at $\tau = 6$ ms Λ reaches 1.2 % and 1.6 % at $\phi = 1.0$ and 1.2, respectively. The reason of this reversal is considered due to the difference in the gas thermal diffusivity. Figure 2.11 compares the burnt gas thermal diffusivity α_b and burnt gas thermal conductivity λ_b among different fuels at each equivalence ratio. Comparing α_b and λ_b values at $\phi = 1.0$ and 1.2, only the H_2 flame shows a higher α_b value at $\phi = 1.2$ due to a higher λ_b. Because the thermal conductivity of H_2 is higher than those of alkanes, under a rich condition α_b and λ_b of the H_2 flames increase although those of alkane flames hardly change. For the tendencies

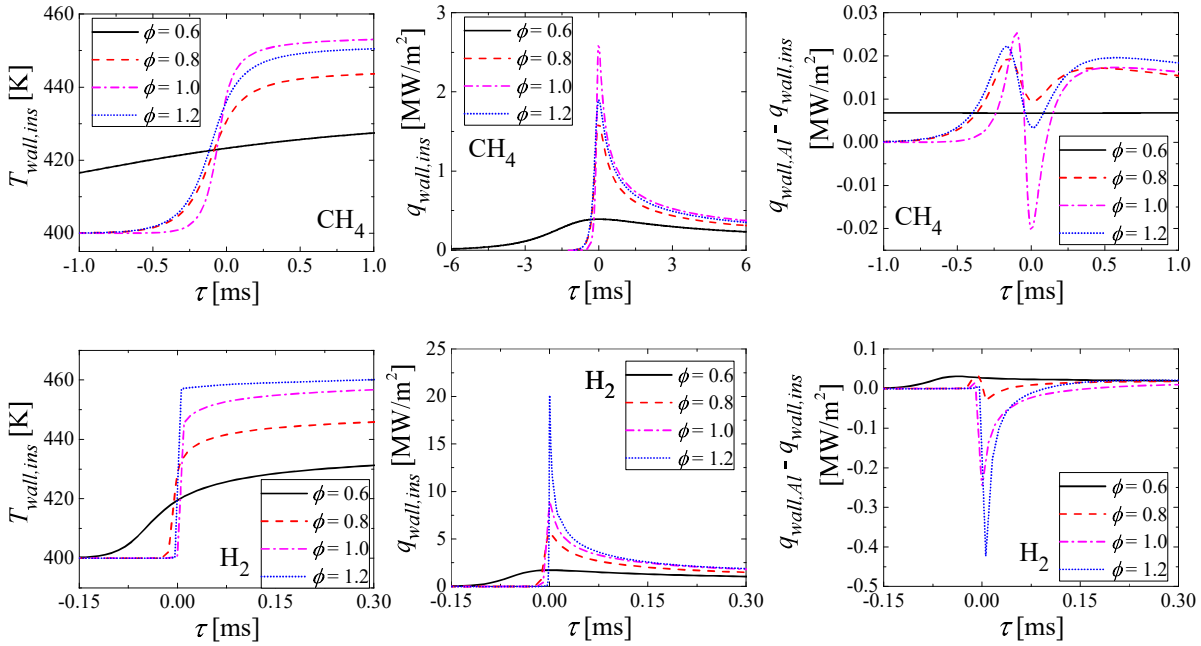

Figure 2.8: Comparisons of time variations of surface temperature, $T_{wall,ins}$, (left) and wall heat flux, $q_{wall,ins}$, (middle) on insulation wall and reduction of wall heat flux (right) at different equivalence ratios of $\phi = 0.6$, 0.8, 1.0 and 1.2 for CH_4 (top) and H_2 (bottom) flames.

of the changes in the gas density and gas heat capacity against equivalence ratio, they are similar, regardless of the fuel. Owing to this increase in α_b at $\phi = 1.2$, $(\partial T/\partial x)_{wall}$ decreases faster than at $\phi = 1.0$, and thus the reduction of q_{wall} and Λ immediately increase and become higher. Moreover, for CH_4 flames in Fig.2.7, Λ at $\phi = 0.8$ is larger than that at $\phi = 1.2$ immediately after $\tau = 0$ ms, but there exists a crossover point around $\tau = 4$ ms where Λ at $\phi = 1.2$ becomes slightly larger than that at $\phi = 0.8$. Such a crossover point also exists in the time variations of Λ for C_3H_8 flames in Fig.2.7 between $\phi = 0.6$ and 1.2 around $\tau = 1$ ms. These behaviors are similar to the time variation of Λ for H_2 flames between $\phi = 1.0$ and 1.2, and are also explained by the differences in α_b between two equivalence ratio conditions shown in Fig.2.11

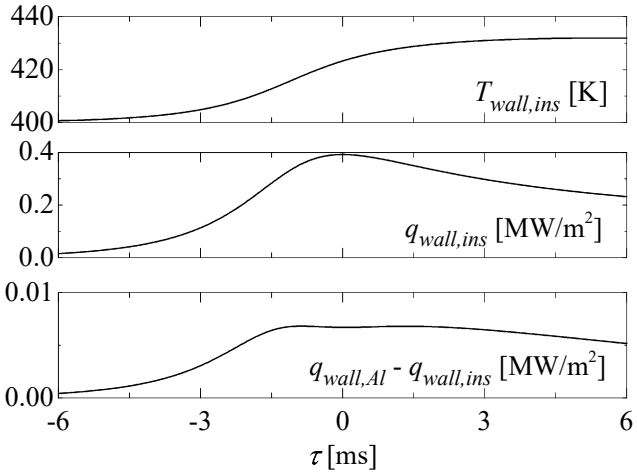

Figure 2.9: Time variations of surface temperature, $T_{wall,ins}$, (top) and wall heat flux, $q_{wall,ins}$, (middle) on insulation wall and reduction of wall heat flux (bottom) at $\phi = 0.6$ for CH_4 flame.

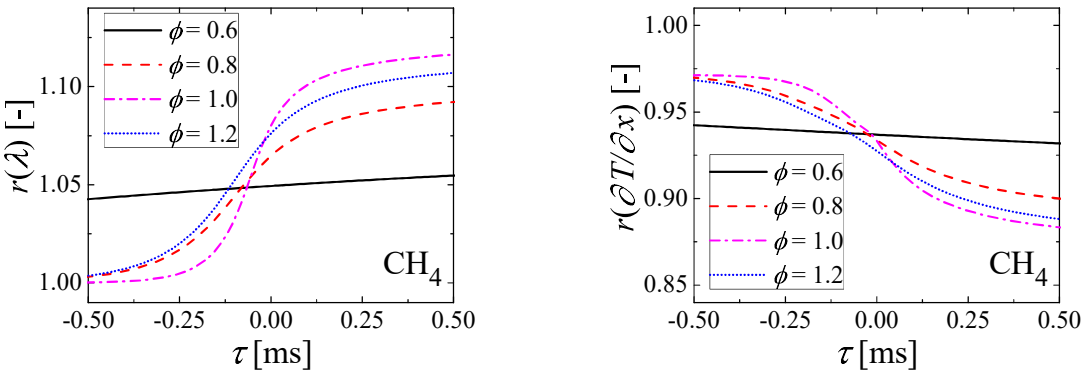

(a) (b)

Figure 2.10: Comparisons of time variations of ratios, r, of (a) gas thermal conductivity, λ, and (b) gas temperature gradient, $(\partial T/\partial x)$, on insulation wall surface to those on Al alloy wall surface at different equivalence ratios of $\phi = 0.6$, 0.8, 1.0 and 1.2 for CH_4 flames.

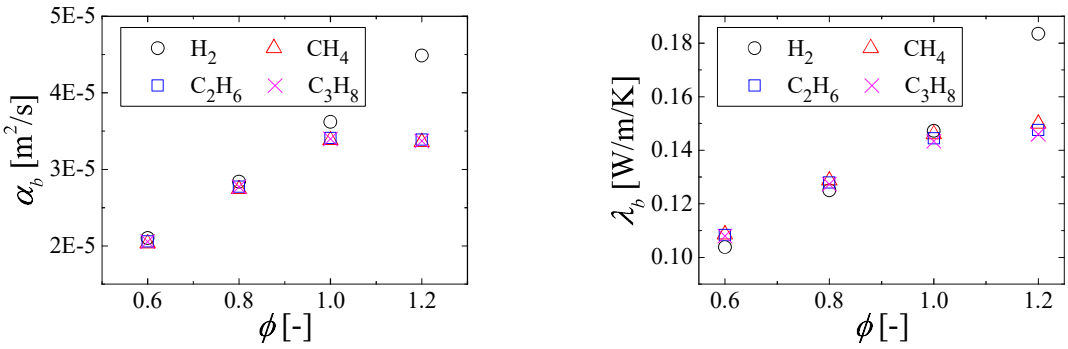

(a) (b)

Figure 2.11: Comparisons of (a) burnt gas thermal diffusivity, α_b, and (b) burnt gas thermal conductivity, λ_b, among different fuels at each equivalence ratio.

2.3 Effects of pressure and turbulence

2.3.1 Numerical simulation

2.3.1.1 Governing equations

In this study, to investigate the effect of wall material on the wall heat flux, numerical simulations of reactive flow and heat conduction in the wall are coupled with. For the reactive flow, the governing equations for conservation of mass, momentum, energy and mass fractions of chemical species are solved as follows

$$\frac{\partial \rho}{\partial t} + \nabla \cdot (\rho \boldsymbol{u}) = 0, \tag{2.8}$$

$$\frac{\partial \rho \boldsymbol{u}}{\partial t} + \nabla \cdot (\rho \boldsymbol{u}\boldsymbol{u}) = -\nabla p + \nabla \cdot \boldsymbol{\tau}, \tag{2.9}$$

$$\frac{\partial \rho h}{\partial t} + \nabla \cdot (\rho h \boldsymbol{u}) = \frac{\partial p}{\partial t} + \boldsymbol{u} \cdot \nabla p + \nabla \cdot (\rho \alpha \nabla h) + \boldsymbol{\tau} : \nabla \boldsymbol{u}, \tag{2.10}$$

$$\frac{\partial \rho Y_k}{\partial t} + \nabla \cdot (\rho Y_k \boldsymbol{u}) = \nabla \cdot (\rho D_k \nabla Y_k) + \rho \dot{\omega}_k. \tag{2.11}$$

along with the equation of state for ideal gas. In the Eq.2.11, D_k is calculated based on unity Lewis number assumption. To describe the combustion reaction of methane, a two-step global reaction model [33] is used for the purpose of saving the computational cost.

For the heat conduction in the wall, the heat equation is solved. Furthernore, for the coupling, the wall surface temperature is calculated to fulfill the heat balance on the interface between gas and wall.

2.3.1.2 Computational setup

One-dimensional numerical simulations

The schematics of the computational domain for 1D numerical simulations is presented in Fig. 2.12. The length of the gas part is 2.55 mm and the thickness of the wall is

0.1 mm. The wall thickness is same as the heat insulation thickness used in the previous experiment [3]. The numerical simulations are performed on a staggered Cartesian grid, and the grid sizes for the gas and wall are $\Delta x = 1.5\,\mu$m, and $\Delta x_s = 2\,\mu$m, respectively. In this study, minimum flame thickness is about $20\,\mu$m for the ambient pressure of 4 MPa, and is resolved by more than 10 grid points. Hence, the system is well resolved with this mesh size. For all cases, time step is 1 ns. Because with these mesh size and time step, the diffusion number and CFL number are always less than 0.5 and 1, respectively, the numerical simulations are stably conducted. The domain is filled with CH_4/air premixed gas at equivalence ratio one and unburnt gas temperature is 700 K. This temperature is almost same as the temperature before the ignition in the spark ignition (SI) engine. To investigate the effect of the pressure on the efficiency of the heat insulation, the numerical simulations are performed various pressurized conditions, 1.0, 2.0 and 4.0 MPa. Initial flow velocity is 0 m/s for whole domain.

As a wall material, two materials summarized in Table 2.1 are considered. Totally, six cases are performed, and the cases are summarized in Table 2.2. In this study, temperature dependence of the thermal properties of the wall is neglected. Initial wall temperature is uniform at 400 K. The flame is ignited at right boundary and propagates toward the wall. At left boundary of the wall, temperature is fixed at 400 K same as the temperature of cooling water used in the practical SI engine, and at right boundary of the wall, wall surface temperature is calculated to fulfill the heat balance as mentioned above. For the gas phase calculation, at outlet boundary, pressure is fixed at ambient pressure and Neumann condition is applied for other properties, and at gas-wall interface, enthalpy and density are calculated by using the wall surface temperature, velocity is fixed 0 m/s and Neumann condition is applied for other properties.

Two-dimensional numerical simulations

The schematics of the computational domain for 2D numerical simulations is presented in Fig. 2.13. The domain is a rectangular channel whose length is 30 mm and height is

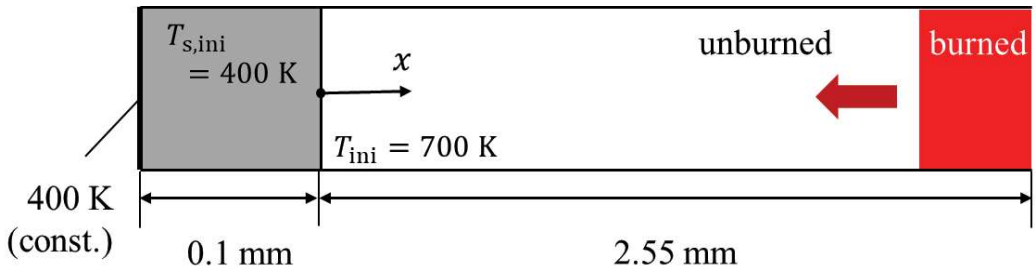

Figure 2.12: Schematic of computational domain for one-dimensional numerical simulations.

Table 2.2: Computational cases for one-dimensional numerical simulations.

Cases	Pressure [MPa]	Wall material
I-4MPa/Al-4MPa	4.0	Insulation/Al alloy
I-2MPa/Al-2MPa	2.0	Insulation/Al alloy
I-1MPa/Al-1MPa	1.0	Insulation/Al alloy

5.1 mm. The thickness of the walls are 0.1 mm. The long side direction is x-direction and spanwise direction is y-direction. The origin is set at the center of the domain. The simulations are performed on a staggered Cartesian grid consisting of 20000×3500 grid points (a total of 7 million grid points) in the x- and y- directions, respectively, and the grid sizes for the gas and wall are $\Delta x = \Delta y = 1.5\,\mu$m, and $\Delta x_s = 1.5\,\mu$m, $\Delta y_s = 2\,\mu$m, respectively. In 2D numerical simulations, laminar and turbulent CH_4/air premixed flames at 4 MPa are calculated. The unburnt gas temperature and equivalence ratio is 700 K and 1.0, respectively. Kolmogorov length scale for the turbulent cases is 3.4 μm and the flame thickness δ based on the maximum temperature gradient is 20 μm. To obtain δ, 1D freely propagating premixed flame is calculated by using Flame Master [34] with the detailed reaction mechanism of GRI-Mech 3.0 (52 species, 325 reactions) [35]. Hence the domain is well resolved by this grid size. The flame is ignited at the center of

the domain and then starts to propagate to the wall and goes out.

Three 2D numerical simulations are performed. One is the laminar case and the others are turbulent cases. For the laminar flame simulation, lower wall is the heat insulation wall and upper wall is the Al alloy wall and initial flow velocity is 0 m/s for whole domain. This case is called as Case L. For one case of the turbulent flame simulations, both of the upper and lower walls are insulation walls and for the other case both walls are Al alloy walls. These cases are called as Cases T-ins and T-Al, respectively. The cases are summarized in Table2.3. For turbulent cases, initially 2D artificial isotropic turbulence velocity fluctuations are superimposed with mean velocity of 0 m/s. Initial velocity field is obtained from the inverse Fourier transformation of an energy spectrum [36, 37] with the most energetic wave number used in the previous study [38]. The parameters for the premixed turbulent combustion are summarized in Table 2.4. To reproduce the turbulence in SI engine, initial turbulence is generated so that l and Ka, become 1 mm and about 3. In the regime diagram presented by Peters [39], the flame is classified in thin reaction zones. Initial vorticity field is presented in Fig. 2.14. Boundary conditions are same as the 1D numerical simulations.

Table 2.3: Computational cases for two-dimensional numerical simulations.

Cases	Velocity field	Upper wall material	Lower wall material
L	Laminar	Al alloy	Insulation
T-ins	Turbulent	Insulation	Insulation
T-Al	Turbulent	Al alloy	Al alloy

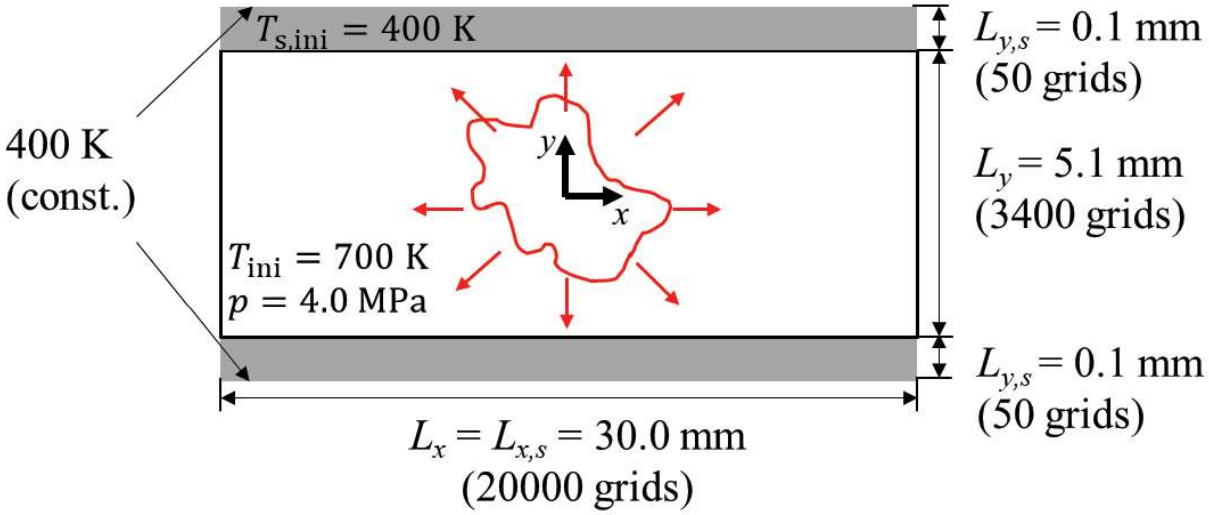

Figure 2.13: Schematic of computational domain for two-dimensional numerical simulations.

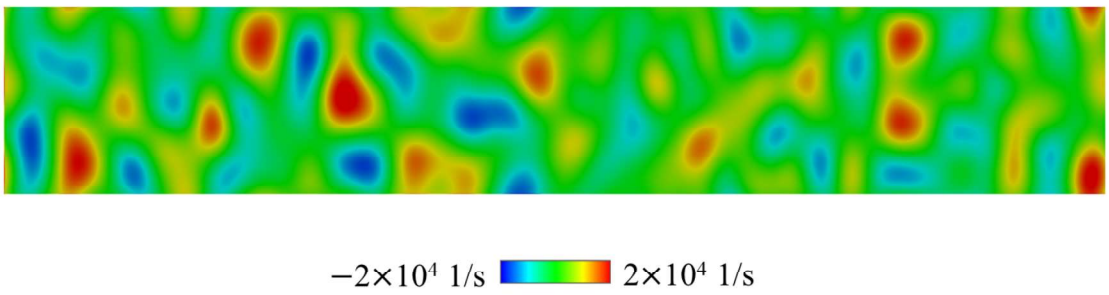

Figure 2.14: Initial vorticity distributions for two-dimensional numerical simulations.

Table 2.4: Parameters for premixed turbulent combustion.

Integral length scale, l [mm]	1.00
Velocity root mean square, u'_{rms} [m/s]	3.428
Flame thickness, δ [μm]	20.4
Laminar burning velocity, S_L [m/s]	0.430
l/δ [-]	49.0
u'_{rms}/S_L [-]	7.97
Karlovitz number, Ka [-]	3.21
Turbulent Reynolds number, Re_l [-]	390

2.3.1.3 Numerical procedure

1D and 2D numerical simulations are performed by using an in-house thermal flow analysis code called FK^3 [24]. This code is pressure-based semi-implicit solver for compressible flows and the fractional-step method based on characteristic splitting is employed [25]. The convective term in the conservation equation of momentum is discretized by second order central difference scheme, while convective terms in conservation equations of scalars are discretized by fifth order WENO scheme [26]. For the discretization of the convective terms near the wall, low order one-sided difference scheme is used. For both of the reactive flow and heat conduction calculations, the spatial derivatives of the diffusion terms are evaluated by second order central difference scheme. The time integration of the convective terms is conducted by third order explicit TVD Runge-Kutta scheme [27]. For all thermodynamic properties and transport properties of the gas phase, their temperature dependence are considered and thermodynamic properties are calculated by using NASA polynomials [45] and transport properties are calculated by using the same method used in CHEMKIN [29, 30]. The temperature dependence of the solid wall properties are not considered since the temperature rising in the wall is

relatively small.

The CPU times required for the Cases L, T-ins and T-Al are approximately 1,760,000, 880,000, and 880,000 core hours, respectively, using K-computer (Fujitsu SPARC64YM VIIIfx processor) The actual time required for parallel computation of 400,000, 200,000 and 200,000 steps using 8,000, 8,000, and 8,000 cores are approximately 220, 110, and 110 hours of real time, respectively.

2.3.2 Results and discussion

2.3.2.1 One-dimensional numerical simulations

Validation

To validate the simulations, in Table 2.5, the obtained laminar burning velocity with two-step reaction model [33] is compared with that obtained by using Flame Master [34] with GRI-Mech 3.0 [35]. At all pressure conditions, laminar burning velocity obtained by present simulation matches well with the result of GRI-Mech 3.0. In addition, to verify the grid size independence, Richardson extrapolation on the maximum wall heat flux on the insulation wall is conducted, and then the error is estimated. This verification is performed only at $p = 4\,\mathrm{MPa}$, because the temperature gradient is largest at this pressure. The mesh sizes $\Delta x = 1.0$, 1.5, 2.0 and 3.0 μm are tested. Figure 2.15 show the extrapolated value and evaluated error for each Δx. In Fig. 2.15(b), the error for $\Delta x = 1.5\,\mu\mathrm{m}$ is less than 1%, which implies that the domain is well resolved.

Table 2.5: Comparison of laminar burning velocity obtained with two-step reaction model [33] and with GRI-Mech 3.0 [35] at $p = 1$, 2 and 4 MPa.

	1 MPa	2 MPa	4 MPa
Two-step reaction	73.23 cm/s	54.68 cm/s	42.53 cm/s
GRI-Mech3.0	73.95 cm/s	55.19 cm/s	42.99 cm/s

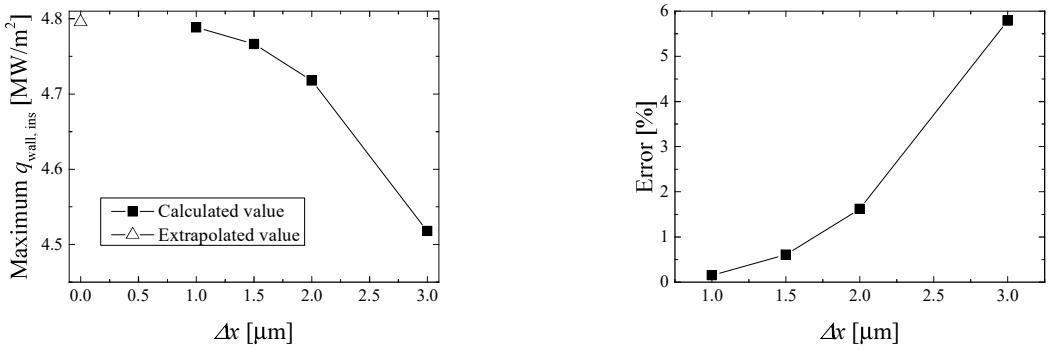

(a) Extrapolation (b) Error

Figure 2.15: (a) Extrapolation on maximum wall heat flux on insulation wall, $q_{\mathrm{wall,ins}}$, at $p = 4\,\mathrm{MPa}$ and (b) evalueted error at mesh size Δx =1.0, 1.5, 2.0 and 3.0 μm.

Effect of wall material

Figure 2.16 shows the time variations of wall surface temperature, T_{wall}, on the insulation wall (Case I-4MPa) and Al alloy wall (Case Al-4MPa) at $p = 4\,\mathrm{MPa}$. For Cases I-4MPa and Al-4MPa, the flame reaches the wall at $t = 5.1\,\mathrm{ms}$. In this study, the time when the flame reaches the wall is defined as the time when the wall heat flux reaches its peak value. At this moment, T_{wall} on the insulation wall increases rapidly by approximately 70 K owing to its low volumetric heat capacity and thermal conductivity. This increse in T_{wall} was observed in the revious studies [2, 3]. After $t = 6\,\mathrm{ms}$, T_{wall} on the insulation wall is almost constant at 482 K. In contrast, on the Al alloy wall, T_{wall} increases about 2 K, and soon after, it decreases to 400 K. Figure 2.16 also shows that before $t = 5\,\mathrm{ms}$, T_{wall} on the insulation wall is higher than that on the Al alloy wall although the flame does not reach the wall. This is because initially the temperature and heat flux are discontinuous on the wall, and heat balance on the wall is not fulfilled for both cases.

To investigate how the wall heat flux, q_{wall}, changes with respect to the difference of the T_{wall}, Fig. 2.17 compares the time variations between q_{wall} on the insulation wall (Case I-4MPa) and Al alloy wall (Case Al-4MPa) at $p = 4\,\mathrm{MPa}$. At the moment the

flame reaches the wall, q_{wall} on the insulation wall increases more than that on the Al alloy wall contrary to the expectation, although T_{wall} on the insulation wall is higher. After that moment, the difference between the two values rapidly decreases and the magnitude relation is reversed as expected.

As q_{wall} is the product of gas thermal conductivity, λ_{wall}, and gas temperature gradient, $\left(\frac{\partial T}{\partial x}\right)_{\mathrm{wall}}$, on the wall, in Fig. 2.18, the time variations of λ_{wall} and $\left(\frac{\partial T}{\partial x}\right)_{\mathrm{wall}}$ on the insulation wall (Case I-4MPa) and Al alloy wall (Case Al-4MPa) at $p = 4\,\mathrm{MPa}$ are compared. λ_{wall} on the insulation wall is higher than that on the Al alloy wall at any moment owing to the higher wall surface temperature. This figure also shows that the tendency of change in λ_{wall} when the flame reaches the wall differs between the two cases. On the Al alloy wall, T_{wall} does not change so much with time and gas composition changes; therefore, λ_{wall} decreases. In contrast, on the insulation wall, although the gas composition changes, the effect of the increase of T_{wall} is stronger, and hence λ_{wall} increases. After the flame reaches the wall, the ratio of the λ_{wall} on the insulation wall and Al alloy wall is almost constant. Contrary to the λ_{wall}, $\left(\frac{\partial T}{\partial x}\right)_{\mathrm{wall}}$ on the insulation wall is smaller than that on the Al alloy wall almost all the time. To investigate how the differences in both λ_{wall} and $\left(\frac{\partial T}{\partial x}\right)_{\mathrm{wall}}$ affect q_{wall} reduction by the insulation, Fig. 2.19 shows the time variations of the ratios of q_{wall}, λ_{wall}, and $\left(\frac{\partial T}{\partial x}\right)_{\mathrm{wall}}$ on the insulation wall (Case I-4MPa) to those on the Al alloy wall (Case Al-4MPa) at $p = 4\,\mathrm{MPa}$. From $t = 4.9$ to $5.05\,\mathrm{ms}$, the increases of ratio in the $\left(\frac{\partial T}{\partial x}\right)_{\mathrm{wall}}$ affects the increase in the ratio of q_{wall}. Since before the flame reaches the wall, gas temperature near the insulation wall is higher than that near the Al alloy wall owing to the higher wall temperature, and the flame can propagate closer to the wall. Additionally, in this time duration, wall temperature on the insulation wall does not increase so much; thus, the ratios of $\left(\frac{\partial T}{\partial x}\right)_{\mathrm{wall}}$ and q_{wall} increases and exceeds 1. After $t = 5.05\,\mathrm{ms}$, wall temperature on the insulation wall rapidly increases, and thus the ratio of $\left(\frac{\partial T}{\partial x}\right)_{\mathrm{wall}}$ decreases. Consequently, the ratio of q_{wall} decreases although the ratio of λ_{wall} increases.

Furthermore, Fig. 2.21 shows the time variations of distributions of temperature, T_s, inside the insulation wall (Case I-4MPa) and Al alloy wall (Case Al-4MPa) at $p = 4\,\mathrm{MPa}$.

For both walls, T_s starts to increase around $t = 5.0\,\mathrm{ms}$. In the insulation wall, T_s near the wall surface rapidly increases, and then high temperature conducts inside the wall gradually. After $t = 6\,\mathrm{ms}$, wall surface temperature is almost constant, as shown in Fig. 2.16. In contrast, in the Al alloy wall, T_s increases until $t = 5.2\,\mathrm{ms}$, maintaining an almost linear distribution owing to high thermal diffusivity of Al alloy, and then decreases. Hence, after $t = 5.2\,\mathrm{ms}$, the ratios of $\left(\frac{\partial T}{\partial x}\right)_{\mathrm{wall}}$ and q_{wall} gradually decrease, even though this is difficult to observe in Fig. 2.19, and then at $t = 10\,\mathrm{ms}$, the ratio of q_{wall} reaches 0.975.

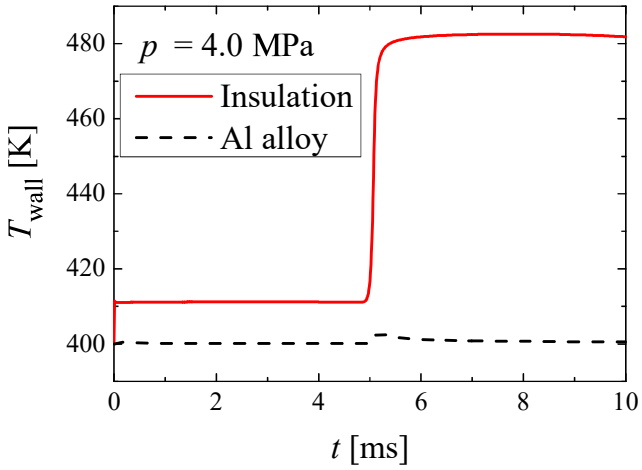

Figure 2.16: Time variations of wall temperature, T_{wall}, on insulation wall (Case I-4MPa) and Al alloy wall (Case Al-4MPa) at $p = 4\,\mathrm{MPa}$.

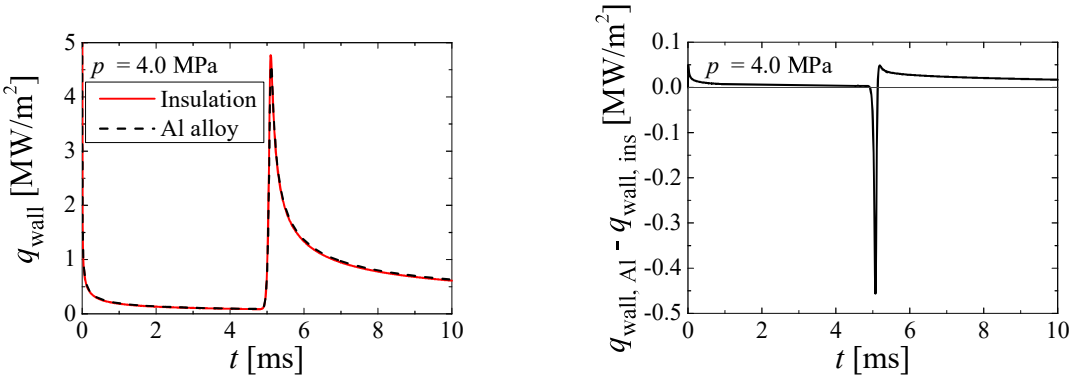

(a) q_{wall} (b) $q_{\mathrm{wall,Al}}$-$q_{\mathrm{wall,ins}}$

Figure 2.17: Time variations of (a) wall heat fluxes, q_{wall}, on insulation wall (Case I-4MPa) and Al alloy wall (Case Al-4MPa) at $p = 4\,\mathrm{MPa}$ and (b) their difference.

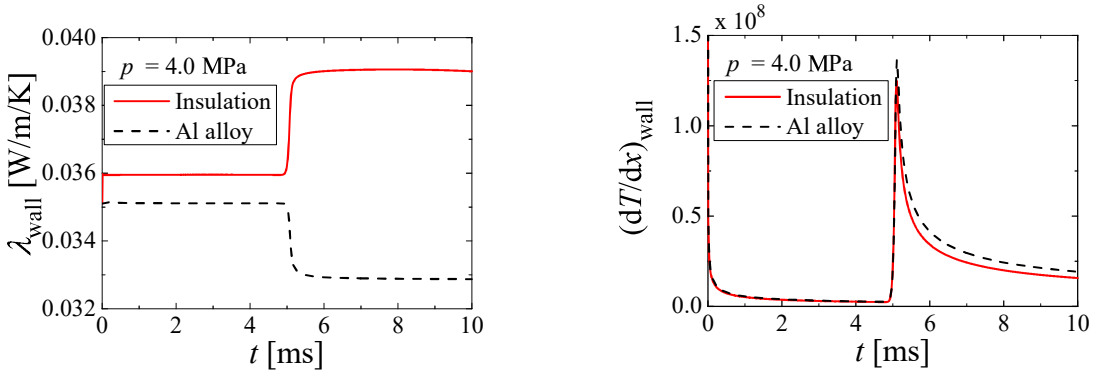

(a) λ_{wall} (b) $\left(\frac{\partial T}{\partial x}\right)_{\mathrm{wall}}$

Figure 2.18: Time variations of (a) gas thermal conductivity, λ_{wall}, and (b) gas temperature gradient, $\left(\frac{\partial T}{\partial x}\right)_{\mathrm{wall}}$, on insulation wall (Case I-4MPa) and Al alloy wall (Case Al-4MPa) at $p = 4\,\mathrm{MPa}$.

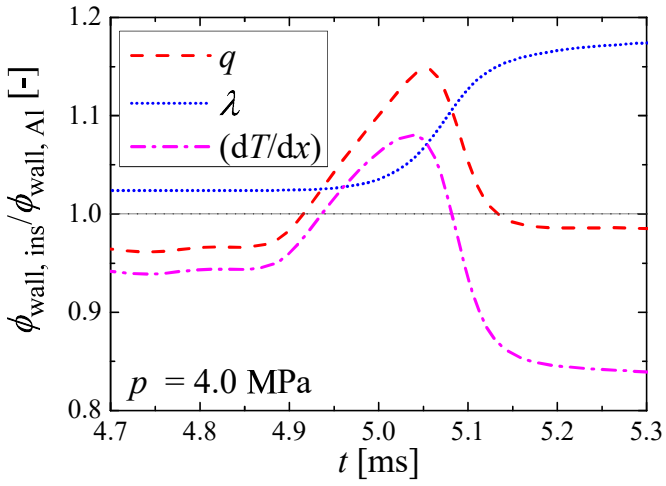

Figure 2.19: Time variations of ratios of wall heat flux, q_{wall}, gas thermal conductivity, λ_{wall}, and gas temperature gradient, $\left(\frac{\partial T}{\partial x}\right)_{\mathrm{wall}}$, on insulation wall (Case I-4MPa) to those on Al alloy wall (Case Al-4MPa) at $p = 4\,\mathrm{MPa}$.

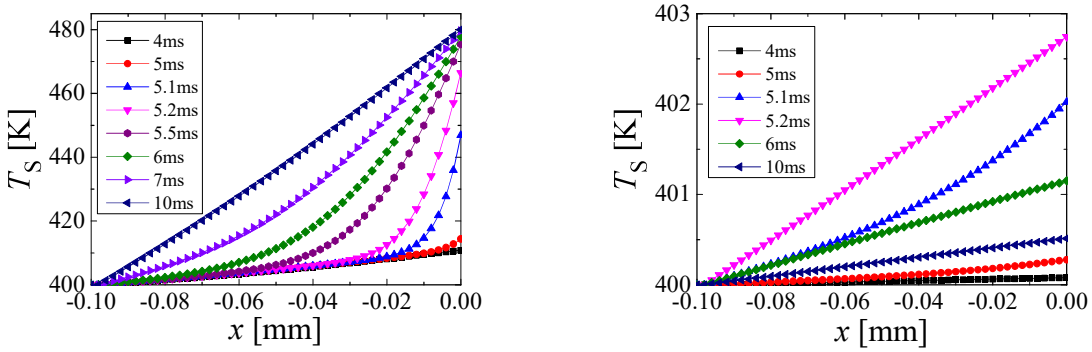

(a) Insulation wall

(b) Al alloy wall

Figure 2.20: Time variations of distributions of temperature, T_s, inside (a) insulation wall (Case I-4MPa) and (b) Al alloy wall (Case Al-4MPa) at $p = 4\,\mathrm{MPa}$.

Effect of ambient pressure

Figure 2.21 shows the comparisons of time variations of T_{wall} and q_{wall} on the insulation wall among Cases I-4MPa, I-2MPa, and I-1MP. It is obvious that both T_{wall} and q_{wall} is higher under higher pressure condition. As the gas density is higher under higher pressure condition, the gas thermal diffusivity decreases. This decreased thermal diffusivity makes the temperature distribution steeper, and thus T_{wall} and q_{wall} increase. In addition, under higher pressure condition, owing to the slower laminar burning velocity, the flame reaches the wall later. To compare the efficiency of the insulation among such different conditions, insulation rate, Λ, which indicates the reduction rate of the heat loss by the insulation, is defined as follows;

$$\Lambda = 1 - \frac{\int_{t1}^{t1+\Delta t} q_{wall,ins} dt}{\int_{t1}^{t1+\Delta t} q_{wall,Al} dt}, \tag{2.12}$$

where, $t1$ is defined as 1 ms before the moment the flame reaches the wall; it does not include the effect of initial temperature discontinuous on the wall. Moreover, as shown in Fig. 2.17 (b), the magnitude relation between $q_{\mathrm{wall,ins}}$ and $q_{\mathrm{wall,Al}}$ changes over time. Hence, Fig. 2.22 shows the comparison of the insulation rate, Λ, versus integration time, Δt, among different pressure conditions of $p = 4, 2,$ and 1MPa. The insulation rates increases with integration time and saturates. For the four strokes engine with rotational speed of 2000 and 3000 rpm, the expansion stroke corresponds to 15 and 10 ms, respectively. The insulation rate at $\Delta t = 15$ ms is higher at higher pressure and reaches approximately 1.8 % at $p = 4$ MPa. This value is of the same order of magnitude as the experiment by Wakisaka et al. [3] in which cycle-averaged heat flux on the insulation wall was compared with that on the wall without heat insulation coating using a single cylinder direct-injection diesel engine. In the experiment, cycle-averaged wall heat flux was reduced by 8 %. The higher value is considered due to the impingement flame formed in the experiment, which tends to enhance the wall heat flux.

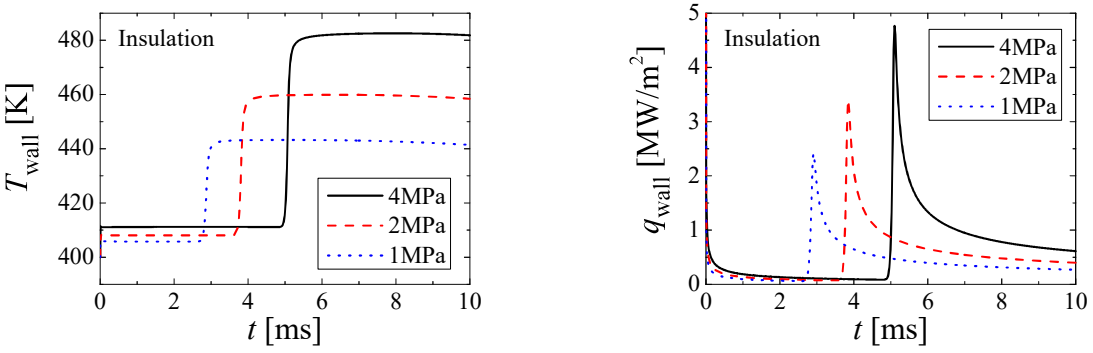

(a) T_{wall} (b) q_{wall}

Figure 2.21: Comparisons of time variations of (a) wall temperature, T_{wall}, and (b) wall heat flux, q_{wall}, on insulation wall among $p = 4, 2,$ and 1MPa (Cases I-4MPa, I-2MPa, and I-1MPa).

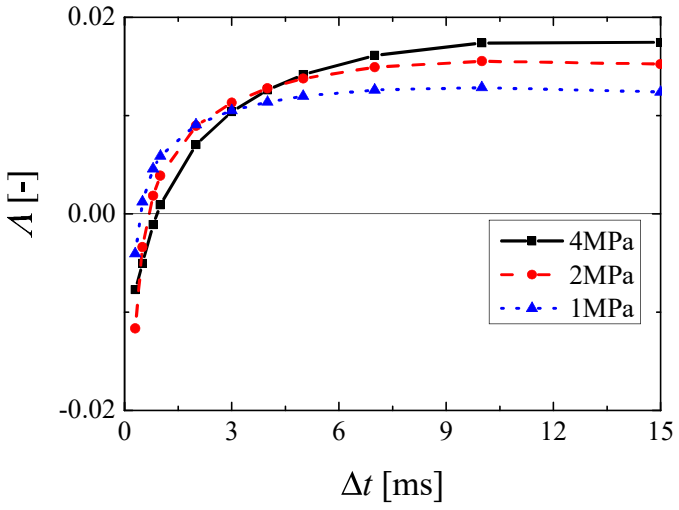

Figure 2.22: Effect of pressure on time variarion of insulation rate, Λ. ($p = 4, 2,$ and 1MPa)

2.3.2.2 Two-dimensional numerical simulations: Effect of turbulence

Figure 2.23 shows the time series of gas temperature distributions of Cases T-ins and L. In Case T-ins, the flame propagates with distortion due to turbulence and propagates faster than that in Case L owing to the larger flame surface area. Owing to faster flame propagation, the flame reaches the wall faster. After flames reach the walls, the flames propagate along the wall in the horizontal direction. Here (not shown in Fig. 2.23), the temperature distribution of Case T-Al is almost same as that of Case T-ins.

To investigate the effect of turbulence on the wall heat flux, Fig. 2.24 shows the time variations of q_{wall} at $x = 0.0\,\mathrm{mm}$ on the insulation wall and Al alloy wall in Case L and their difference. Similarly, for turbulent case, Fig. 2.25 shows the time variations at $x = -0.75\,\mathrm{mm}$ on the lower walls in Cases T-ins and T-Al. The selected points are where the flames first touch the walls. Regardless of the turbulent or laminar case, the tendency of the wall heat flux immediately before and after the moment when the flame reaches the wall is similar to the 1D numerical simulations, as shown in Fig. 2.17, although the magnitude is different from that in the1D cases, especially for the turbulent case.

Regarding the spatial distribution of the wall heat flux after the flames reach the walls, Figs. 2.26 and 2.27 show the time variations of spatial distributions of q_{wall} on the insulation walls of Cases L and T-ins, respectively. The peak value of q_{wall} on the insulation wall of Case L hardly changes with time, whereas, for Case T-ins, it fluctuates approximately 20 %. To investigate the effect of flow field on the wall heat flux, Figs. 2.28 to 2.30 show the instantaneous distributions of gas temperature and velocity vectors near the wall and q_{wall} on the lower walls for Case L at $t = 2.6\,\mathrm{ms}$, Case T-ins at the moment the peak value of q_{wall} is maximum ($t = 0.8\,\mathrm{ms}$), and Case T-ins at the moment the peak value of q_{wall} is minimum ($t = 1.0\,\mathrm{ms}$), respectively. For Case L, the velocity direction is away from the wall, and its magnitude is lower than that in turbulent cases. Hence, the peak value is almost the same as that of the 1D numerical simulation (Case I-4MPa). In contrast, in Case T-ins, when the peak value is maximum or minimum, there exist turbulent eddies with a strong flow toward or away from the wall, respectively.

In addition to the magnitude of q_{wall}, turbulence affects the propagation speed of the heat near the wall. As shown in Figs. 2.26 and 2.27, the flame propagation speed along the wall for Case T-ins is slower than that for Case L, which is contrary to the flame propagation in the center region. This is because the turbulent eddies in front of the flame surface suppress the advection of the flame front with high temperature toward the unburnt side, as shown in Fig. 2.31.

To investigate the effect of turbulence on the dependence on the wall materials, Fig. 2.32 compares instantaneous distributions of q_{wall} on the insulation wall and Al alloy wall for laminar and turbulent flames, and Fig. 2.33 shows their enlarged views. For all cases, the peak value of q_{wall} on the insulation wall is higher, the same as that of the 1D numerical simulations. Moreover, for turbulent case, the flame front near the insulation wall locates slightly outwards compared to near the Al alloy wall. This is because on the insulation wall, a higher gas thermal diffusivity, α_{wall}, as shown in Fig. 2.34, results in higher heat conduction toward the unburnt side. For the laminar case, although α_{wall} on the insulation wall is also higher than that on the Al alloy wall, the gap of the flame front is not observed, as shown in Fig. 2.33 (a). As explained earlier, in the turbulent case, the advection of the flame front is suppressed by the eddies, implying that the contribution of the heat conduction to the transportation of the high temperature is larger than that in the laminar case. Hence, the gap of the flame front in the vicinity of the wall is obsereved only for the turbulent case.

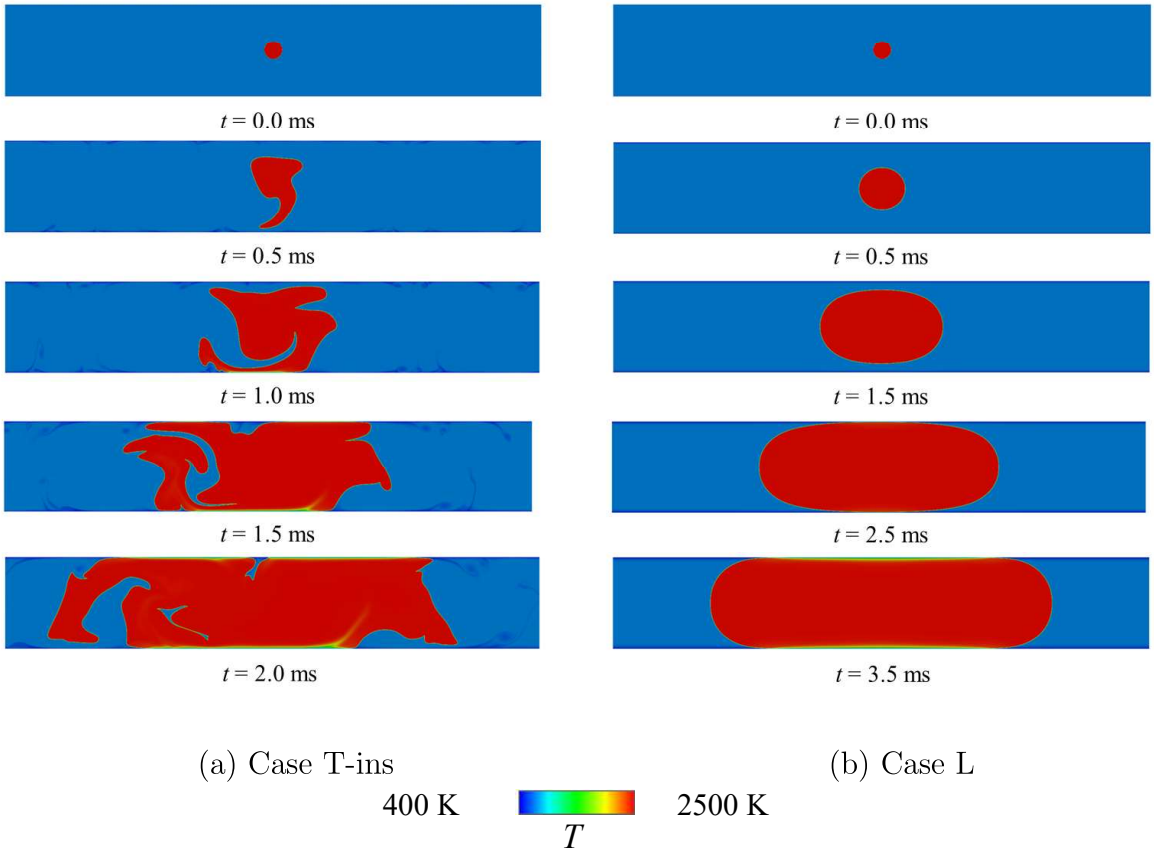

Figure 2.23: Time series of temperature distributions of (a) Cass T-ins and (b) Case L.

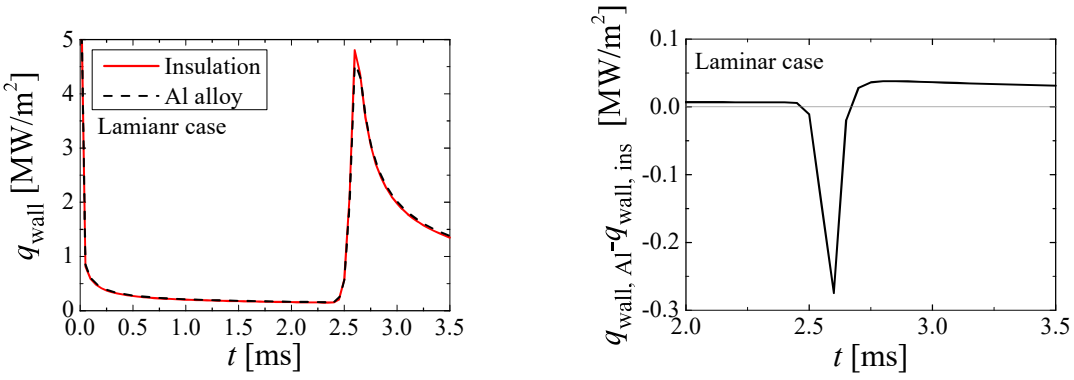

(a) q_{wall} (b) $q_{\mathrm{wall,Al}}$-$q_{\mathrm{wall,ins}}$

Figure 2.24: Time variations of (a) wall heat fluxes, q_{wall}, at $x = 0.0\,\mathrm{mm}$ on insulation (lower) wall and Al alloy (upper) wall of Case L and (b) their difference.

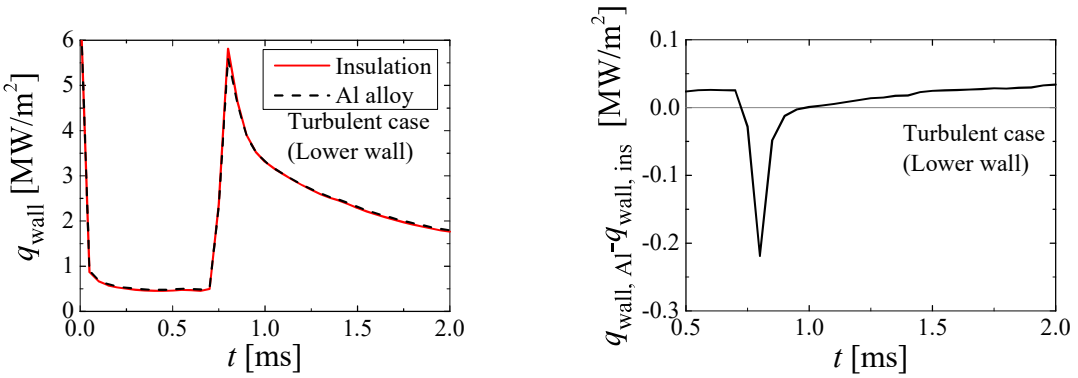

(a) q_{wall} (b) $q_{\mathrm{wall,Al}}$-$q_{\mathrm{wall,ins}}$

Figure 2.25: Time variations of (a) wall heat fluxes, q_{wall}, at $x = -0.75\,\mathrm{mm}$ on lower walls of Cases T-ins and T-Al and (b) their difference.

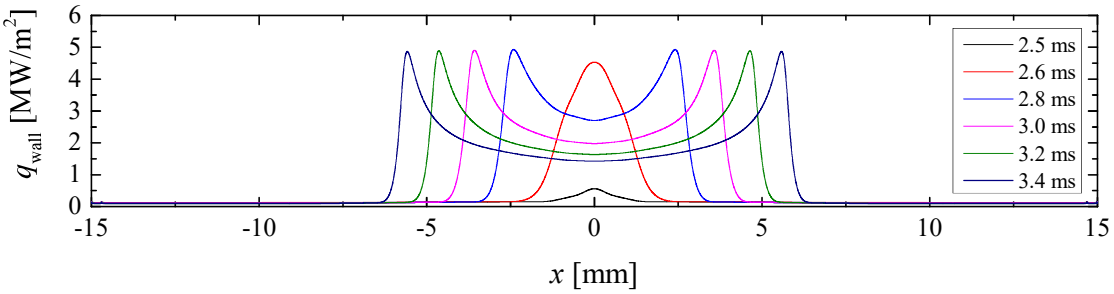

Figure 2.26: Time variations of spatial distribution of wall heat flux, q_{wall}, on insulation (lower) wall of Case L.

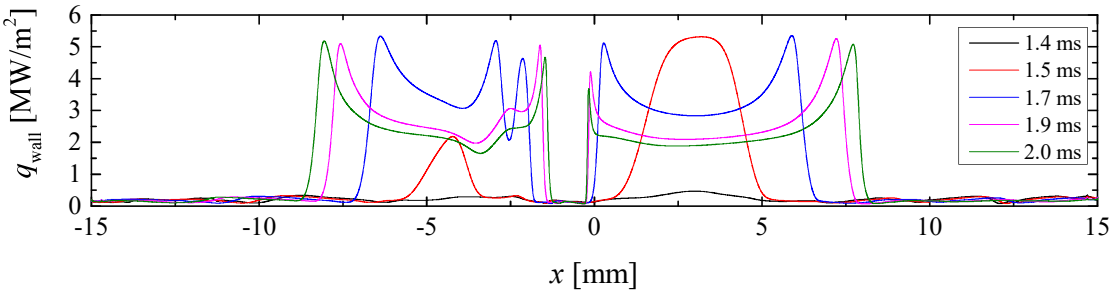

(a) Upper wall

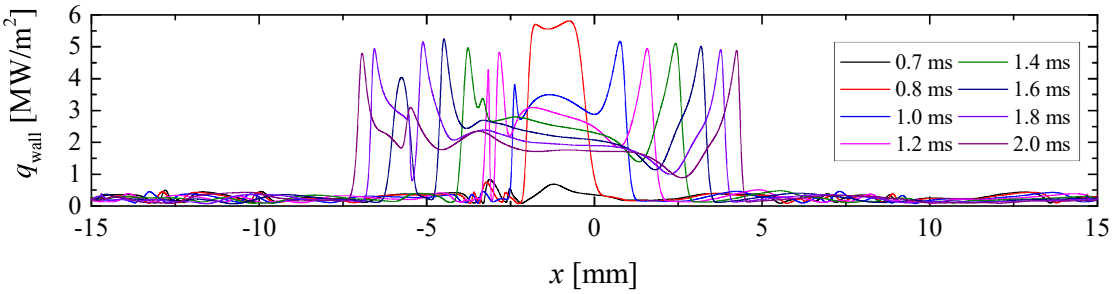

(b) Lower wall

Figure 2.27: Time variations of spatial distributions of wall heat flux, q_{wall}, on (a) upper wall and (b) lower wall of Case T-ins.

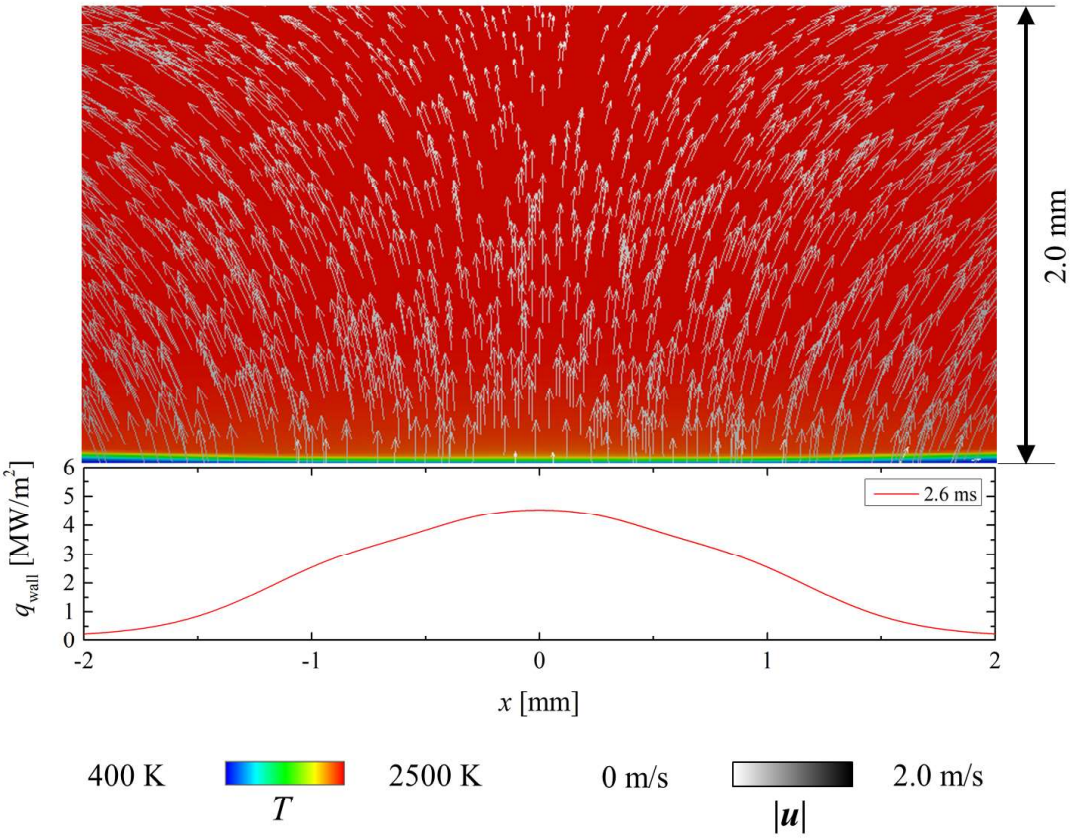

Figure 2.28: Instantaneous distributions of gas temperature, T, and velocity vecotors (represented by arrows) near wall, and wall heat flux q_{wall}, on insulation (lower) wall of Case L at $t = 2.6\,\mathrm{ms}$.

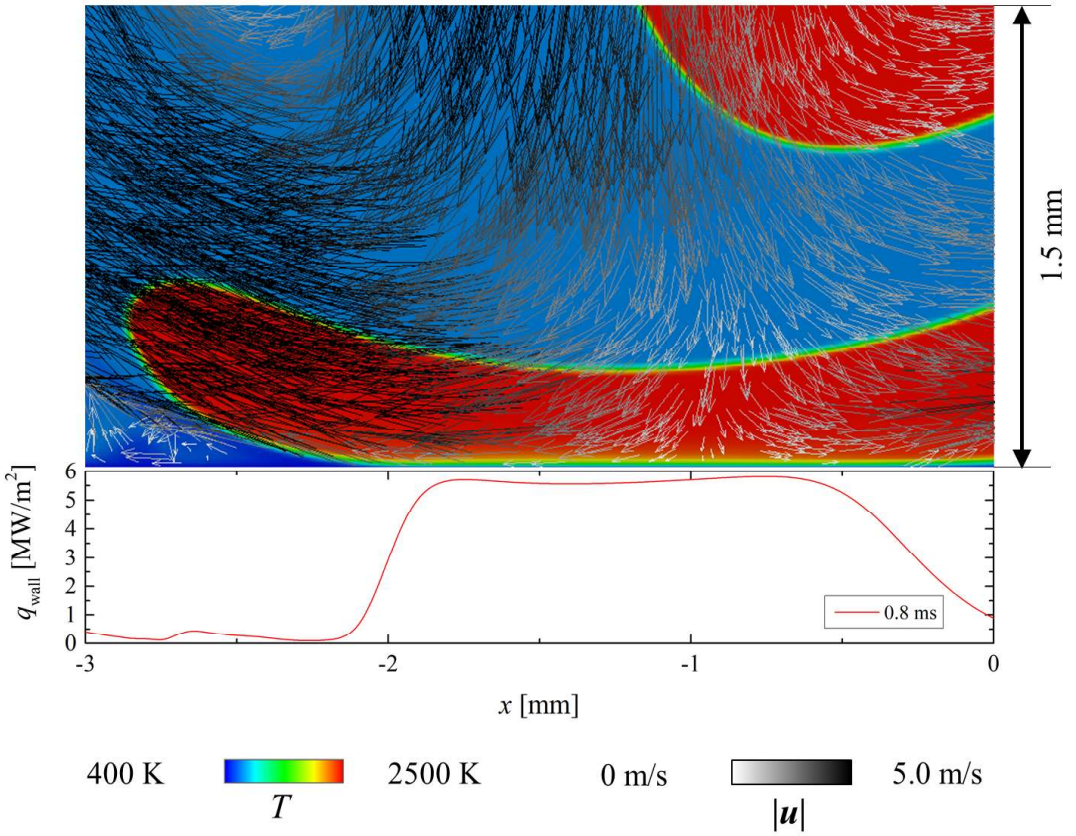

Figure 2.29: Instantaneous distributions of gas temperature, T, and velocity vecotors (represented by arrows) near wall, and wall heat flux, q_{wall}, on lower wall of Case T-ins at $t = 0.8\,\mathrm{ms}$.

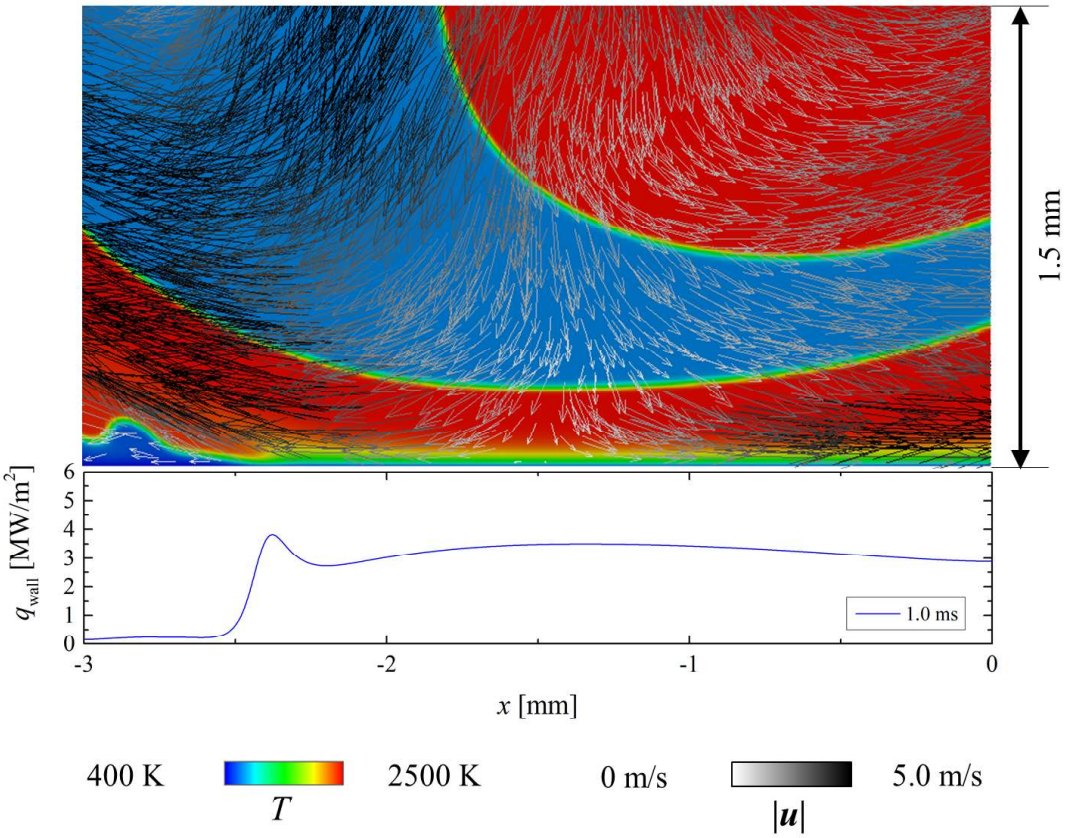

Figure 2.30: Instantaneous distributions of gas temperature, T, and velocity vecotors (represented by arrows) near wall, and wall heat flux, q_{wall}, on lower wall of Case T-ins at $t = 1.0\,\mathrm{ms}$.

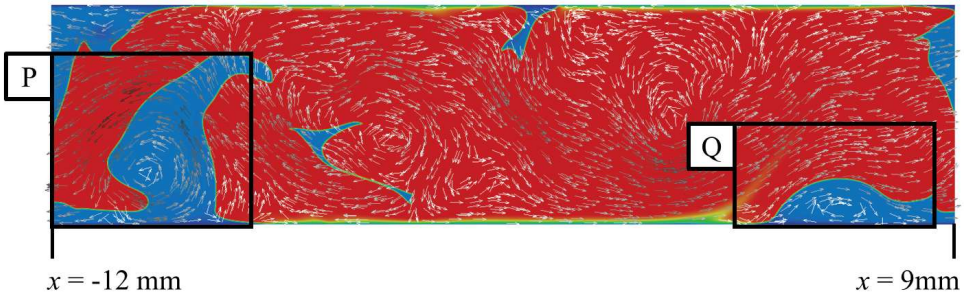

(a) Case T-ins at $t = 2.0\,\mathrm{ms}$

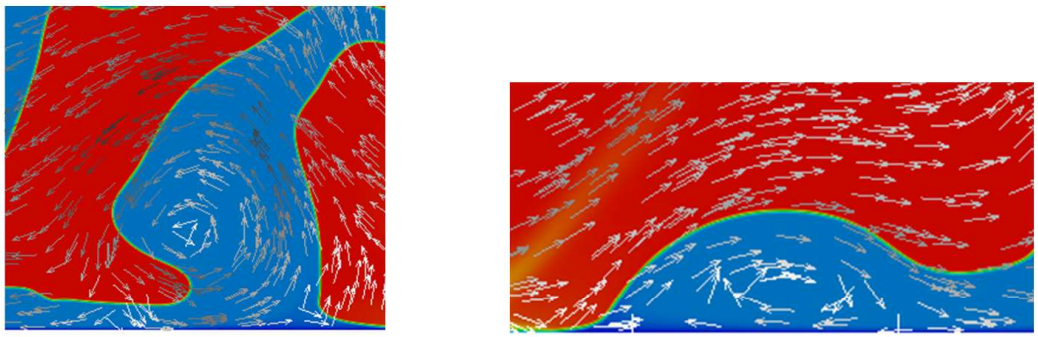

(b) Region P in (a)

(c) Region Q in (a)

Figure 2.31: Instantaneous distributions of (a) gas temperature, T, and velocity vector (represented by arrows), and enlarged views of (b) recatngle P and (c) rectangle Q for Case T-ins at $t = 2.0\,\mathrm{ms}$.

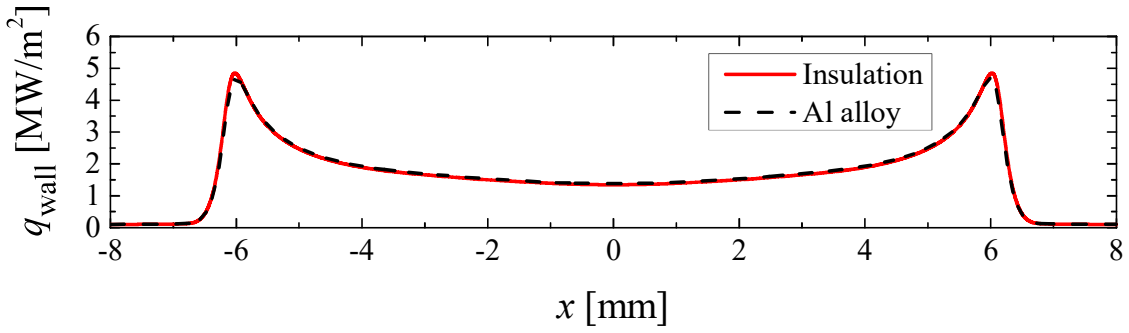

(a) Laminar case

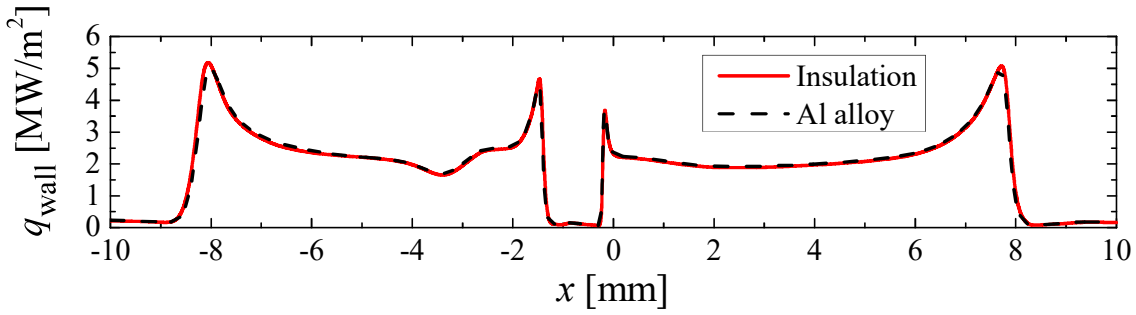

(b) Turbulent case (upper wall)

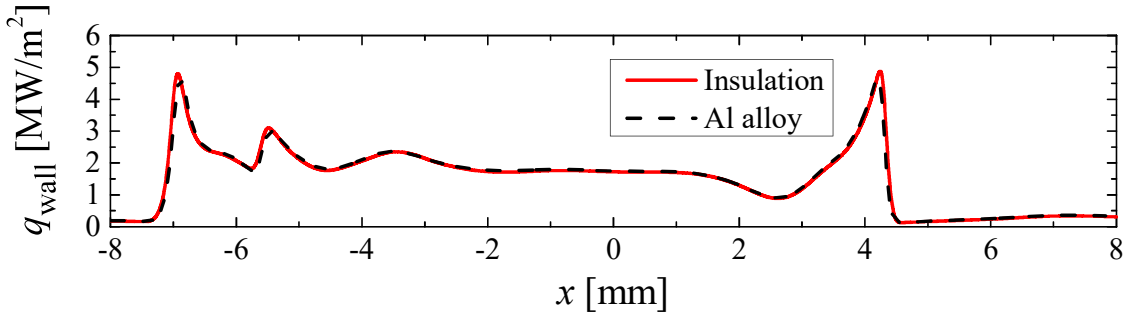

(c) Turbulent case (lower wall)

Figure 2.32: Comparisons of instantaneous distributions of wall heat fluxes, q_{wall}, on (a) both walls of Case L at $t = 3.5\,\mathrm{ms}$, (b) upper walls of Cases T-ins and T-Al at $t = 2.0\,\mathrm{ms}$, and (c) lower walls of Cases T-ins and T-Al at $t = 2.0\,\mathrm{ms}$.

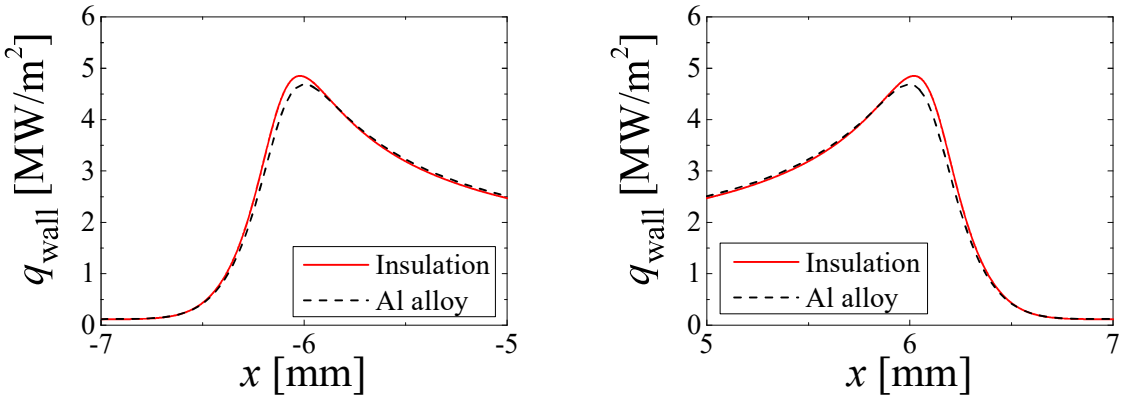

(a) Laminar case

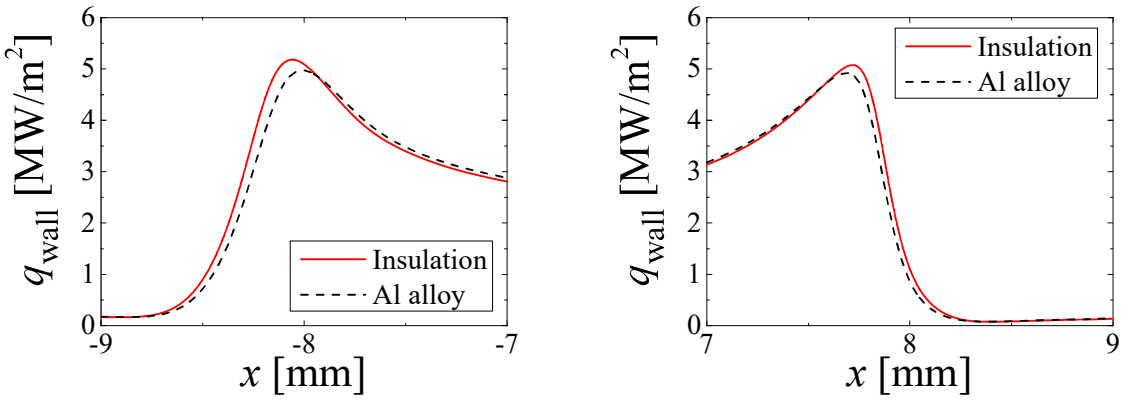

(b) Turbulent case (upper wall)

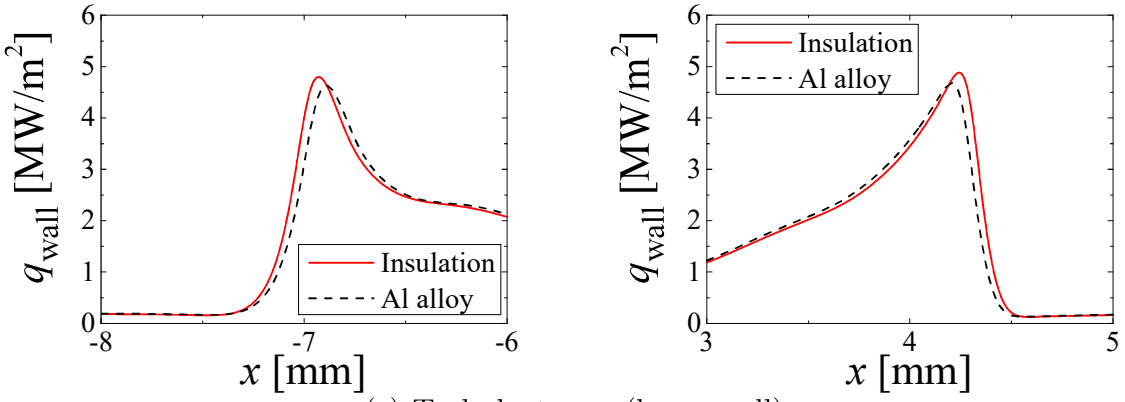

(c) Turbulent case (lower wall)

Figure 2.33: Enlarged views of Fig. 2.32 (a), (b) and (c) near peaks of wall heat flux, q_{wall}.

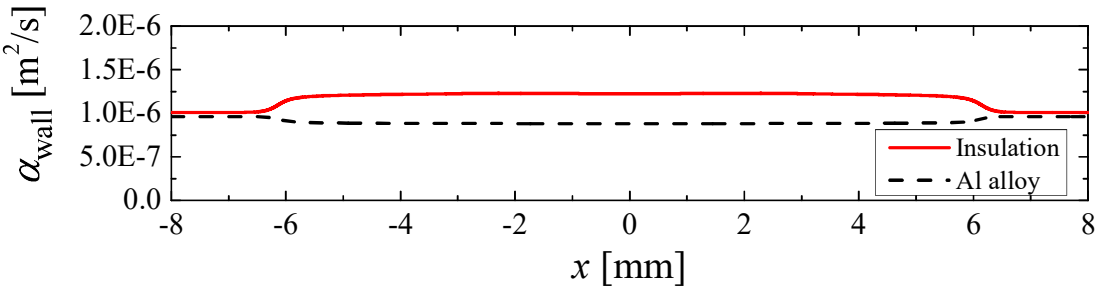

(a) Laminar case

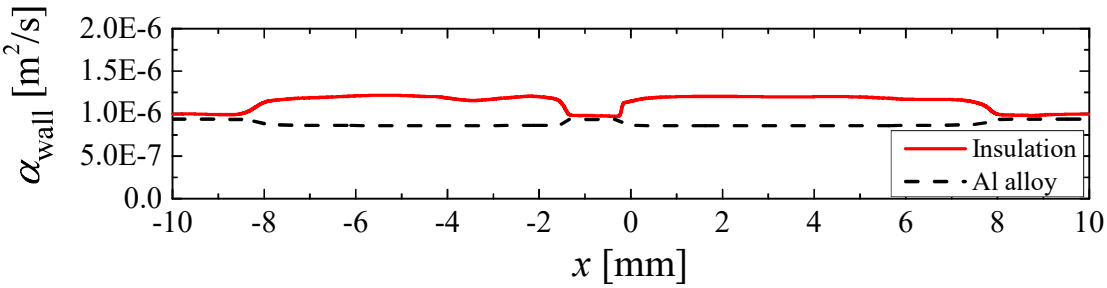

(b) Turbulent case (upper wall)

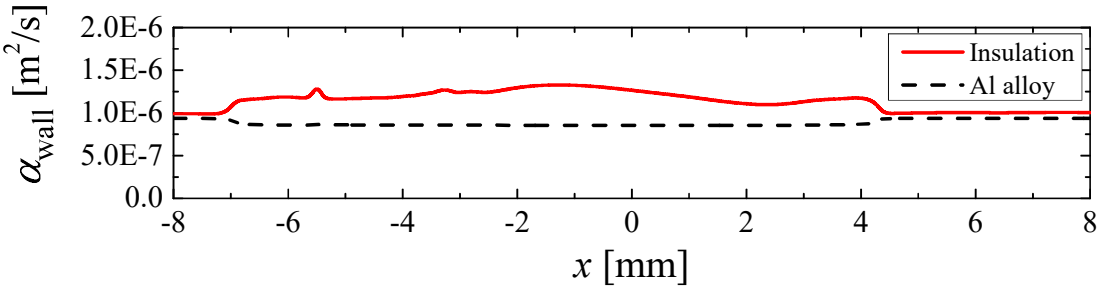

(c) Turbulent case (lower wall)

Figure 2.34: Comparisons of instantaneous distributions of gas thermal diffusivity, α_{wall}, on (a) both walls of Case L at $t = 3.5\,\mathrm{ms}$, (b) upper walls of Cases T-ins and T-Al at $t = 2.0\,\mathrm{ms}$, and (c) lower walls of Cases T-ins and T-Al at $t = 2.0\,\mathrm{ms}$.

2.4 Conclusions

In this study, the CHT analyses of premixed flames propagating toward walls were performed without employing any wall model in terms of one- and two-dimensional (1D and 2D) numerical simulations, and the FWI was investigated in detail. In the 1D numerical simulations, the effects of wall material, i.e., the insulation and Al alloy, on the wall heat flux are investigated for different fuels (C1 to C3 alaknes and H_2) at different equivalence ratios ($\phi = 0.6$, 0.8, 1.0, and 1.2) under different ambient pressure conditions (1, 2, and 4 MPa). In the 2D numerical simulations, on the other hand, the effect of turbulence on the wall heat flux was investigated. The main results obtained in this study can be summarized as follows.

1. For all the alkanes and H_2 flames, the temperature at the surface of the insulation wall increases more and faster than that of the Al alloy wall, and the heat loss through the wall is reduced by the insulation.

2. The heat loss reduction rate for the insulation wall to the Al alloy wall Λ becomes higher both with increase and decrease in the equivalence ratio from the stoichiometric ratio, regardless of the fuel. The value of Λ reaches up to 2.1%, and this order matches well with the existing experiment. The reason for this tendency of Λ against the equivalence ratio is explicitly explained by the time variations of the gas thermal conductivity and the gas temperature gradient in the vicinity of the wall, which control the heat flux through the wall.

3. For the methane flame, the insulation works more efficiently at higher pressure condition, and Λ reaches 1.8 % at 4 MPa.

4. In the 2D numerical simulations, for both laminar and turbulent cases, the wall heat fluxes are reduced by the insulation wall similarly to 1D numerical simulations, although the maximum wall heat flux values for turbulent cases are fluctuated because of turbulent eddies.

References

[1] O. Edenhofer. *Climate change 2014: mitigation of climate change*, volume 3. Cambridge University Press, 2015.

[2] H. Kosaka, Y. Wakisaka, Y. Nomura, Y. Hotta, M. Koike, K. Nakakita, and A. Kawaguchi. Concept of "temperature swing heat insulation" in combustion chamber walls, and appropriate thermo-physical properties for heat insulation coat. *SAE International Journal of Engines*, 6(1):142–149, 2013.

[3] Y. Wakisaka, M. Inayoshi, K. Fukui, H. Kosaka, Y. Hotta, A. Kawaguchi, and N. Takada. Reduction of heat loss and improvement of thermal efficiency by application of "temperature swing" insulation to direct-injection diesel engines. *SAE International Journal of Engines*, 9(3):1449–1459, 2016.

[4] H. Fujimoto, H. Yamamoto, M. Fujimoto, and H. Yamashita. A study on improvement of indicated thermal efficiency of ICE using high compression ratio and reduction of cooling loss. Technical report, SAE Technical Paper, 2011.

[5] A. Kikusato, K. Jin, and Y. Daisho. A numerical simulation study on improving the thermal efficiency of a spark ignited engine—part 1: Modeling of a spark ignited engine combustion to predict engine performance considering flame propagation, knock, and combustion chamber wall—. *SAE International Journal of Engines*, 7(1):96–105, 2014.

[6] R. Mari, B. Cuenot, J.-P. Rocchi, L. Selle, and F. Duchaine. Effect of pressure on hydrogen/oxygen coupled flame–wall interaction. *Combustion and Flame*, 168:409–419, 2016.

[7] M. Shahi, J. B. Kok, J. R. Casado, and A. K. Pozarlik. Transient heat transfer between a turbulent lean partially premixed flame in limit cycle oscillation and the walls of a can type combustor. *Applied Thermal Engineering*, 81:128–139, 2015.

[8] K. Bioche, L. Vervisch, and G. Ribert. Premixed flame–wall interaction in a narrow channel: impact of wall thermal conductivity and heat losses. *Journal of Fluid Mechanics*, 856:5–35, 2018.

[9] C. Koren, R. Vicquelin, and O. Gicquel. Multiphysics simulation combining large-eddy simulation, wall heat conduction and radiative energy transfer to predict wall temperature induced by a confined premixed swirling flame. *Flow, Turbulence and Combustion*, 101(1):77–102, 2018.

[10] F. Berni, G. Cicalese, and S. Fontanesi. A modified thermal wall function for the estimation of gas-to-wall heat fluxes in CFD in-cylinder simulations of high performance spark-ignition engines. *Applied Thermal Engineering*, 115:1045–1062, 2017.

[11] L. Zhang. Parallel simulation of engine in-cylinder processes with conjugate heat transfer modeling. *Applied Thermal Engineering*, 142:232–240, 2018.

[12] M. A. Ceviz, A. K. Sen, A. K. Küleri, and İ. V. Öner. Engine performance, exhaust emissions, and cyclic variations in a lean-burn si engine fueled by gasoline–hydrogen blends. *Applied Thermal Engineering*, 36:314–324, 2012.

[13] S. Lee, S. Park, C. Kim, Y.-M. Kim, Y. Kim, and C. Park. Comparative study on egr and lean burn strategies employed in an si engine fueled by low calorific gas. *Applied energy*, 129:10–16, 2014.

[14] J. P. Bhasker and E. Porpatham. Effects of compression ratio and hydrogen addition on lean combustion characteristics and emission formation in a compressed natural gas fuelled spark ignition engine. *Fuel*, 208:260–270, 2017.

[15] T. S. Hora, P. C. Shukla, and A. K. Agarwal. Particulate emissions from hydrogen enriched compressed natural gas engine. *Fuel*, 166:574–580, 2016.

[16] R. Sankaran, H. G. Im, E. R. Hawkes, and J. H. Chen. The effects of non-uniform temperature distribution on the ignition of a lean homogeneous hydrogen–air mixture. *Proceedings of the Combustion Institute*, 30(1):875–882, 2005.

[17] V. Kozlov, N. Titova, and I. Chechet. Modeling study of hydrogen or syngas addition on combustion and emission characteristics of hcci engine operating on isooctane. *Fuel*, 221:61–71, 2018.

[18] A. Gruber, R. Sankaran, E. Hawkes, and J. Chen. Turbulent flame–wall interaction: a direct numerical simulation study. *Journal of Fluid Mechanics*, 658:5–32, 2010.

[19] J. Pan, G. Shu, P. Zhao, H. Wei, and Z. Chen. Interactions of flame propagation, auto-ignition and pressure wave during knocking combustion. *Combustion and Flame*, 164:319–328, 2016.

[20] H. Terashima, A. Matsugi, and M. Koshi. End-gas autoignition behaviors under pressure wave disturbance. *Combustion and Flame*, 203:204–216, 2019.

[21] "Chemical-Kinetic Mechanisms for Combustion Applications", San Diego Mechanism web page, Mechanical and Aerospace Engineering (Combustion Research), University of California at San Diego, `http://web.eng.ucsd.edu/mae/groups/combustion/sdmech/sandiego20161214/sandiego20161214_mechCK.txt` .

[22] M. Ó Conaire, H. J. Curran, J. M. Simmie, W. J. Pitz, and C. K. Westbrook. A comprehensive modeling study of hydrogen oxidation. *International journal of chemical kinetics*, 36(11):603–622, 2004.

[23] W. F. Gale and T. C. Totemeier. *Smithells metals reference book*. Elsevier, 2003.

[24] R. Kurose. FK^3, `http://www.tse.me.kyoto-u.ac.jp/members/kurose/link_e.php`, 2020.

[25] V. Moureau, C. Bérat, and H. Pitsch. An efficient semi-implicit compressible solver for large-eddy simulations. *Journal of Computational Physics*, 226(2):1256–1270, 2007.

[26] V. Titarev and E. Toro. WENO schemes based on upwind and centred TVD fluxes. *Computers & Fluids*, 34(6):705–720, 2005.

[27] S. Gottlieb and C. W. Shu. Total variation diminishing Runge-Kutta schemes. *Mathematics of computation of the American Mathematical Society*, 67(221):73–85, 1998.

[28] P. N. Brown, G. D. Byrne, and A. C. Hindmarsh. VODE: A variable-coefficient ODE solver. *SIAM journal on scientific and statistical computing*, 10(5):1038–1051, 1989.

[29] R. J. Kee, G. Dixon-Lewis, J. Warnatz, M. E. Coltrin, and J. A. Miller. A Fortran computer code package for the evaluation of gas-phase multicomponent transport properties. *Sandia National Laboratories Report SAND86-8246*, 1986.

[30] R. J. Kee, F. M. Rupley, and J. A. Miller. Chemkin-II: A Fortran chemical kinetics package for the analysis of gas-phase chemical kinetics. *Sandia National Laboratories Report SAND89-8009*, 1989.

[31] G. E. Andrews and D. Bradley. The burning velocity of methane-air mixtures. *Combustion and flame*, 19(2):275–288, 1972.

[32] R. Masuda and T. Ikedo. private communication, 2019.

[33] B. Franzelli, E. Riber, L. Y. Gicquel, and T. Poinsot. Large eddy simulation of combustion instabilities in a lean partially premixed swirled flame. *Combustion and Flame*, 159(2):621–637, 2012.

[34] H. Pitsch. FlameMaster: A C++ computer program for 0D combustion and 1D laminar flame calculations. *Cited in*, 81, 1998.

[35] G. P. Smith, D. M. Golden, M. Frenklach, N. W. Moriarty, B. Eiteneer, M. Goldenberg, C. T. Bowman, R. K. Hanson, S. Song, W. Gardiner Jr, et al. GRI-Mech 3.0, `http://www.me.berkeley.edu/gri_mech`. 1999.

[36] R. S. Rogallo. Numerical experiments in homogeneous turbulence, (1981). *NASA Technical Memorandum 81315*, 1981.

[37] G. Bansal, A. Mascarenhas, and J. H. Chen. Direct numerical simulations of autoignition in stratified dimethyl-ether (DME)/air turbulent mixtures. *Combustion and Flame*, 162(3):688–702, 2015.

[38] R. N. Roy, M. Muto, and R. Kurose. Direct numerical simulation of ignition of syngas (h_2/co) mixtures with temperature and composition stratifications relevant to HCCI conditions. *International Journal of Hydrogen Energy*, 42(41):26152–26161, 2017.

[39] N. Peters. Turbulent combustion, 2001.

[40] T. Hara, M. Muto, T. Kitano, R. Kurose, and S. Komori. Direct numerical simulation of a pulverized coal jet flame employing a global volatile matter reaction scheme based on detailed reaction mechanism. *Combustion and Flame*, 162(12):4391–4407, 2015.

[41] Y. Hu and R. Kurose. Nonpremixed and premixed flamelets LES of partially premixed spray flames using a two-phase transport equation of progress variable. *Combustion and Flame*, 188:227–242, 2018.

[42] A. L. Pillai and R. Kurose. Combustion noise analysis of a turbulent spray flame using a hybrid DNS/APE-RF approach. *Combustion and Flame*, 200:168–191, 2019.

[43] U. Ahmed, A. L. Pillai, N. Chakraborty, and R. Kurose. Statistical behavior of turbulent kinetic energy transport in boundary layer flashback of hydrogen-rich premixed combustion. *Physical Review Fluids*, 4(10):103201, 2019.

[44] K. Yunoki, R. Kai, S. Inoue, and R. Kurose. Numerical Simulation of CO Concentration on Flame Propagation in the Vicinity of the Wall-Validity of Non-Adiabatic FGM Approach. *International Journal of Gas Turbine, Propulsion and Power Systems*, 11(3), 2020.

[45] B. J. McBride, S. Gordon, and M. A. Reno. Coefficients for calculating thermodynamic and transport properties of individual species. *NASA Technical Memorandum 4513*, 1993.

Nomenclature

c	: Specific heat capacity [J/(K kg)]	**Subscripts**	
D	: Diffusion coefficient [m^2/s]	Al	: Al alloy wall
h	: Specific enthalpy [J/kg]	b	: Burnt gas
Ka	: Karlovitz number [-]	ini	: Initial value
l	: Integral length scale [m]	ins	: Insulation wall
p	: Pressure [Pa]	k	: Species k
q	: Heat flux [W/m^2]	s	: Solid wall
Re_l	: Turbulent Reynolds number [-]	$wall$	: Wall surface
S_L	: Laminar burning velocity [m/s]		
T	: Temperature [K]		
t	: Time [s]		
$\boldsymbol{u}$	: Velocity [m/s]		
u'_{rms}	: Velocity root mean square [m/s]		
$\boldsymbol{V}$	: Diffusion velocity [m/s]		
X	: Mole fraction [-]		
Y	: Mass fraction [-]		
α	: Thermal diffusivity [m^2/s]		
δ	: Flame thickness [m]		
Λ	: Heat loss reduction rate [-]		
λ	: Thermal conductivity [W/(m K)]		
ρ	: Density [kg/m^3]		
τ	: Time [s]		
$\boldsymbol{\tau}$	: Viscous stress tensor [$kg/(m^2\ s^2)$]		
ϕ	: Equivalence ratio [-]		
$\dot{\omega}$	: Reaction rate [1/s]		

Chapter 3

Numerical analysis of premixed flame-wall interaction in turbulent channel flow

3.1 Introduction

In this chapter, the near-wall surface density fucntion $|\nabla c|$ statistics is investigated based on DNS.

To reduce the CO_2 emission from combustion devices such as gas turbine engines, automobile engines, and furnaces, the improvement of their fuel efficiency is necessary. As one way to achieve this, such combustion devices have been made smaller and lighter. As a result of the reduction in the size of the combustion chamber, the flame is more likely to interact with the chamber wall. Therefore, the fundamental physical understanding of the flame-wall interaction (FWI) plays a pivotal role in the design of modern combustors. The flame in the vicinity of the wall is strongly affected by the heat flux through the wall, which leads to flame quenching. In contrast, the flame modifies the flow field near the wall, which in turn influences the wall heat flux [1]. Hence, in the combustor, the presence of walls alters the turbulence structure, which is further affected by the presence of the flame near the wall also alters turbulence flow [2]. However, the

information on the behavior of turbulence and combustion processes during FWI in a fully developed boundary layer is limited, and consequently, the modeling is currently in its infancy [3–10] .

There are several experimental [7, 8, 11–16] and numerical [2–6, 9, 10, 17–40] studies on the FWI for turbulent premixed flames. For the head-on quenching (HOQ) configuration, Poinsot et al. [17] performed a two-dimensional direct numerical simulation (DNS) based on a single step irreversible Arrhenius type chemistry. This analysis was subsequently extended for two-dimensional HOQ of hydrogen-air flames using a detailed chemical mechanism by Dabireau et al. [20]. The HOQ of statistically planar flames by inert walls [4–6, 24–26] and the FWI of statistically planar flames impinging on inert walls [27, 28, 30] were analyzed by Chakraborty and co-workers using three-dimensional DNS for both unity and non-unity Lewis number conditions. These analyses provided important physical insights into the near-wall flame structure [4, 6, 9], flow topology [25], enstrophy distribution [24, 26], wall heat flux [4–6, 9, 28], quenching distance [4–6, 9, 28], and reactive scalar gradient [27, 37] and flame propagation [36] statistics, which were subsequently utilized for purpose of the modification of the flame surface density (FSD) [4–6, 9] and scalar dissipation rate (SDR) [4, 6, 9] based mean reaction rate closures to account for flame quenching in the vicinity of the wall. Both FSD and SDR based modeling depend on the statistical behavior of the surface density function (SDF), which represents the norm of the gradient of progress variable $|\nabla c|$ [41]. Thus, the evolution of the SDF in the case of FWI of statistically planar flames impinging on inert isothermal walls was analyzed for different Lewis numbers by Konstantinou et al. [37]. The alignment of ∇c with local principal strain rates in the near-wall region during the FWI and its implications on the modeling were analyzed by Zhao et al. [27]. The statistical behavior of the wall heat flux, which leads to flame quenching, and the formation of CO and NOx formed the basis of several investigations [32, 33, 35, 38]. For example, CO production in the near-wall region was analyzed based on unsteady two-dimensional HOQ simulation by Jiang et al. [32], Palulli et al. [33], and Yunoki et al. [38]. Kai et al. [35] performed two-dimensional DNS for turbulent spherical flame

and investigated the effect of wall material property on the wall heat flux.

It is not straightforward to characterize boundary layer in the HOQ configuration, but the mean flow shear in turbulent boundary layers can significantly affect turbulent premixed FWI in industrial combustors. Bruneaux et al. [18] pioneered the analysis of FWI in turbulent boundary layers using constant density three-dimensional DNS of premixed flames propagating toward the wall in a channel flow configuration for at friction Reynolds number $Re_\tau = 180$. Bruneaux et al. [18] revealed the role of horseshoe vortices in premixed FWI in turbulent boundary layers. The same authors [3] also subsequently investigated the FSD evolution during FWI within turbulent boundary layers using this DNS data and proposed near-wall modifications to the mean reaction rate closure and unclosed terms of the FSD transport equation. The analysis by Bruneaux et al. [3, 18] has recently been extended by Ahmed et al. [39] by considering three-dimensional variable-density DNS of statistically planar flame propagation across the turbulent boundary layer toward an inert isothermal wall. This data has been utilized to assess the algebraic FSD closure and the FSD based mean reaction rate modeling in the near-wall region.

In the case of premixed combustion of high hydrogen content fuels, the high flame propagation rate in the low-velocity near-wall region within turbulent boundary layers can lead to flashback, as reported in some previous experiments: Eichler et al. [11] and Goldmann and Dinkelacker [16] performed experiments for hydrogen and hydrogen-ammonia flames, respectively. Gruber et al. [22, 29] and Kitano et al. [23] performed three-dimensional DNS of flashback for hydrogen-air flames in turbulent boundary layers at $Re_\tau = 180$ and 120, respectively. Ahmed et al. [31, 34] investigated the budgets of turbulent kinetic energy transport equation and SDF evolution based on the DNS database of Kitano et al. [23].

To understand the FWI under a statistically steady-state within the turbulent boundary layer, wall interaction of turbulent premixed V-flame in the turbulent boundary layer has also been analyzed [10, 21, 39, 40] where the flames obliquely interact with walls. Jainski et al. [8] measured the FSD from experimental data for the FWI of turbulent

V-shaped methane-air flame. Kosaka et al. [14] experimentally investigated the correlations between local heat release rate, flame curvature, and wall-normal quenching distance for the FWI of V-shaped methane- and dimethyl ether-air flames. Zentgraf et al. [15] experimentally investigated the correlations between CO and CO_2 and temperature near the wall for V-shaped dimethyl ether-air FWI. In numerical studies, in contrast, Alshaalan and Rutland [2, 19] performed DNS of turbulent channel-Couette flow at $Re_\tau = 38$ and investigated the effect of streamwise vortex on wall heat flux, statistical behaviors of turbulent scalar flux and FSD, and proposed modifications to the mean reaction closure. Gruber et al. [21] carried out three-dimensional complex chemistry DNS of turbulent V-shaped hydrogen-air flame interaction with isothermal inert walls to analyze the flame structure and flame propagation in the near-wall region along the statistical behavior of the wall heat release rate. Ahmed et al. [39] performed three-dimensional DNS of V-flame in the turbulent channel flow at $Re_\tau = 110$ interacting with adiabatic and isothermal inert walls and demonstrated the effects of wall boundary condition on the SDF evolution in boundary layer during premixed FWI. Ahmed et al. [10] assessed the applicability of Bray-Moss-Libby formulation for oblique quenching of turbulent V-shaped premixed flames and for statistically planar premixed flame propagation across the turbulent boundary layer toward an inert isothermal wall. Jiang et al. [40] performed three-dimensional DNS of V-flame in turbulent channel flow interacting with two different isothermal walls and investigated CO formation near the wall. Although all the analyses provided significant physical and modeling insights for turbulent premixed FWI, these studies were conducted for moderate values of friction Reynolds number (i.e., $Re_\tau < 180$) and thus it is necessary to analyze the fundamental aspects of FWI in turbulent boundary layers for higher values of Re_τ.

In this study, the near-wall SDF $|\nabla c|$ statistics is investigated based on the three-dimensional DNS of turbulent premixed V-flame interacting with an isothermal inert wall in the wall-bounded turbulent channel flow at $Re_\tau = 395$ for the stoichiometric methane-air flame, as the SDF is closely related to the generalized FSD $\Sigma_{gen} = \overline{|\nabla c|}$ (where the overbar indicates the Reynolds averaging/LES filtering operation, as appro-

priate) [42] and SDR $N_c = D\nabla c \cdot \nabla c$ [43], which are required for the purpose of modeling. For this purpose, an auxiliary non-reacting flow DNS has been conducted, which was subsequently utilized for the inlet flow field specification for the DNS of V-flame. The methane-air combustion is represented by two-step global reaction model [44] under the unity Lewis number assumption. It was previously demonstrated [39] that the behaviors of heat release rate near the wall obtained considering detailed reaction model is not reproduced by simple reaction model because of the lack of the intermediate species, but the detailed reaction model does not affect the SDF statistics, wall heat flux magnitude, flame quenching distance, and flame-turbulence interaction in the vicinity of the isothermal wall. Lai et al. [9] has also shown that the FSD and SDR models based on the DNS employing simple reaction model are valid in the presence of detailed reaction mechanism. Moreover, Jainski et al. [8] has shown that the FSD model developed on simple reaction model can capture the global features of the experimentally obtained near-wall FSD profile. Therefore, a two-step chemical mechanism [45] can be used for the analysis of the SDF evolution in premixed FWI within turbulent boundary layer for a high value of friction Reynolds number $Re_\tau = 395$.

3.2 Numerical simulation

3.2.1 Governing equations

The governing equations for conservation of mass, momentum, energy, and mass fraction of chemical species are written as

$$\frac{\partial \rho}{\partial t} + \nabla \cdot (\rho \boldsymbol{u}) = 0 \tag{3.1}$$

$$\frac{\partial \rho \boldsymbol{u}}{\partial t} + \nabla \cdot (\rho \boldsymbol{u}\boldsymbol{u}) = -\nabla p + \nabla \cdot \boldsymbol{\tau} \tag{3.2}$$

$$\frac{\partial \rho H}{\partial t} + \nabla \cdot (\rho H \boldsymbol{u}) = \frac{\partial p}{\partial t} + \boldsymbol{u} \cdot \nabla p + \nabla \cdot (\rho D_H \nabla H) + \boldsymbol{\tau} : \nabla \boldsymbol{u} \tag{3.3}$$

$$\frac{\partial \rho Y_k}{\partial t} + \nabla \cdot (\rho Y_k \boldsymbol{u}) = \nabla \cdot (\rho D_k \nabla Y_k) + \rho \dot{\omega}_k \tag{3.4}$$

where ρ is the density, $\boldsymbol{u}$ is the velocity, p is the pressure, $\boldsymbol{\tau}$ is the viscous stress, and H is the specific enthalpy, and Y_k is the mass fraction of chemical species k. Here, h is sum of specific formation enthalpy and specific sensible enthalpy. D_H is the thermal diffusivity given by $D_H = \lambda/\rho c_p$. Here, λ and c_p are the thermal conductivity and the specific heat capacity at a constant pressure, respectively. D_k is the diffusion coefficient of species k, and is evaluated under the unity Lewis number assumption as $D_k = \lambda/\rho c_p$. $\dot{\omega}_k$ is the production rate of species k. The methane reaction is represented by a two-step reaction mechanism [44], which consists of the following reactions.

$$\mathrm{CH_4} + \frac{3}{2}\mathrm{O_2} \longrightarrow 2\,\mathrm{H_2O} + \mathrm{CO}, \tag{3.5}$$

$$\mathrm{CO} + \frac{1}{2}\mathrm{O_2} \rightleftharpoons \mathrm{CO_2}. \tag{3.6}$$

3.2.2 Numerical setups

Before performing the DNS of V-flame, an auxiliary DNS of non-reacting flow is conducted, which is subsequently utilized for the inlet flow field specification for the DNS of V-flame. Figure 3.1(a) shows the computational domain and conditions for the DNS of non-reacting flow. In the DNS of non-reacting flow, a fully developed wall-bounded turbulent flow is generated by imposing a periodic boundary condition in x-direction while maintaining a constant bulk velocity u_{Bulk} of 55m/s on the inlet plane. The inflow gas is the stoichiometric methane-air premixed gas at 750K. The ambient pressure is 0.1 MPa. The no-slip isothermal (750K) boundary condition is applied in y-direction, and the periodic boundary condition is applied in z-direction. The friction Reynolds number $Re_\tau = u_\tau h/\nu$ is approximately 395, where u_τ is the friction velocity, h is the channel half height , ν is the kinetic viscosity. The bulk Reynolds number $Re_{\mathrm{Bulk}} = u_{\mathrm{Bulk}} 2h/\nu$ is approximately 14,500. The computational domain is discretized on a non-uniform staggered grid with a Cartesian coordinate. For the turbulence generation region, the grid resolution is 250 µm in x-direction ($\Delta x^+ = 10$), 10–30 µm from the wall to the center of

the channel in y-direction ($\Delta y^+ = 0.4$–1.2), and 30 µm in z-direction ($\Delta z^+ = 1.2$). Here, the superscript + represents the wall-unit length. It should be noted that the region $y^+ < 1$ has at least two grid points to ensure appropriate resolution of the boundary layer, as recommended by Moser et al. [46].

Figure 3.1(b) shows the computational domain and conditions for the DNS of V-flame. The domain consists of two regions (i.e., flame and buffer regions). The buffer region is used to remove the unrealistic pressure reflection at the outlet boundary. In the flame region, a flame holder is placed in a fully developed wall-bounded turbulent flow to stabilize the flame. It is placed at 5mm above the bottom wall ($y^+ = 197.5$, $y = 0.5h$) and at 85mm from the inlet plane. The radius of the flame holder R_{fth} is approximately 0.86 δ_{th}. Here, δ_{th} is the laminar flame thermal thickness and is defined as $\delta_{th} = (T_b - T_u)/|\nabla T|_{L,max}$, where T is the temperature, and the subscripts b, u, and L represent quantities for the fully burnt gas, unburnt gas, and laminar planar flame, respectively. Burnt gas composition and temperature are imposed at the flame holder. The computational domain is discretized on a non-uniform staggered grid with a Cartesian coordinate. The origin of the coordinate system is located at the flame holder in x-direction, at the bottom wall in y-direction, and at the center in z-direction. The grid configuration in y- and z-directions is same as the DNS of non-reacting flow. The minimum grid spacing in x-direction is 30 µm and is arranged from $x = -0.12h$ to $10.5h$. The δ_{th} is resolved by approximately 10 grid points with this grid spacing. In the buffer region, the grid spacing in x-direction is stretched. As the inflow characteristics of the flame region, the outflow characteristics of the DNS of the non-reacting flow are given. At the outflow boundary, the pressure is constant at the ambient pressure of 0.1 MPa, and the Neumann boundary condition is imposed for the other physical quantities. The no-slip isothermal (750K) boundary condition is applied in y-direction. For the pressure and species mass fraction, Neumann boundary condition is imposed at the wall. The periodic boundary condition is applied in z-direction.

The numerical simulations are performed using the in-house code FK^3 [23, 35, 38, 47]. This code is based on the pressure-based semi-implicit solver for compressible flows,

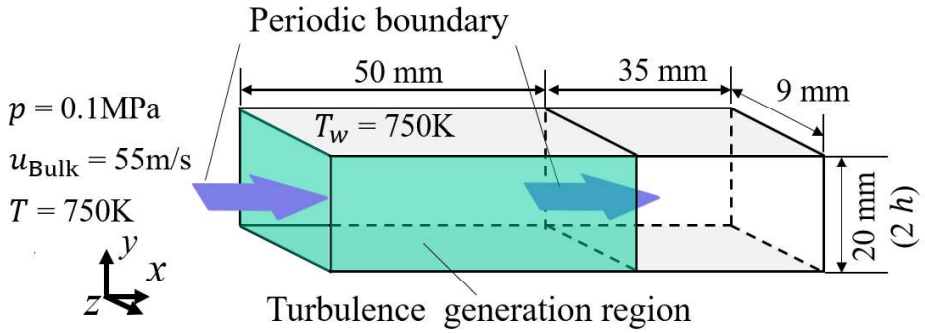

(a) Nonreactive flow

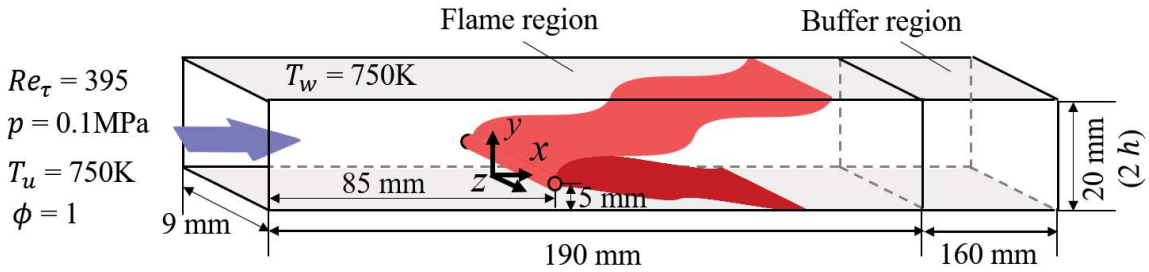

(b) V-flame

Figure 3.1: Schematics of computational domains and conditions for DNS of (a) non-reacting flow and (b) V-flame.

which employs a fractional-step method [48]. The spatial derivative of the convective term in the momentum equation is approximated with a fourth-order central difference scheme. The WENO scheme [49] is applied to the convective terms in the governing equations of the scalar quantities. In the vicinity of the wall, a low-order one-sided scheme is used for the spatial derivatives. The time integration of these convective terms is performed using the third-order TVD Runge-Kutta method [50]. For all simulations, time step is 0.1 µs.

The CPU time required for the DNS of non-reacting flow and V-flame was approximately 0.25 and 1.26 million hours by parallel computation with 1,488 and 3,000 cores (actual time was 168 and 420 hours), respectively, on a Cray XC40 supercomputer at Kyoto University.

3.3 Mathematical background

In this study, the progress variable c is defined in terms of the mass fraction of H_2O as $c = (Y_{H2O} - Y_{H2O,u})/(Y_{H2O,b} - Y_{H2O,u})$. The conservation equation of progress variable c is given as

$$\frac{\partial \rho c}{\partial t} + \nabla \cdot (\rho c \boldsymbol{u}) = \nabla \cdot (\rho D_c \nabla c) + \rho \dot{\omega}_c, \tag{3.7}$$

where D_c is the diffusion coefficient for c. In this study, Lewis number is assumed to be unity; therefore, D_c is given by $D_c = \lambda/\rho c_p$. Eq.(3.7) can also be represented using the SDF for a given c isosurface as

$$\frac{\partial c}{\partial t} + \boldsymbol{u} \cdot \nabla c = S_d |\nabla c|, \tag{3.8}$$

where S_d is the displacement speed and is defined as [51]

$$S_d = \frac{(\rho \dot{\omega}_c + \nabla \cdot (\rho D_c \nabla c))}{\rho |\nabla c|}. \tag{3.9}$$

The displacement speed is affected by the balance of reaction and diffusion and SDF.

The conservation equation of SDF is represented as

$$\frac{\partial |\nabla c|}{\partial t} + (\boldsymbol{u} + S_d \boldsymbol{n}) \cdot \nabla (|\nabla c|) = -(a_n + \boldsymbol{n} \cdot \nabla S_d) |\nabla c|. \tag{3.10}$$

Here, $\boldsymbol{n} = -\nabla c/|\nabla c|$ is the flame normal vector, and $a_n = \boldsymbol{n}\boldsymbol{n} : \nabla \boldsymbol{u}$ is the normal strain rate. Because $\boldsymbol{u} + S_d \boldsymbol{n}$ represents the propagation speed of given c isosurface, Eq.(3.10) can be transformed as [52]

$$\frac{1}{|\nabla c|} \frac{d|\nabla c|}{dt} = -(a_n + \boldsymbol{n} \cdot \nabla S_d) = -a_n^{eff}, \tag{3.11}$$

where d/dt is the total derivative associated with flame movement, and a_n^{eff} is the effective normal strain rate. Therefore, the time evolution of SDF is governed by a_n^{eff}. In this study, the mean values of SDF, a_n^{eff}, a_n, and $\boldsymbol{n} \cdot \nabla S_d$ have been analyzed during FWI close to the wall.

3.4 Results and discussion

3.4.1 Flow field and flame behavior

Figure 3.2 shows the profiles of the mean streamwise velocity and root mean square values of velocity fluctuations in the wall normal direction obtained by the DNS of non-reacting flow. The obtained results are compared with the previous DNS by Moser et al. [46] and Abe et al. [53] at $Re_\tau = 395$. The profiles of present DNS match well with the previous DNS, particularly for $y^+ < 100$.

Figure 3.3 shows the instantaneous flame and turbulence behaviors at $t = 4.3\,\mathrm{ms}$. The flame surface is represented by the isosurface of the progress variable $c = 0.5$ colored in red. The white isosurface represents the invariant of velocity gradient tensor $Q^* = 1\times10^8$ $1/\mathrm{s}^2$. Here, Q^* is defined as $Q^* = (\Omega_{ij}\Omega_{ij} - S_{ij}S_{ij})/2$, where $S_{ij} = (\partial u_i/\partial x_j + \partial u_j/\partial x_i)/2$, and $\Omega_{ij} = (\partial u_i/\partial x_j - \partial u_j/\partial x_i)/2$ are the strain rate tensor, and rotation rate tensor, respectively. Positive Q^* value represents the dominance of the rotational motion over the strain deformation. The flame is stabilized at the flame holder and is distorted by developed wall turbulence. The distorted flame interacts with the bottom wall at approximately $4 < x/h < 6$. For the turbulence structure, the strong vortices decrease in the burnt gas.

To evaluate the accuracy of the DNS of V-flame, a quenching Peclet number Pe_Q is quantified. The Pe_Q is the normalized value of quenching distance δ_Q and is defined using Zel'dovich flame thickness $\delta_Z = \alpha_u/S_L$ as $Pe_Q = \delta_Q/\delta_Z$. Here, α_u is the thermal diffusivity for unburnt gas, and S_L is the laminar burning velocity. In this study, δ_Q is defined as the minimum wall-normal distance to the isosurface of non-dimensional temperature $T^* = 0.75$ according to the previous study [39]. Here, T^* is defined as $T^* = (T - T_u)/(T_{ad} - T_u)$ where T_{ad} is the adiabatic flame temperature. S_L and T_{ad} used to calculated Pe_Q is obtained from the one-dimensional simulation of laminar planar flame in HOQ configuration. The minimum Pe_Q for the present DNS at $Re_\tau = 395$ is 1.96 and is close to the minimum Pe_Q of 2.02 at $Re_\tau = 110$ [39]. The minimum Pe_Q for the one-dimensional HOQ flame is also calculated and is compared with the previous

study [39]. The obtained value is 2.20 and is almost the same as 2.19 obtained in the previous study [39].

Figure 3.4 shows the Favre averaged distributions of temperature, enthalpy, heat release rate, and mass fractions of chemical species. Figure 3.5 shows the isolines of Favre averaged progress variable $\tilde{c}$. The lower flame brush is thinner than that of upper flame brush. Accordingly, the averaged heat release rate of lower flame is higher than that of upper flame at same streamwise location. The isolines of $\tilde{c} = 0.1, 0.5, 0.9$ touch the wall at approximately $x/h = 4, 5, 6$. Therefore, thermal boundary layer develops on the bottom wall in the downstream region for $x/h > 5$ as shown in Fig.3.4(a). The thickness of the low enthalpy layer on the bottom wall increases at approximately $4 < x/h < 6$, and at $x/h = 10.5$, the heat loss is observed up to $y/h = 0.2$ ($y^+ = 79$) from the bottom wall surface. Moreover, the heat release rate disappears near the wall for $x/h > 7$ because of the heat loss through the wall. In addition to the averaged distributions, Fig.3.6 shows the instantaneous distributions of the same variables shown in Fig.3.4 at $z/h = 0$ at $t = 4.45\,\mathrm{ms}$. The folded flame is observed at approximately $4 < x/h < 5$, where the unburnt methane pockets appear surrounded by the burnt gas.

To investigate the flame behavior in the vicinity of the wall, Fig.3.7 shows the time series of the isosurfaces of $c = 0.5$ and $Q^* = 1.0 \times 10^8\ 1/\mathrm{s}^2$ near the bottom wall. The isosurface of $c = 0.5$ protrudes forward and upward in the vicinity of the wall due to near-wall turbulent structures (e.g. ejections). The high values of vorticity are observed on the unburnt side of the protruded isosurface of $c = 0.5$ as vorticity magnitude drops from the unburned gas to the burned gas side due to the increase in kinematic viscosity and dilatation rate effects.. In the downstream, the isolated unburnt gas pockets are consumed away from the wall where heat loss effects remain weak. Figure 3.8 shows the instantaneous distributions of c, isoline of $Q^* = 1 \times 10^8\ 1/\mathrm{s}^2$, and velocity vector colored by y-component of velocity vector on y-z planes at $x/h = 1.8$, 3.3, 3.6, and 5.4. The locations of these cross-sections are shown in Fig.3.7(a). The magenta and black circles indicate the sweep and ejection. It is obviously shown that the sweep enhances the flame

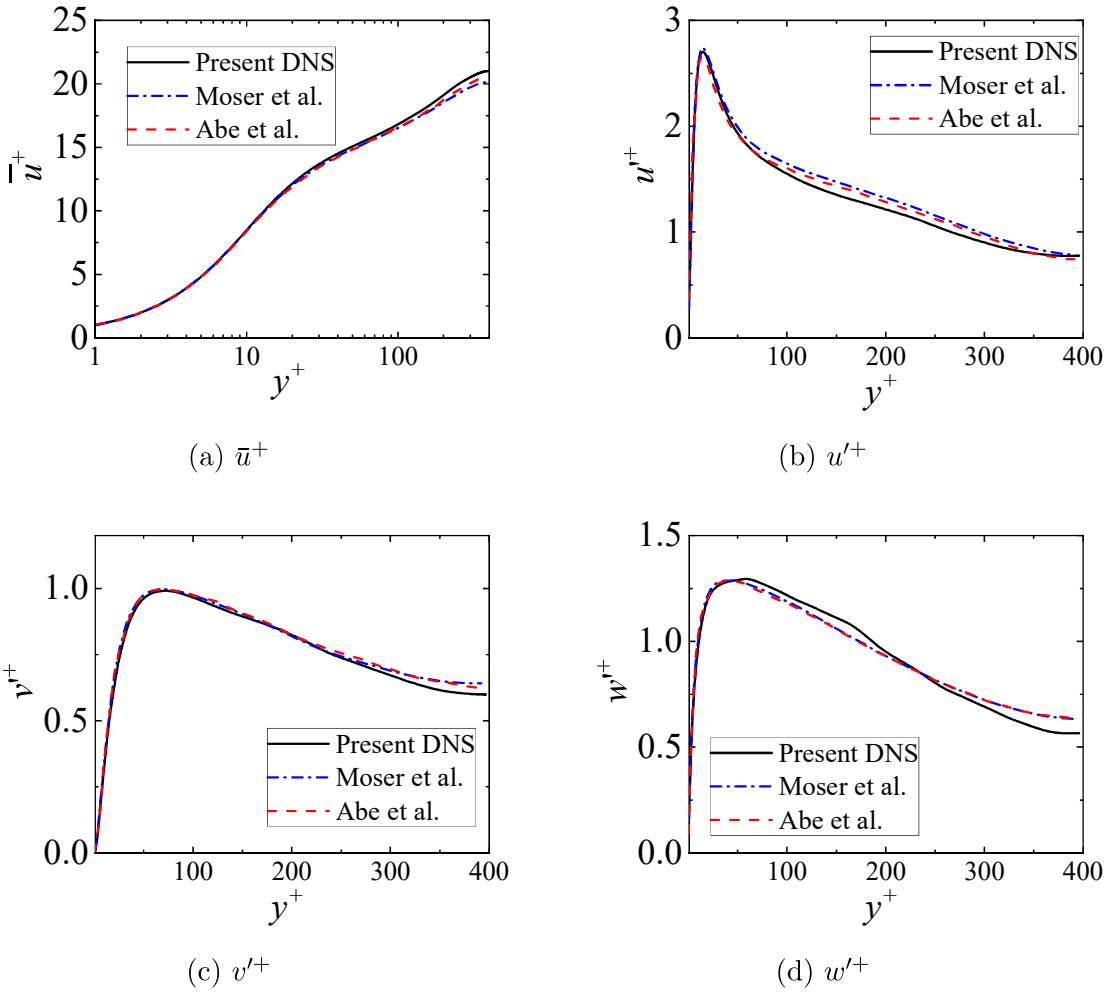

(a) $\bar{u}^+$ (b) u'^+

(c) v'^+ (d) w'^+

Figure 3.2: Profiles of (a) mean mainstream velocity, $\bar{u}^+$, and (b)-(d) root mean square values of velocity fluctuations, u'^+, v'^+, w'^+, in wall normal direction for DNS of non-reacting flow. The results of present DNS are compared with the previous DNS by Moser et al. [46] and by Abe et al. [53].

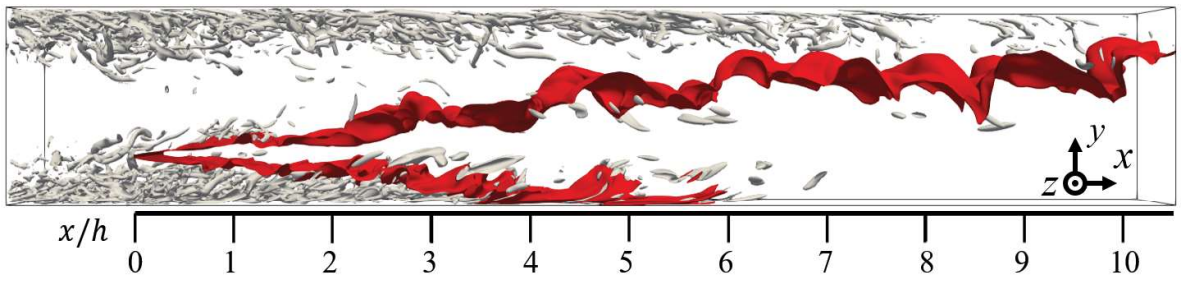

Figure 3.3: Instantaneous isosurfaces of progress variable ($c = 0.5$, colored in red) and invariant of velocity gradient tensor ($Q^* = 1 \times 10^8$ 1/s^2, colored in white) at $t = 4.3$ ms.

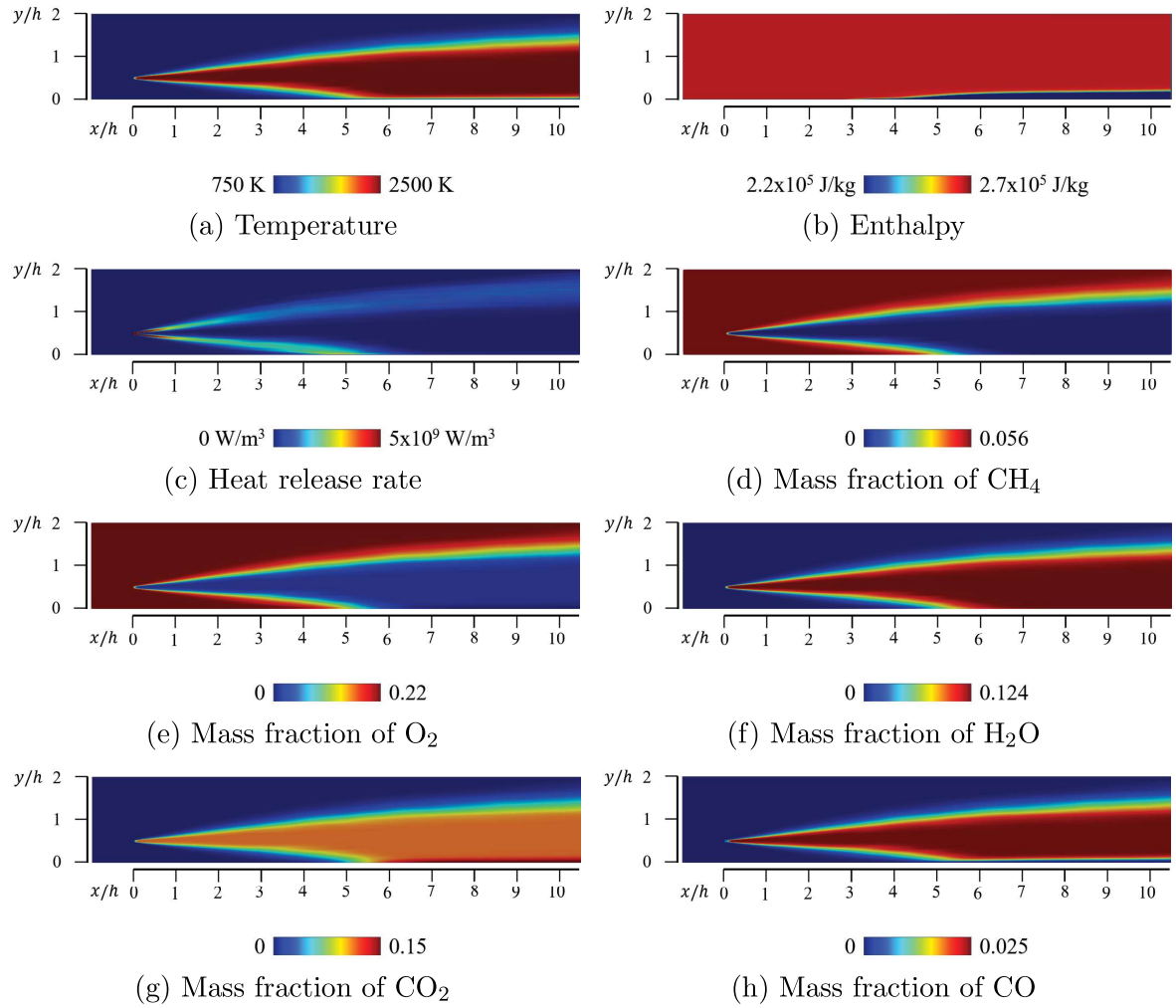

(a) Temperature (b) Enthalpy

(c) Heat release rate (d) Mass fraction of CH_4

(e) Mass fraction of O_2 (f) Mass fraction of H_2O

(g) Mass fraction of CO_2 (h) Mass fraction of CO

Figure 3.4: Favre averaged distributions of (a) temperature, (b) enthalpy, (c) heat release rate, and (d)-(h) mass fractions of CH_4, O_2, H_2O, CO_2, and CO.

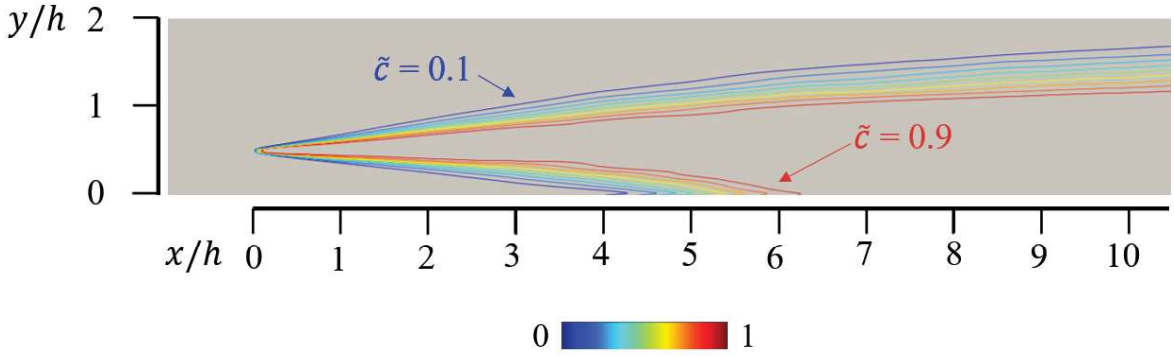

Figure 3.5: Isolines of Favre averaged progress variable $\tilde{c}$.

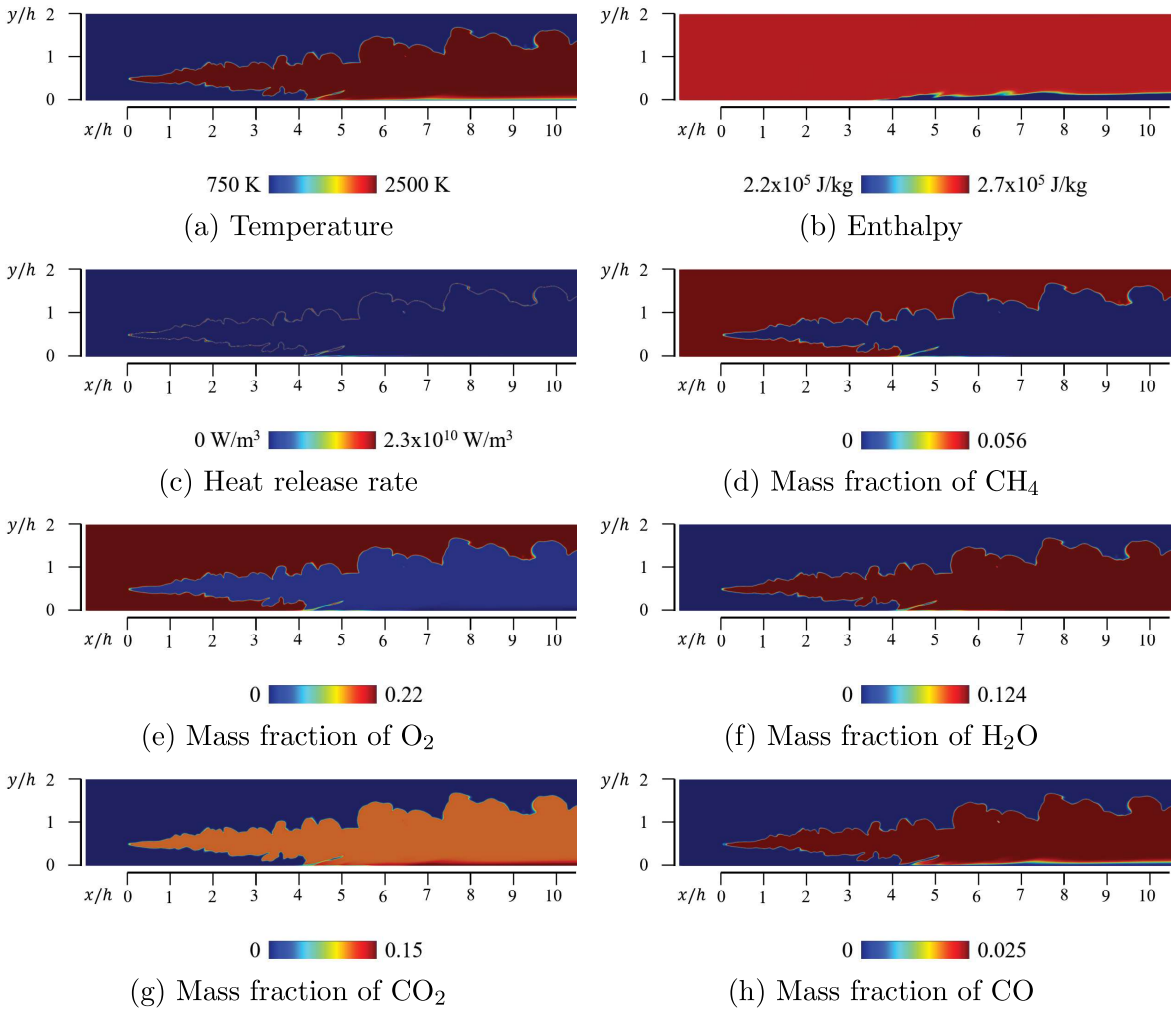

(a) Temperature (b) Enthalpy

(c) Heat release rate (d) Mass fraction of CH_4

(e) Mass fraction of O_2 (f) Mass fraction of H_2O

(g) Mass fraction of CO_2 (h) Mass fraction of CO

Figure 3.6: Instantaneous distributions of (a) temperature, (b) enthalpy, (c) heat release rate, and (d)-(h) mass fractions of CH_4, O_2, H_2O, CO_2, and CO on x-y plane at $z/h = 0$ at $t = 4.45$ ms.

propagation toward the wall, and the ejection raises unburnt gas away from the wall, as observed in previous studies [2, 18]. Figure 3.9 shows the instantaneous distributions of c and $Q^* > 1 \times 10^8$ 1/s^2 on x-y plane at $z/h = 0.27$. The streamwise vortex exists in the protruded unburnt gas at approximately $x/h = 3.6$. This vortex corresponds to the left vortex enclosed by the magenta circle in Fig.3.8(c). On the right side of this vortex, the upward burnt gas is advected downward, and on the left side of this vortex, the downward burnt gas, which is diffused form upstream direction, can be found. Thus, unburnt gas pockets are formed in the downstream region.

3.4.2 SDF behavior

Figure 3.10 shows instantaneous distributions of the SDF on x-y plane at $z/h = 0$ and on x-z plane at $y^+ = 4$ at $t = 4.45$ ms. To demonstrate near-wall behavior, Fig.3.11 shows the enlarged view of Fig.3.10 with isoline of $c = 0.5$. These figures clearly show that the SDF assumes peak values close to $c = 0.5$ away from the wall. However, in the vicinity of the wall, the SDF remains small even close to $c = 0.5$. Figure 3.12 shows the instantaneous distributions of c, heat release rate, enthalpy deficit ΔH, normalized values of a_n^{eff}, a_n, and $\boldsymbol{n} \cdot \nabla S_d$ for normalized SDF $|\nabla c| \times \delta_{th} > 0.001$ at $z/h = 0$. Here, ΔH is defined as $\Delta H = H_{ad} - H$ where H_{ad} is the adiabatic specific enthalpy. Figure 3.13 shows the instantaneous distributions of same variables shown in Fig.3.12 on x-z plane at $y^+ = 4$. Away from the wall, a_n assumes positive peak values near the isoline of $c = 0.5$ because of the dominance of the thermal expansion effects. By contrast, negative peak values of $\boldsymbol{n} \cdot \nabla S_d$ are obtained close to $c = 0.5$ because the displacement speed S_d increases from the unburned to the burned gas side of the flame due to the density variation as a result of thermal expansion. The relative magnitudes of a_n and $\boldsymbol{n} \cdot \nabla S_d$ lead to the behavior of a_n^{eff} and this results in large positive values of a_n^{eff} in burnt gas side and unburnt gas side of the folded flame. In the vicinity of the wall, despite being near the isoline of $c = 0.5$, the SDF has small values if the enthalpy deficit is large and heat release rate effects are weak, as shown in Figs.3.11(b) and 3.13. In addition to the heat loss, the flame structure also affects the magnitude of SDF. At approximately

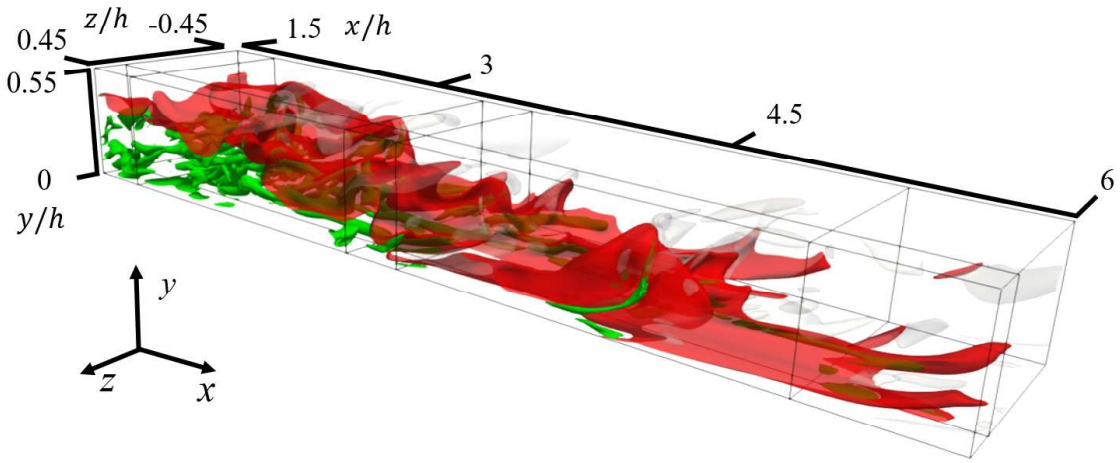

(a) $t = 4.30\,\mathrm{ms}$

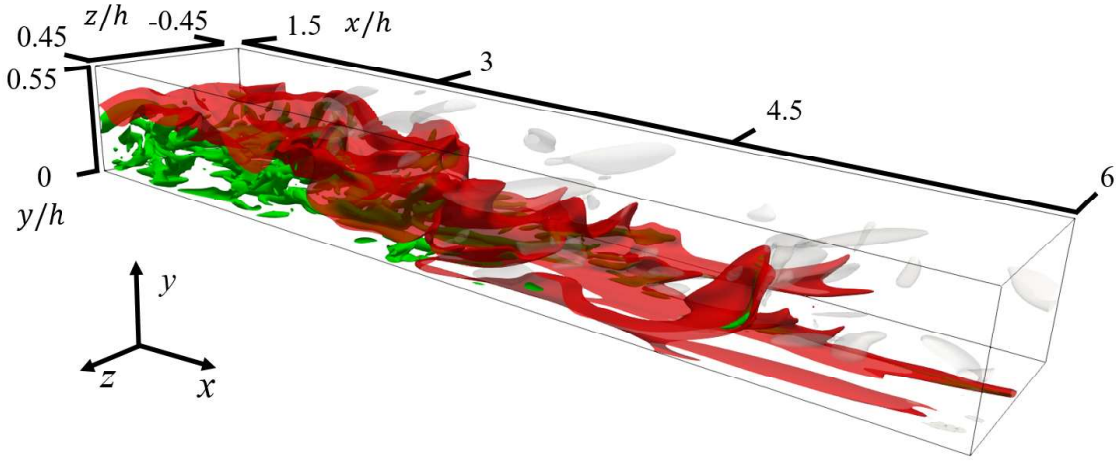

(b) $t = 4.35\,\mathrm{ms}$

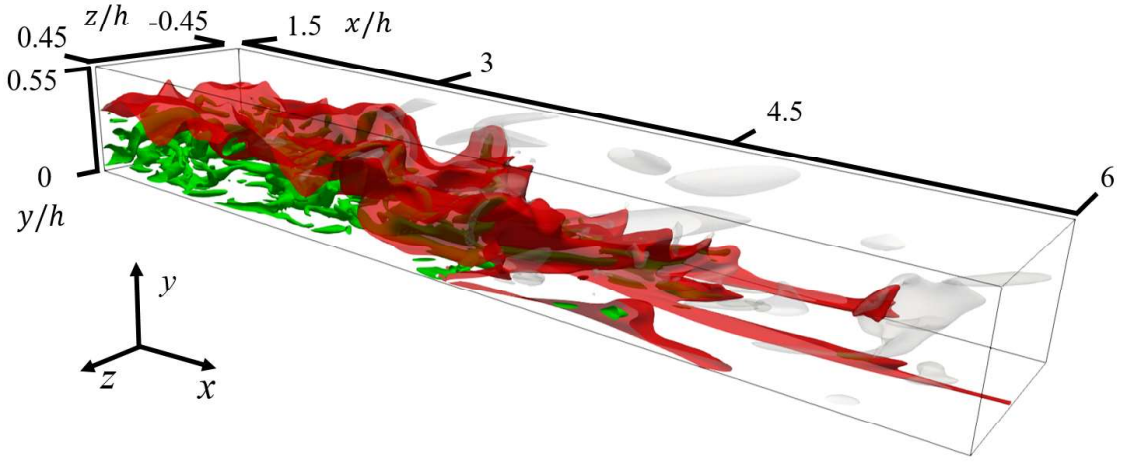

(c) $t = 4.40\,\mathrm{ms}$

Figure 3.7: Time series of instantaneous isofurfaces of progress variable ($c = 0.5$, colored in red) and second invariant of velocity gradient tensor ($Q^* = 1 \times 10^8\ 1/\mathrm{s}^2$, colored in green for $c < 0.5$, colored in white for $c > 0.5$) near bottom wall .

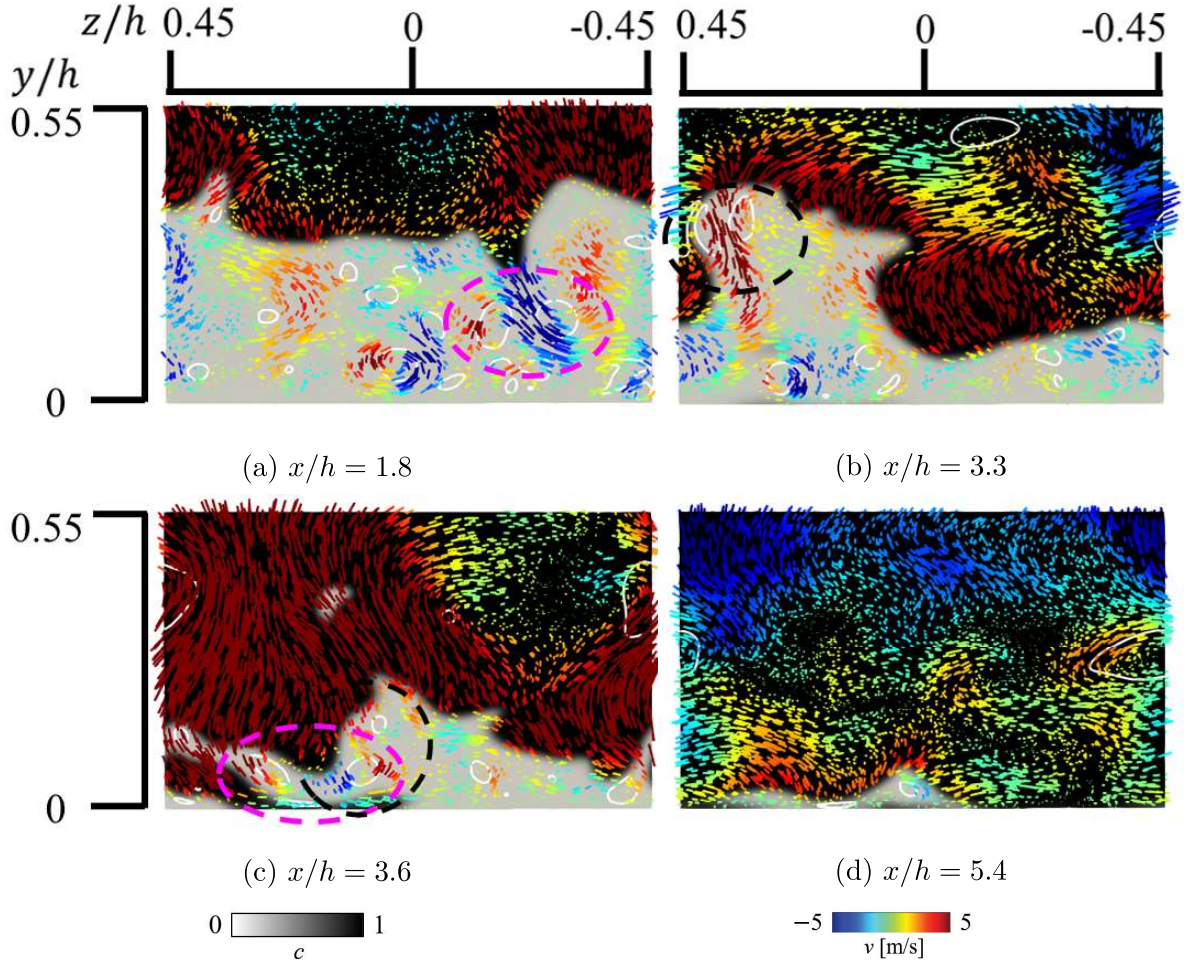

Figure 3.8: Instantaneous distributions of progress variable c, isolines of second invariant of velocity gradient tensor ($Q^* = 1 \times 10^8$ 1/s^2, colored in white), and velocity vectors on y-z plane colored by y-component of velocity vector v at $x/h =$ (a) 1.8, (b) 3.3, (c) 3.6, and (d) 5.4 at $t = 4.3$ ms. Locations of each cross-section are shown in Fig.3.7(a). Magenta and black circles show sweep and ejection flows .

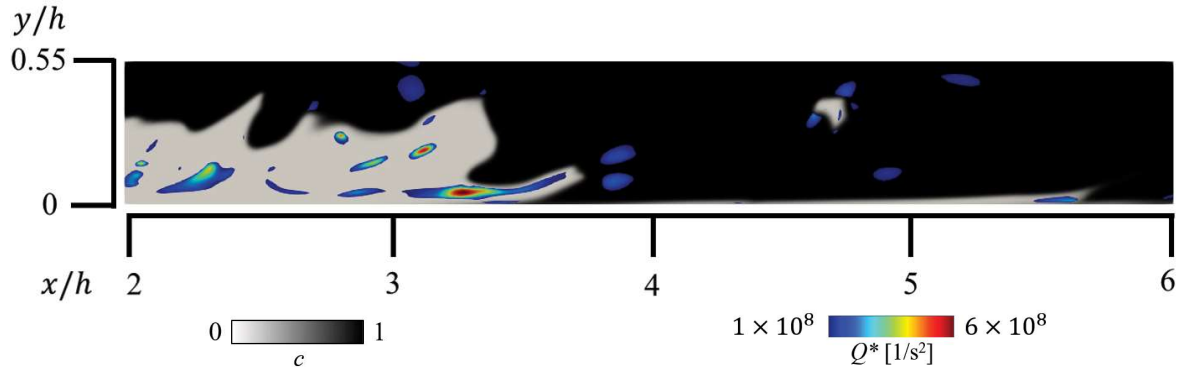

Figure 3.9: Instantaneous distributions of progress variable c ans second invariant of velocity gradient tensor (for $Q^* > 1 \times 10^8$ 1/s^2) on x-y plane at $z/h = 0.27$ at $t = 4.3$ ms

.

$5 < x/h < 5.5$ and $-0.45 < z/h < -0.3$, for example, the SDF becomes smaller than that in the area where the c and enthalpy deficit have same magnitudes, because the upstream and downstream flame surfaces of the folded flame merge resulting in the formation of saddle point of c. For the a_n distribution, different from the behavior away from the wall, a_n tends to have negative values downstream of the isoline of $c = 0.5$ and positive peak values outside of the negative a_n region. As shown in Fig.3.7, the unbunt gas protrudes forward and upward near the wall. As the heat release rate of upper side of the protruded unburnt gas is larger than that of the lower side because of the lower heat loss, the stronger thermal expansion of the upper side generates the flow toward the wall. This flow and zero velocity on the wall surface result in the negative a_n in the downstream side of the isoline of $c = 0.5$, which corresponds to the flame surface of lower side of the protruded unburnt gas. The impinged flow on the wall changes its flow direction to parallel to the wall; thus, the a_n becomes positive outside of the negative a_n region. The $\boldsymbol{n} \cdot \nabla S_d$ is generally positive. It is negative if the hear release rate is large. For the a_n^{eff}, the negative value of a_n downstream the isoline of $c = 0.5$ results in the negative a_n^{eff} in the same area. For the positive value of a_n^{eff}, the contribution of $\boldsymbol{n} \cdot \nabla S_d$ is dominant, except for the low heat loss region.

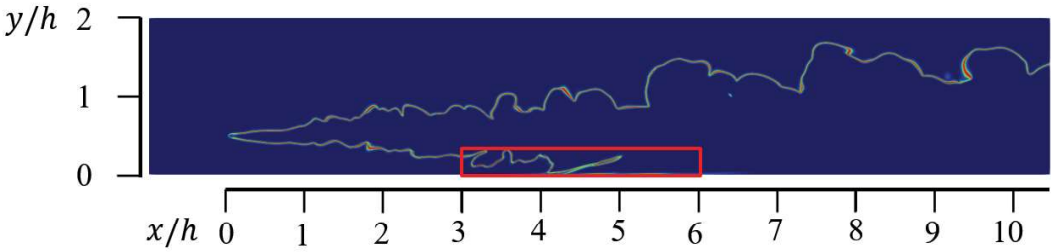

(a) x-y plane

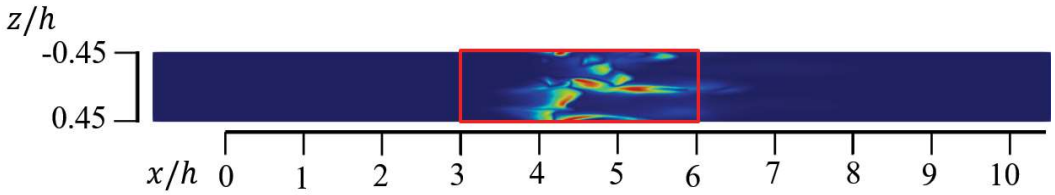

(b) x-z plane

Figure 3.10: Instantaneous distributions of normalized surface density function $|\nabla c| \times \delta_{th}$ on (a) x-y plane at $z/h = 0$, and (b) on x-z plane at $y^+ = 4$ at $t = 4.45\,\mathrm{ms}$.

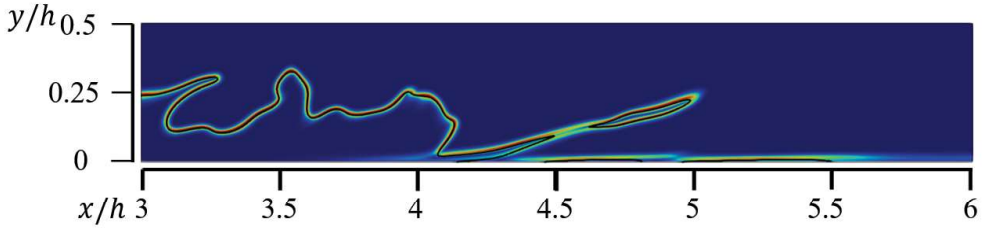

(a) x-y plane

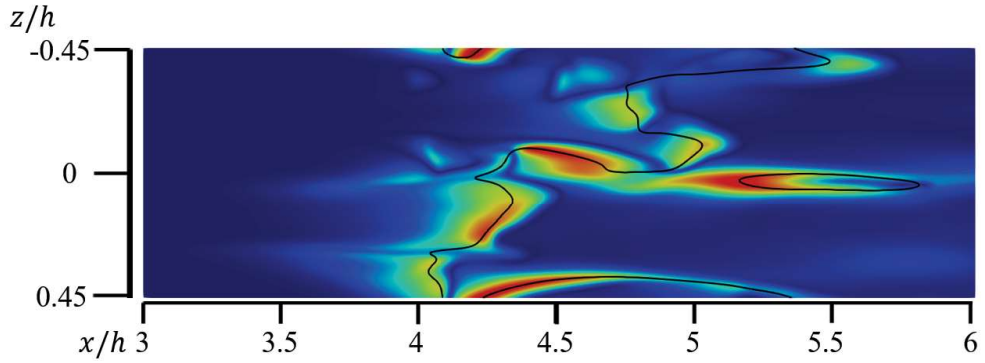

(b) x-z plane

Figure 3.11: Close-up views of areas enclosed by red rectangular in Fig.3.10. Black line represents isoline of progress variable $c = 0.5$.

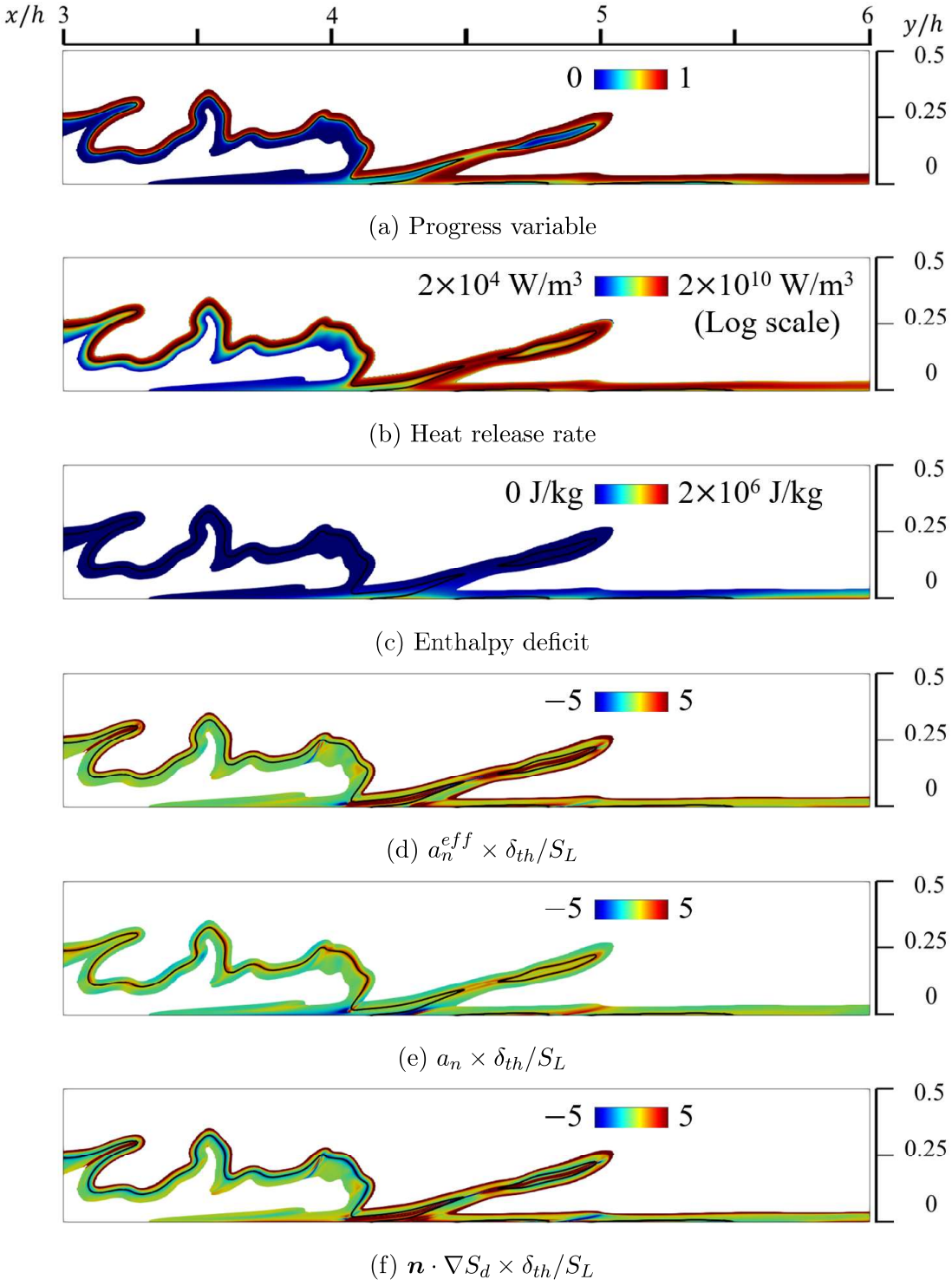

(a) Progress variable

(b) Heat release rate

(c) Enthalpy deficit

(d) $a_n^{eff} \times \delta_{th}/S_L$

(e) $a_n \times \delta_{th}/S_L$

(f) $\boldsymbol{n} \cdot \nabla S_d \times \delta_{th}/S_L$

Figure 3.12: Instantaneous distributions of (a) progress variable c, (b) heat release rate, (c) enthalpy deficit, normalized values of (d) a_n^{eff}, (e) a_n, and (f) $\boldsymbol{n} \cdot \nabla S_d$ on x-y plane at $z/h = 0$ near-wall for $|\nabla c| \times \delta_{th} > 0.001$ at $t = 4.45\,\mathrm{ms}$. Black line represents isoline of progress variable $c = 0.5$.

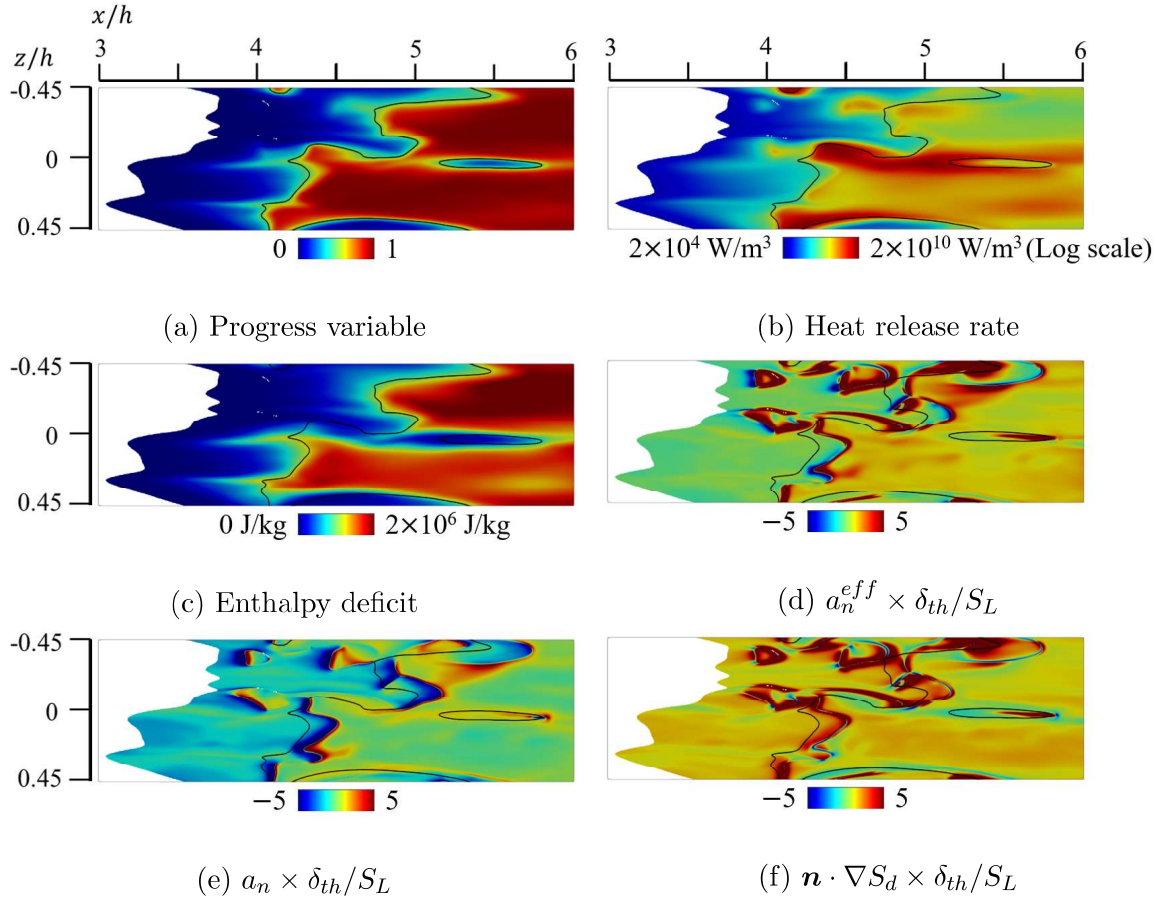

(a) Progress variable

(b) Heat release rate

(c) Enthalpy deficit

(d) $a_n^{eff} \times \delta_{th}/S_L$

(e) $a_n \times \delta_{th}/S_L$

(f) $\boldsymbol{n} \cdot \nabla S_d \times \delta_{th}/S_L$

Figure 3.13: Instantaneous distributions of (a) progress variable c, (b) heat release rate, (c) enthalpy deficit, normalized values of (d) a_n^{eff}, (e) a_n, and (f) $\boldsymbol{n} \cdot S_d$ on x-z plane at $y^+ = 4$ for $|\nabla c| \times \delta_{th} > 0.001$ at $t = 4.45\,\mathrm{ms}$. Black line represents isoline of progress variable $c = 0.5$.

For the FSD and SDR based modeling, the statistical behavior of SDF is investigated. Figure 3.14 shows the mean values of normalized SDF $|\nabla c| \times \delta_{th}$ and enthalpy conditioned on c. The mean values in the viscous sublayer (at $y^+ = 0.6$), buffer layer (at $y^+ = 20$), and outer layer (at $y^+ = 71$) are compared to investigate the effect of the isothermal wall. Moreover, the mean values are calculated for different streamwise locations. For comparison, the SDF profile for one-dimensional laminar planar flame is also shown in Fig.3.14. The mean value of SDF in the outer layer (at $y^+ = 71$) matches with that of one-dimensional laminar planar flame, whereas the mean values of SDF in the buffer layer (at $y^+ = 20$) and viscous sublayer (at $y^+ = 0.6$) are almost 90% and 10% of that of the planar flame, respectively. In all three layers, the local mean value of SDF has been found to decrease in the downstream direction. For the enthalpy, the heat loss is negligible at $y^+ = 71$, and the enthalpy decreases as c increase at $y^+ = 0.6$ and 20. The comparison of mean SDF and mean enthalpy implies that the mitigation of the reaction due to the heat loss decreases the mean SDF.

The evolution of the SDF is also investigated. Figure 3.15 shows the mean values of a_n^{eff}, a_n, and $\boldsymbol{n} \cdot \nabla S_d$ conditioned on c at different wall-normal distances for different stream wise locations. The mean value of effective normal strain rate a_n^{eff}, whose increase tends to decrease the value of SDF, is significantly higher at $y^+ = 0.6$ than those at $y^+ = 71$ and 21. This means that the SDF steeply decreases in the viscous sublayer. In the viscous sublayer, the contribution of $\boldsymbol{n} \cdot \nabla S_d$ to the a_n^{eff} is more dominant than that of normal strain rate a_n. This tendency is qualitatively similar to the analysis of the previous study for $Re_\tau = 110$ [39], however the maximum value of a_n^{eff} for $Re_\tau = 395$ is approximately twice that for $Re_\tau = 110$, which causes the marked decrease in the SDF in the viscous sublayer at a higher Re_τ. In all three layers, the local mean values of a_n^{eff} and $\boldsymbol{n} \cdot \nabla S_d$ decreases downstream.

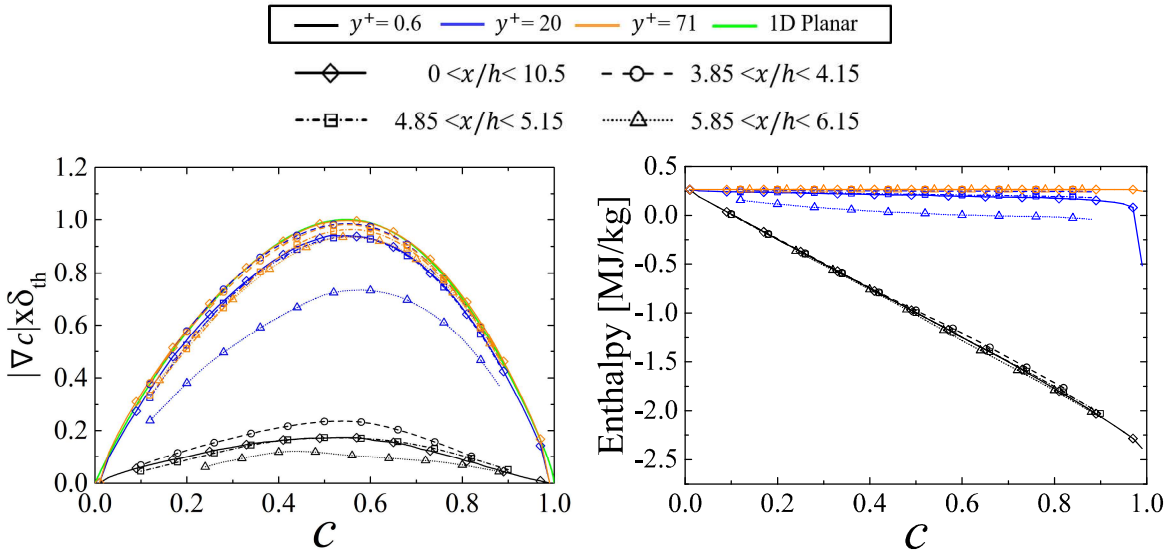

(a) Surface density function (b) Enthalpy

Figure 3.14: Mean values of (a) normalized surface density function $|\nabla c| \times \delta_{th}$, and (b) enthalpy plotted versus progress variable c at different wall normal distances of $y^+ = 0.6$, 20, 71 for different streamwise locations. .

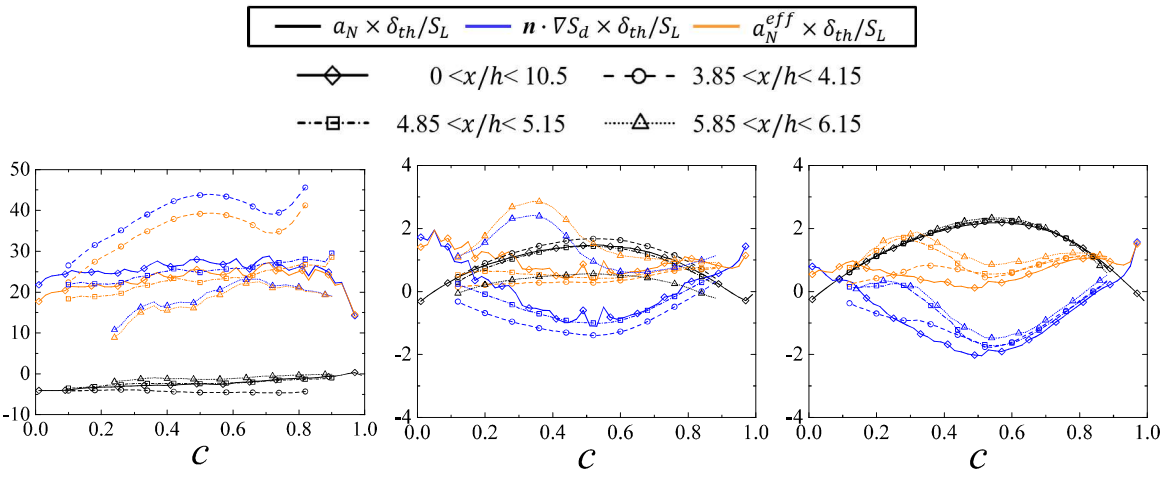

(a) $y^+ = 0.6$ (b) $y^+ = 20$ (c) $y^+ = 71$

Figure 3.15: Mean values of normalized normal strain rate a_n, gradient of displacement speed in flame-normal direction $\boldsymbol{n} \cdot \nabla S_d$, and effective normal strain rate a_n^{eff} plotted versus progress variable c at (a) $y^+ = 0.6$, (b) $y^+ = 20$, and (c) $y^+ = 71$ for different streamwise locations. .

3.5 Conclusions

In this study, a three-dimensional DNS of turbulent premixed V-flame interacting with an isothermal wall in the wall-bounded turbulent channel flow at friction Reynolds number $Re_\tau = 395$ for stoichiometric methane-air flame was performed employing a two-step global reaction mechanism [44]. The flame-turbulence interaction and statistical behavior of surface density function (SDF) in the vicinity of the wall were investigated. The main results obtained in this study can be summarized as follows.

1. It has been found that the streamwise vortices strongly affects the flame behavior near the wall. By contrast, sweep enhances flame propagation toward the wall, and the ejection raises unburnt gas away from the wall. Some of the unburnt gas raised by the ejection give rise to the unburnt gas pockets in the downstream region.

2. The statistical behaviors of SDF, effective normal strain rate a_n^{eff}, normal strain rate a_n, and gradient of displacement speed in flame-normal direction $\boldsymbol{n} \cdot \nabla S_d$ are investigated in progress variable c space at different wall-normal distances and streamwise locations. The mean value of SDF in the outer layer (at $y^+ = 71$) in progress variable space matches with that of one-dimensional laminar planar flame, whereas the mean values of SDF in the buffer layer (at $y^+ = 20$) and viscous sublayer (at $y^+ = 0.6$) are almost 90% and 10% of that of the planar flame, respectively. In all three layers, the local mean value of SDF has been found to decrease in the downstream direction. These suggests that the mean value of SDF is strongly affected by the heat loss through the wall.

3. The mean value of effective normal strain rate a_n^{eff} $(= \boldsymbol{n} \cdot \nabla S_d + a_n)$, whose increase tends to decrease the value of SDF, is much higher at $y^+ = 0.6$ than those at $y^+ = 71$ and 21. This means that the SDF steeply decreases in the viscous sublayer. In the viscous sublayer, the contribution of $\boldsymbol{n} \cdot \nabla S_d$ to the a_n^{eff} is more dominant than that of normal strain rate a_n. This tendency is qualitatively similar to the analysis of the previous study for $Re_\tau = 110$ [39], however the maximum

value of a_n^{eff} for $Re_\tau = 395$ is approximately twice that for $Re_\tau = 110$, which causes the marked decrease in the SDF in the viscous sublayer at a higher Re_τ. In all three layers, the local mean values of a_n^{eff} and $\boldsymbol{n} \cdot \nabla S_d$ decreases downstream.

4. At $Re_\tau = 395$, the statistical values related to the SDF evolution are quantitatively different from those at $Re_\tau = 110$, although the tendency that the drop of the SDF in the viscous sublayer mainly because of strain rate induced by displacement speed rather than aerodynamic strain is qualitatively the same.

References

[1] T. Poinsot and D. Veynante. Theoretical and numerical combustion, 2005.

[2] T. M. Alshaalan and C. J. Rutland. Turbulence, scalar transport, and reaction rates in flame-wall interaction. In *Symposium (International) on Combustion*, volume 27, 793–799. Elsevier, 1998.

[3] G. Bruneaux, T. Poinsot, and J. Ferziger. Premixed flame–wall interaction in a turbulent channel flow: budget for the flame surface density evolution equation and modelling. *Journal of Fluid Mechanics*, 349:191–219, 1997.

[4] J. Lai and N. Chakraborty. Effects of lewis number on head on quenching of turbulent premixed flames: a direct numerical simulation analysis. *Flow, Turbulence and Combustion*, 96(2):279–308, 2016.

[5] J. Sellmann, J. Lai, A. M. Kempf, and N. Chakraborty. Flame surface density based modelling of head-on quenching of turbulent premixed flames. *Proceedings of the Combustion Institute*, 36(2):1817–1825, 2017.

[6] J. Lai and N. Chakraborty. A priori direct numerical simulation modeling of scalar dissipation rate transport in head-on quenching of turbulent premixed flames. *Combustion Science and Technology*, 188(9):1440–1471, 2016.

[7] M. Mann, C. Jainski, M. Euler, B. Böhm, and A. Dreizler. Transient flame–wall interactions: Experimental analysis using spectroscopic temperature and co concentration measurements. *Combustion and Flame*, 161(9):2371–2386, 2014.

[8] C. Jainski, M. Rißmann, B. Böhm, and A. Dreizler. Experimental investigation of flame surface density and mean reaction rate during flame–wall interaction. *Proceedings of the Combustion Institute*, 36(2):1827–1834, 2017.

[9] J. Lai, M. Klein, and N. Chakraborty. Direct numerical simulation of head-on quenching of statistically planar turbulent premixed methane-air flames using a

detailed chemical mechanism. *Flow, turbulence and combustion*, 101(4):1073–1091, 2018.

[10] U. Ahmed, N. Chakraborty, and M. Klein. Assessment of bray moss libby formulation for premixed flame-wall interaction within turbulent boundary layers: Influence of flow configuration. *Combustion and Flame*, 233:111575, 2021.

[11] C. Eichler, G. Baumgartner, and T. Sattelmayer. Experimental investigation of turbulent boundary layer flashback limits for premixed hydrogen-air flames confined in ducts. *Journal of Engineering for Gas Turbines and Power*, 134(1), 2012.

[12] M. Rißmann, C. Jainski, M. Mann, and A. Dreizler. Flame-flow interaction in premixed turbulent flames during transient head-on quenching. *Flow, Turbulence and Combustion*, 98(4):1025–1038, 2017.

[13] C. Jainski, M. Rißmann, B. Böhm, J. Janicka, and A. Dreizler. Sidewall quenching of atmospheric laminar premixed flames studied by laser-based diagnostics. *Combustion and Flame*, 183:271–282, 2017.

[14] H. Kosaka, F. Zentgraf, A. Scholtissek, C. Hasse, and A. Dreizler. Effect of flame-wall interaction on local heat release of methane and dme combustion in a side-wall quenching geometry. *Flow, Turbulence and Combustion*, 104(4):1029–1046, 2020.

[15] F. Zentgraf, P. Johe, A. D. Cutler, R. S. Barlow, B. Böhm, and A. Dreizler. Classification of flame prehistory and quenching topology in a side-wall quenching burner at low-intensity turbulence by correlating transport effects with CO_2, CO and temperature. *Combustion and Flame*, 111681, 2021.

[16] A. Goldmann and F. Dinkelacker. Experimental investigation and modeling of boundary layer flashback for non-swirling premixed hydrogen/ammonia/air flames. *Combustion and Flame*, 226:362–379, 2021.

[17] T. Poinsot, D. C. Haworth, and G. Bruneaux. Direct simulation and modeling of flame-wall interaction for premixed turbulent combustion. *Combustion and Flame*, 95(1-2):118–132, 1993.

[18] G. Bruneaux, K. Akselvoll, T. Poinsot, and J. Ferziger. Flame-wall interaction simulation in a turbulent channel flow. *Combustion and flame*, 107(1-2):27–44, 1996.

[19] T. Alshaalan and C. J. Rutland. Wall heat flux in turbulent premixed reacting flow. *Combustion science and technology*, 174(1):135–165, 2002.

[20] F. Dabireau, B. Cuenot, O. Vermorel, and T. Poinsot. Interaction of flames of H_2+ O_2 with inert walls. *Combustion and flame*, 135(1-2):123–133, 2003.

[21] A. Gruber, R. Sankaran, E. Hawkes, and J. Chen. Turbulent flame–wall interaction: a direct numerical simulation study. *Journal of Fluid Mechanics*, 658:5–32, 2010.

[22] A. Gruber, J. H. Chen, D. Valiev, and C. K. Law. Direct numerical simulation of premixed flame boundary layer flashback in turbulent channel flow. *Journal of Fluid Mechanics*, 709:516–542, 2012.

[23] T. Kitano, T. Tsuji, R. Kurose, and S. Komori. Effect of pressure oscillations on flashback characteristics in a turbulent channel flow. *Energy & Fuels*, 29(10):6815–6822, 2015.

[24] J. Lai, N. Chakraborty, and A. Lipatnikov. Statistical behaviour of vorticity and enstrophy transport in head-on quenching of turbulent premixed flames. *European Journal of Mechanics-B/Fluids*, 65:384–397, 2017.

[25] J. Lai, D. H. Wacks, and N. Chakraborty. Flow topology distribution in head-on quenching of turbulent premixed flame: a direct numerical simulation analysis. *Fuel*, 224:186–209, 2018.

[26] U. Ahmed, N. A. K. Doan, J. Lai, M. Klein, N. Chakraborty, and N. Swaminathan. Multiscale analysis of head-on quenching premixed turbulent flames. *Physics of Fluids*, 30(10):105102, 2018.

[27] P. Zhao, L. Wang, and N. Chakraborty. Strain rate and flame orientation statistics in the near-wall region for turbulent flame-wall interaction. *Combustion Theory and Modelling*, 22(5):921–938, 2018.

[28] P. Zhao, L. Wang, and N. Chakraborty. Analysis of the flame–wall interaction in premixed turbulent combustion. *Journal of Fluid Mechanics*, 848:193–218, 2018.

[29] A. Gruber, E. S. Richardson, K. Aditya, and J. H. Chen. Direct numerical simulations of premixed and stratified flame propagation in turbulent channel flow. *Physical Review Fluids*, 3(11):110507, 2018.

[30] P. Zhao, L. Wang, and N. Chakraborty. Vectorial structure of the near-wall premixed flame. *Physical Review Fluids*, 4(6):063203, 2019.

[31] U. Ahmed, A. L. Pillai, N. Chakraborty, and R. Kurose. Statistical behavior of turbulent kinetic energy transport in boundary layer flashback of hydrogen-rich premixed combustion. *Physical Review Fluids*, 4(10):103201, 2019.

[32] B. Jiang, R. L. Gordon, and M. Talei. Head-on quenching of laminar premixed methane flames diluted with hot combustion products. *Proceedings of the Combustion Institute*, 37(4):5095–5103, 2019.

[33] R. Palulli, M. Talei, and R. L. Gordon. Unsteady flame–wall interaction: Impact on co emission and wall heat flux. *Combustion and Flame*, 207:406–416, 2019.

[34] U. Ahmed, A. L. Pillai, N. Chakraborty, and R. Kurose. Surface density function evolution and the influence of strain rates during turbulent boundary layer flashback of hydrogen-rich premixed combustion. *Physics of Fluids*, 32(5):055112, 2020.

[35] R. Kai, R. Masuda, T. Ikedo, and R. Kurose. Conjugate heat transfer analysis of methane/air premixed flame–wall interaction: A study on effect of wall material. *Applied Thermal Engineering*, 181:115947, 2020.

[36] P. Zhao, L. Wang, and N. Chakraborty. Effects of the cold wall boundary on the flame structure and flame speed in premixed turbulent combustion. *Proceedings of the Combustion Institute*, 38(2):2967–2976, 2021.

[37] I. Konstantinou, U. Ahmed, and N. Chakraborty. Effects of fuel lewis number on the near-wall dynamics for statistically planar turbulent premixed flames impinging on inert cold walls. *Combustion Science and Technology*, 193(2):235–265, 2021.

[38] K. Yunoki, R. Kai, S. Inoue, and R. Kurose. Numerical simulation of co formation and reduction on flame propagation due to heat loss through the cooled wall. *Energy*, 236:121352, 2021.

[39] U. Ahmed, N. Chakraborty, and M. Klein. Scalar gradient and strain rate statistics in oblique premixed flame–wall interaction within turbulent channel flows. *Flow, Turbulence and Combustion*, 106(2):701–732, 2021.

[40] B. Jiang, D. Brouzet, M. Talei, R. L. Gordon, Q. Cazeres, and B. Cuenot. Turbulent flame-wall interactions for flames diluted by hot combustion products. *Combustion and Flame*, 230:111432, 2021.

[41] W. Kollmann and J. H. Chen. Pocket formation and the flame surface density equation. In *Symposium (International) on Combustion*, volume 27, 927–934. Elsevier, 1998.

[42] M. Boger, D. Veynante, H. Boughanem, and A. Trouvé. Direct numerical simulation analysis of flame surface density concept for large eddy simulation of turbulent premixed combustion. In *Symposium (International) on Combustion*, volume 27, 917–925. Elsevier, 1998.

[43] R. Borghi and D. Dutoya. On the scales of the fluctuations in turbulent combustion. In *Symposium (International) on Combustion*, volume 17, 235–244. Elsevier, 1979.

[44] B. Franzelli, E. Riber, M. Sanjosé, and T. Poinsot. A two-step chemical scheme for kerosene–air premixed flames. *Combustion and Flame*, 157(7):1364–1373, 2010.

[45] B. Franzelli, E. Riber, L. Y. Gicquel, and T. Poinsot. Large eddy simulation of combustion instabilities in a lean partially premixed swirled flame. *Combustion and Flame*, 159(2):621–637, 2012.

[46] R. D. Moser, J. Kim, and N. N. Mansour. Direct numerical simulation of turbulent channel flow up to re τ= 590. *Physics of fluids*, 11(4):943–945, 1999.

[47] R. Kurose. FK^3, `http://www.tse.me.kyoto-u.ac.jp/members/kurose/link_e.php`, 2020.

[48] V. Moureau, C. Bérat, and H. Pitsch. An efficient semi-implicit compressible solver for large-eddy simulations. *Journal of Computational Physics*, 226(2):1256–1270, 2007.

[49] V. Titarev and E. Toro. WENO schemes based on upwind and centred TVD fluxes. *Computers & Fluids*, 34(6):705–720, 2005.

[50] S. Gottlieb and C. W. Shu. Total variation diminishing Runge-Kutta schemes. *Mathematics of computation of the American Mathematical Society*, 67(221):73–85, 1998.

[51] T. Echekki and J. H. Chen. Unsteady strain rate and curvature effects in turbulent premixed methane-air flames. *Combustion and Flame*, 106(1-2):184–202, 1996.

[52] N. Chakraborty, M. Klein, D. Alwazzan, and H. G. Im. Surface density function statistics in hydrogen-air flames for different turbulent premixed combustion regimes. *Combustion Science and Technology*, 190(11):1988–2002, 2018.

[53] H. Abe, H. Kawamura, and Y. Matsuo. Direct numerical simulation of a fully developed turbulent channel flow with respect to the reynolds number dependence. *Journal of fluids Engineering*, 123(2):382–393, 2001.

Nomenclature

a_n : Normal strain rate [1/s]

a_n^{eff} : Effective normal strain rate [1/s]

c : Progress variable [-]

c_p : Specific heat capacity [J/(K kg)]

D : Diffusion coefficient [m^2/s]

H : Specific enthalpy [J/kg]

h : Channel half height [m]

N_c : Scalar dissipation rate [1/s]

$\boldsymbol{n}$: Flame normal vector [-]

Pe_Q : Quenching Peclet number [-]

p : Pressure [Pa]

Q^* : Invariant of velocity gradient tensor [$1/s^2$]

Re_τ : Friction Reynolds number [-]

S : Strain rate tensor [1/s]

S_d : Displacement speed [m/s]

S_L : Laminar burning velocity [m/s]

T : Temperature [K]

T^* : Non-dimensional temperature [-]

t : Time [s]

$\boldsymbol{u}$: Velocity [m/s]

u_τ : Friction velocity [m/s]

Y : Mass fraction [-]

α : Thermal diffusivity [m^2/s]

δ_Q : Quenching distance [m]

δ_{th} : Flame thickness [m]

δ_Z : Zel'dovich flame thickness [m]

ν : Kinematic viscosity [m^2/s]

λ : Thermal conductivity [W/(m K)]

ρ : Density [kg/m^3]

Σ_{gen} : Generalized flame surface density [1/m]

$\boldsymbol{\tau}$: Viscous stress tensor [$kg/(m^2\ s^2)$]

ϕ : Equivalence ratio [-]

Ω : Vorticity tensor [1/s]

$\dot{\omega}$: Reaction rate [1/s]

Subscripts

ad : Adiabatic flame

$Bulk$: Bulk value

b : Burnt gas

H : Enthalpy

L : Laminar planar flame

max : Maximum value

min : Minimum value

u : Unburnt gas

w : Wall

Superscript

$+$: Wall unit

Chapter 4

Conjugate heat transfer analysis of spray flame-wall interaction in jet impinging on wall

4.1 Introduction

In this chapter, heat transfer between spray flame and wall is investigated using DNS.

According to the United Nations Environment Programme (UNEP) annual emissions gap report [1], global greenhouse gas emissions should be cut drastically in the next decade to limit the adverse consequences of climate change. Therefore, to mitigate the challenges of climate change, it is necessary to suppress the anthropogenic CO_2 emissions, most of which arise from the burning of fossil fuels. In this regard, many governments across the globe are expected to set ambitious new commitments to slash their CO_2 emissions, as part of the 2015 Paris Agreement [2] at the 21^{st} Conference of the Parties (COP21) to the United Nations Framework Convention on Climate Change (UNFCC). However, all energy outlooks [3, 4] acknowledge that combustion will play an indispensable role in the energy sector for the foreseeable future. The road transportation sector which is vital for any economy, currently accounts for approximately 16 % of the global CO_2 emissions [5]. Under these circumstances, further improvements in the

thermal efficiencies of Compression Ignition (CI) engines (which are a type of widely-used Internal Combustion engine) are urgently needed. One way to achieve this, is to reduce the heat loss through the engine cylinder/combustion chamber wall, which accounts for nearly 30 % of the fuel energy released in the form of combustion [6]. Consequently, good understanding of the wall heat loss mechanism under different combustion conditions such as engine size, fuel injection rate, etc., is paramount for developing fuel-efficient CI engines. If the heat loss through the combustion chamber wall could be accurately predicted in the early design stages, then the optimal combustion conditions for reducing heat loss can be devised, thereby achieving significant savings in the engine design cycle time. Normally, heat loss through the wall in Internal Combustion (IC) engines is estimated based on the principle of convective heat transfer, where the dimensionless average Nusselt number Nu (corresponding to the average heat flux at the wall surface assuming quasi-steady state conditions) is a function of two other dimensionless parameters, viz. the Reynolds number Re and the Prandtl number Pr. In this regard, since the 20th century, many researchers have performed IC engine experiments, using both Spark Ignition (SI) and CI engines [7–12], and proposed empirical equations/correlations (derived from their experimental data) of the form:

$$Nu \propto Re^{n} \tag{4.1}$$

under the assumption that the Prandtl number Pr is constant. In Eq. (4.1), n is the correlation index. Once such a correlation for Nu is known, it is possible to directly calculate the value of Nu, and then using this knowledge of Nu, the average convective heat transfer coefficient h_{heat} can be estimated. The average wall heat flux q_w can then be computed easily from Newton's law of cooling, which is expressed as:

$$q_w = h_{heat}(T - T_w) \tag{4.2}$$

where T is the representative gas-phase temperature and T_w is the wall temperature. To this extent, Woschni [10] applied the analogy of non-reacting fully-developed turbulent flow in pipes (i.e., forced convection assumption) to the flow in engines, and reported a correlation between Nu and Re of the form $Nu \propto Re^{0.8}$, similar to Eq. (4.1). Therefore,

Woschni determined the value of the correlation index n in Eq. (4.1) to be 0.8. However, the applicability of Woschni's correlation during the combustion period inside an IC engine has not been verified, even though it is still being used for zero-dimensional cycle simulations (e.g., [13, 14]). In the same manner, other researchers have also proposed values for the correlation index n in Eq. (4.1) based on their experiments (using forced convection assumption), such as Oguri ($n = 0.5$) [8], Annand ($n = 0.7$) [9], Sitkei and Ramanaiah ($n = 0.7$) [11], and Hohenberg [12] ($n = 0.8$). Recently, Inagaki et al. [15] investigated the effects of bore size and fuel injection conditions on the heat loss through combustion chamber wall, experimentally and theoretically from the viewpoint of fuel efficiency. Follow-up experiment performed by Inagaki et al. [16] aimed to propose a correlation for the heat transfer coefficient, by applying the similarity of spray characteristics to diesel spray combustion, and tried to elucidate the dependence of heat loss through the wall (during spray flame-wall interaction process) on the representative velocity. From their experiments [15, 16], a power law dependence of Nu on Re of the form $Nu \propto Re^{0.4}$ was deduced, indicating the value of the correlation index to be $n = 0.4$. However, in a more recent experimental study conducted by Mahmud et al. [17], a correlation index value of $n = 0.8$ was found (i.e., $Nu \propto Re^{0.8}$). Hence, it is evident from all the above-mentioned experimental investigations that, there is an appreciable variation in the value of the correlation index n, indicating the lack of a clear consensus on the relation between Nu and Re corresponding to wall heat loss during spray flame-wall interaction process.

Although measurement errors might occur while performing experiments, the variations in the value of correlation index n proposed in the aforementioned studies [8–12, 15–17], could also arise due to the way in which Nu and Re are defined in the respective studies. This is owing to the physical constraints and restrictions of a given experimental setup, which could make it very challenging to take into account the detailed spatial distributions and temporal evolution of flame temperature, spray flame-wall contact area, gas-phase velocity and wall heat flux, while performing measurements. Another reason could be the fact that, when wall heat flux is measured in an experiment, it might implic-

itly include the contribution of radiative heat transfer. Under CI engine-like conditions, the contribution of radiative heat transfer from spray flame to the wall heat flux could be non-negligible, and can account for 5% to 15% of the total wall heat flux as reported by Yan and Borman [18]. So, when such heat flux measurements are used to calculate the Nusselt number Nu (a parameter fundamentally defined in the context of convective heat transfer alone), significant variations in the value of n could occur.

For these reasons, numerical simulations can prove to be effective tools for elucidating such complex two-phase reacting flow problems. Considerable progress has been made on numerical simulation and modelling of two-phase flows over the decades, from the earlier studies by Bray and co-workers [19–21] to the more recent ones (e.g., [22–38]). Modelling and simulation of spray combustion under Diesel engine-like conditions have also been performed (e.g., [39–47]). For premixed flames impinging on walls and interacting with walls, there exist some early theoretical (e.g., [48–50]) and experimental (e.g., [51–53]) studies by Bray and co-workers, and several numerical investigations by other researchers (e.g., [54–59]). However, when it comes to turbulent spray combustion, it is an intricate two-phase phenomenon in itself, involving turbulent mixing, evaporation of the liquid fuel droplets, their dispersion and convection by the carrier gas-phase and combustion of the evaporated fuel, all of which occur simultaneously while influencing each other. Furthermore, the simulation of a spray flame impinging on a wall adds another level of complexity (due to fuel droplets impacting on the wall surface and forming a liquid film on it, and flame-wall interaction), is difficult to model and is demanding in terms of computational resources. Hence, studies involving numerical simulations of spray flames impinging on walls are scarce to the best of the authors' knowledge, with one example being that of Hori et al. [45]. In their study, Hori et al. [45] numerically analysed Diesel spray flames impinging on a flat wall using Reynolds Averaged Navier-Stokes (RANS) simulations, to investigate the relationship between fuel injection pressure and wall heat loss. But, they did not take into account the temporal and spatial variations of temperature inside the wall, nor did they consider the influence of radiative heat transfer on wall heat loss.

In this study, 3-Dimensional numerical simulations of spray flames impinging on a flat wall under CI engine like conditions, are used to analyse the influence of fuel injection velocity (and hence the fuel injection rate) on the wall heat flux (convective, radiative and the sum of both these heat fluxes) and the wall heat flow rate. The differences between simulations in this study and those of previous studies are that, radiative heat transfer and the dynamics of liquid fuel film formed on the wall surface (due to impinging fuel droplets) are taken into account. Additionally, Conjugate Heat Transfer (CHT) is also considered, wherein the heat conduction occurring within the finite thickness wall is coupled with the convective and radiative heat transfer at the wall surface, to track the temperature variations inside the wall. To the best of the authors' knowledge, such a comprehensive analysis of spray flames impinging on a wall in CI engine-like environment, using numerical simulations has not yet been performed.

4.2 Numerical simulation

In the present numerical simulations of spray flames impinging on a wall, neither subgrid-scale turbulence model nor turbulence-chemistry interaction model is used, since fine grids with coarse DNS-like resolution are employed in each simulation (discussed later). Simulations of the two-phase reacting flows are based on an Eulerian-Lagrangian framework [22, 24, 26, 29, 32, 60] in which, the continuous gas-phase is modelled in the classical Eulerian coordinate framework, while the dispersed-phase fuel droplets are tracked individually in the Lagrangian framework as point-masses. Additionally, liquid film formation on the wall surface due to fuel droplet impingement, is captured using a particle-based approach (Lagrangian framework). As mentioned previously, CHT is incorporated in these simulations to couple the spray combustion calculations with the conduction heat transfer occurring inside the solid wall. Details of the various numerical approaches mentioned above, along with information about the models for liquid fuel evaporation, combustion reaction, soot formation and radiation are presented in the following.

4.2.1 Governing equations of gas-phase

Conservation equations of mass, momentum, enthalpy, mixture fraction and progress variable (PV) are solved for the gas-phase, which is treated as an Eulerian continuum, in the following manner:

$$\frac{\partial \rho}{\partial t} + \nabla \cdot (\rho \boldsymbol{u}) = S_\rho \tag{4.3}$$

$$\frac{\partial \rho \boldsymbol{u}}{\partial t} + \nabla \cdot (\rho \boldsymbol{u}\boldsymbol{u}) = -\nabla P + \nabla \cdot \boldsymbol{\tau} + \boldsymbol{S}_\rho \boldsymbol{u} \tag{4.4}$$

$$\frac{\partial \rho h}{\partial t} + \nabla \cdot (\rho h \boldsymbol{u}) = \frac{\partial P}{\partial t} + \boldsymbol{u} \cdot \nabla P + \nabla \cdot (\rho D_h \nabla h) + \boldsymbol{\tau} : \nabla \boldsymbol{u} + S_{\rho h} + \rho Q_{rad} \tag{4.5}$$

$$\frac{\partial \rho Z}{\partial t} + \nabla \cdot (\rho Z \boldsymbol{u}) = \nabla \cdot (\rho D_Z \nabla Z) + S_{\rho Z} \tag{4.6}$$

$$\frac{\partial \rho C}{\partial t} + \nabla \cdot (\rho C \boldsymbol{u}) = \nabla \cdot (\rho D_C \nabla C) + \rho \dot{\omega}_C \tag{4.7}$$

In Eqs. (4.3) - (4.7), ρ is the density, $\boldsymbol{u}$ is the gas-phase velocity vector, $\boldsymbol{\tau}$ is the viscous stress tensor, P is the pressure, h is the specific enthalpy, Z is the mixture fraction, C is the progress variable (PV) defined as the sum of mass fractions of combustion products, i.e. $C = Y_{\mathrm{CO_2}} + Y_{\mathrm{CO}} + Y_{\mathrm{H_2}}$, and $\dot{\omega}_C$ is the reaction rate of C (explained later). D_Z and D_C are the diffusion coefficients of Z and C, respectively, and are assumed to be equal to the gaseous thermal diffusivity D_h under the unity Lewis number assumption ($Le = 1.0$) as:

$$D_Z = D_C = D_h = \frac{\lambda}{\rho c_p} \tag{4.8}$$

where c_p and λ are the specific heat capacity at constant pressure and thermal conductivity, respectively, of the gas-phase. Q_{rad} is the radiative heat source term whose calculation method is described later. Source terms S_ρ, $\boldsymbol{S}_\rho \boldsymbol{u}$, $S_{\rho h}$ and $S_{\rho Z}$ appearing in Eqs. (4.3) - (4.6), take into account the interactions between the gas-phase and the liquid-phase, allowing for two-way coupling between both the phases. These source terms are expressed as:

$$S_\rho = S_{\rho,d} + S_{\rho,l} \tag{4.9}$$

$$\boldsymbol{S}_\rho \boldsymbol{u} = \boldsymbol{S}_\rho \boldsymbol{u}_{,d} + \boldsymbol{S}_\rho \boldsymbol{u}_{,l} \tag{4.10}$$

$$S_{\rho h} = S_{\rho h,d} + S_{\rho h,l} \tag{4.11}$$

$$S_{\rho Z} = S_{\rho Z,d} + S_{\rho Z,l} \tag{4.12}$$

where terms with the subscript d (i.e., $S_{\rho,d}$, $\boldsymbol{S}_{\rho\boldsymbol{u},d}$, $S_{\rho h,d}$ and $S_{\rho Z,d}$) represent the interactions between the dispersed-phase (contribution from each individual fuel droplet) and gas-phase, while the terms with subscript l (i.e., $S_{\rho,l}$, $\boldsymbol{S}_{\rho\boldsymbol{u},l}$, $S_{\rho h,l}$ and $S_{\rho Z,l}$) represent the interactions between the liquid fuel film formed on the wall surface and the gas-phase.

4.2.1.1 Combustion model

Combustion of vaporized n-dodecane (fuel used in this study) is modelled using the Non-Adiabatic Flamelet/Progress Variable (NA-FPV) approach [61, 62]. NA-FPV is a type of flamelet approach in which the influence of heat loss due to latent heat of liquid fuel evaporation, cooled wall and radiative heat transfer, on the variation of each physical quantity is accounted for. With the NA-FPV approach, the conservation equations for mass, momentum, enthalpy, mixture fraction and PV, i.e., Eqs. (4.3) - (4.7), are solved in the physical space, while the mass fractions of various chemical species Y_k and the reaction rate of C ($\dot{\omega}_C$) at each grid point in the gas-phase's computational domain, are extracted from a pre-computed database called the flamelet library. A reduced set of control variables, viz. mixture fraction Z, progress variable C and enthalpy loss Δh are used for extracting Y_k and $\dot{\omega}_C$ from the flamelet library. Here, Δh is the difference between the enthalpy h_0 when there is no heat loss (adiabatic condition) and the enthalpy h in Eq. (4.5) when heat loss is considered. Contrary to the conventional FPV approach, the NA-FPV approach stores flamelet data with heat loss in the flamelet library, which enables accurate prediction of chemical reactions in non-adiabatic combustion fields involving latent heat of evaporation of fuel droplets and liquid fuel film, heat loss through the wall, and heat loss due to radiative heat transfer from soot and gas-phase species. The diffusion flamelet database (flamelet library) is generated using FlameMaster [63] by solving the flamelet equations for 1-Dimensional counter diffusion flame, using a detailed chemical kinetic mechanism of n-dodecane consisting of 255 chemical species and 1466 reactions [64]. Details of the procedure for generating the flamelet library are described in [61, 62].

4.2.2 Governing equations of dispersed-phase fuel droplets

Dynamics of the dispersed-phase fuel droplets (treated as spherical point masses) are described by a set of Lagrangian equations governing the evolution of the fuel spray. Evaporating fuel droplets of the dispersed-phase are individually tracked using a Lagrangian framework [22, 29, 60, 65] by solving the equations for droplet trajectory $\boldsymbol{x}_d$, velocity $\boldsymbol{u}_d$, temperature T_d, and mass m_d in the following manner:

$$\frac{d\boldsymbol{x}_d}{dt} = \boldsymbol{u}_d \tag{4.13}$$

$$\frac{d\boldsymbol{u}_d}{dt} = \frac{f_1}{\tau_d}(\boldsymbol{u} - \boldsymbol{u}_d) + \boldsymbol{g} \tag{4.14}$$

$$\frac{dT_d}{dt} = \left(\frac{Nu_g}{3Pr_g}\right)\left(\frac{c_p}{c_{p,d}}\right)\left(\frac{f_2}{\tau_d}\right)(T - T_d) + \frac{1}{m_d}\left(\frac{dm_d}{dt}\right)\frac{L_V}{c_{p,d}} \tag{4.15}$$

$$\frac{dm_d}{dt} = -\frac{m_d}{\tau_d}\left(\frac{Sh_g}{3Sc_g}\right)\ln(1 + B_M) \tag{4.16}$$

Here, $c_{p,d}$ is the specific heat capacity of fuel droplet, τ_d is the droplet response time in Stokes regime, $\mathbf{g}$ is the acceleration due to gravity, $\boldsymbol{u}$, T, $\mathrm{Pr_g}$ and $\mathrm{Sc_g}$ are the local gas-phase properties, viz. gas-phase velocity, temperature, Prandtl number and Schmidt number, respectively, at the droplet position. Similarly, $\mathrm{Nu_g}$ and $\mathrm{Sh_g}$ are the local gas-phase Nusselt and Sherwood numbers, respectively, at the droplet position, which are calculated using the Ranz-Marshall correlations [66, 67]. L_V is the latent heat of vaporization at the droplet temperature T_d, and B_M is the Spalding mass transfer number. f_1 and f_2 are the correction factors for Stokes drag and interphase heat transfer of evaporating fuel droplets, respectively [29, 60, 68, 69]. A non-equilibrium Langmuir-Knudsen evaporation model [60, 65, 70, 71] is used to capture the evaporation of dispersed-phase fuel droplets in Eq. (4.16). Details of this evaporation model and the calculation procedures for the above-mentioned quantities appearing in Eqs. (4.14) - (4.16) are described elsewhere [22, 26, 29, 68, 69], and interested readers are directed to these studies for further information.

By solving the system of Lagrangian equations (4.13) - (4.16), the source terms accounting for the interactions between dispersed-phase fuel droplets and the gas-phase

(i.e., $S_{\rho,d}$, $\boldsymbol{S}_{\rho\boldsymbol{u},d}$, $S_{\rho h,d}$ and $S_{\rho Z,d}$) in Eqs. (4.9) - (4.12), can be computed using the Particle-Source-In-Cell (PSI-Cell) approach [72] as follows:

$$S_{\rho,d} = -\frac{1}{\Delta V}\sum_{N}\frac{dm_d}{dt} \tag{4.17}$$

$$\boldsymbol{S}_{\rho\boldsymbol{u},d} = -\frac{1}{\Delta V}\sum_{N}\frac{d(m_d\boldsymbol{u}_d)}{dt} \tag{4.18}$$

$$S_{\rho h,d} = -\frac{1}{\Delta V}\sum_{N}\frac{d(m_d h_d)}{dt} \tag{4.19}$$

$$S_{\rho Z,d} = -\frac{1}{\Delta V}\sum_{N}\frac{dm_d}{dt} \tag{4.20}$$

where ΔV is the volume of the computational grid-cell within which a certain fuel droplet resides, h_d is the specific enthalpy of a fuel droplet, and N is the number of fuel droplets within a given computational grid-cell. In the classical PSI-Cell approach, the contribution of a fuel droplet to the above source terms is interpolated to each of the 8 neighbouring grid points of the gas-phase's computational cell (i.e., when the geometry of the Cartesian grid-cell is cuboidal) within which that fuel droplet resides. The interpolation of each droplet's source term contribution is achieved using the conventional trilinear interpolation technique, considering the relative positions of the droplets within a computational cell. However, this simple trilinear interpolation technique can be applied only when the point mass assumption for a droplet is true, meaning the grid-cell size must be about 10 times larger than the droplet size [73, 74]. For the computational grid used in the present simulations, the grid-cell size is of the order of droplet sizes or even smaller than the droplet sizes in certain regions of the computational domain (especially in the regions closer to the wall). Applying the conventional trilinear interpolation technique to the droplet source terms in such regions would lead to erroneous estimates of droplet dynamics, because with this interpolation technique, the range of influence of the evaporating fuel droplets on the gas-phase depends on the grid-cell size. To overcome this drawback, a Gaussian distance function technique proposed by Borghesi et al. [75] is used for interpolating the droplet source term contributions, in the regions where the grid-cell sizes are equal to or smaller than twice the initial Sauter Mean Diameter

(SMD) of the injected fuel spray. This technique allows for the range of influence of the fuel droplets on the gas-phase to be kept constant regardless of the computational cell size. Although the Gaussian distance function interpolation technique is computationally more demanding than the trilinear interpolation technique, it has been used in the above-mentioned regions of the computational domain to capture droplet dynamics accurately. Similar techniques for interpolating the dispersed-phase source terms to the gas-phase have already been applied successfully by other researchers [76, 77]. Details of the implementation of the Gaussian distance function technique are presented in [27, 75].

4.2.3 Spray-wall interaction modelling

When liquid fuel is sprayed directly into the cylinder of a CI engine, there is a possibility of some of the fuel spray impinging on the piston and cylinder walls (before vaporization and mixing are finished), resulting in the formation of liquid films. In this study, the spray-wall interaction phenomena is modelled using a combination of the spray-film interaction model proposed by Stanton and Rutland [78], and the wall film dynamics model proposed by O'Rourke and Amsden [79, 80], which are briefly introduced below.

4.2.3.1 Spray-film interaction model

The behaviour of fuel droplets impinging on a wetted wall surface can be classified into 4 regimes, namely: Stick, Rebound, Spread and Splash, depending on the Weber number We of the incoming dispersed-phase droplets [78], which is defined as:

$$We = \frac{\rho_d d u_{d,n}^2}{\gamma_d} \tag{4.21}$$

where, ρ_d is the droplet density, $u_{d,n}$ is the incoming droplet's velocity component perpendicular to the wall before impingement, and γ_d is the liquid droplet's surface tension. It is assumed that the solid wall surface is covered by a thin film of liquid fuel when the droplet impact occurs. The transition criteria for each regime is decided by the Weber number We, which is calculated using the incident dispersed-phase droplet's wall-normal velocity component $u_{d,n}$, as shown in Eq. (4.21). As suggested by the name

of each regime, the outcome of the collision of a droplet with the film surface can be easily discerned. Droplets undergoing Sticking, Spreading and Splashing phenomena usually contribute to the formation and growth of liquid film on the wall surface, and further details of each impingement regime are discussed in [78].

4.2.3.2 Wall film dynamics model

The wall film dynamics model proposed by O'Rourke and Amsden [79, 80] is a particle-based numerical method used to model the dynamics and evaporation of liquid fuel films formed on the walls of IC engines. Dominant physical phenomena to be considered when tracking the motion of liquid film on the wall surface are summarized in Fig. 4.1. Using the above assumptions and setting the wall velocity $\boldsymbol{u}_w = 0$ (since the wall is kept stationary in the present simulations), the governing equations for the conservation of mass, momentum and energy of the liquid film formulated by O'Rourke and Amsden [79, 80], can be re-written as:

$$\frac{\partial \rho_l h_l}{\partial t} + \nabla \cdot (\rho_l h_l \boldsymbol{u}_l) = \dot{M}_{imp} + \dot{M}_{vap} \tag{4.22}$$

$$\begin{aligned} \rho_l h_l \left\{ \frac{\partial \boldsymbol{u}_l}{\partial t} + \boldsymbol{u}_l \cdot \nabla \boldsymbol{u}_l \right\} + h_l \nabla P_l = \tau_w \boldsymbol{t} - \mu_l(T_l) \frac{\boldsymbol{u}_l}{h_l/2} + \dot{\boldsymbol{P}}_{imp} \\ - (\dot{\boldsymbol{P}}_{imp} \cdot \boldsymbol{n})\boldsymbol{n} - \dot{M}_{imp} \boldsymbol{u}_l + \delta p_l \boldsymbol{n} + \rho_l h_l \mathbf{g} \end{aligned} \tag{4.23}$$

$$\begin{aligned} \rho_l h_l c_{vl} \left\{ \frac{\partial T_l}{\partial t} + \boldsymbol{u}_l \cdot \nabla T_l \right\} = \lambda_l(T_l) \left[\frac{T_s - T_l}{h_l/2} - \frac{T_l - T_w}{h_l/2} \right] \\ + \dot{Q}_{imp} - e_l(T_l) \dot{M}_{imp} \end{aligned} \tag{4.24}$$

where ρ_l is the liquid film's density (temperature-dependent), h_l is the film thickness, $\boldsymbol{u}_l$ is the mean film velocity, T_l is the mean film temperature, T_s is the gas-film interface temperature, T_w is the wall surface temperature, τ_w is the shear stress acting on the gas-side of the wall film (at the gas-film interface), and $\boldsymbol{t}$ is the unit tangent to the wall in the direction of $\boldsymbol{u}_l$. $\mu_l(T_l)$, $\lambda_l(T_l)$ and $e_l(T_l)$ are the liquid film viscosity, thermal conductivity, and internal energy, respectively, at the mean film temperature T_l, and $\mathbf{g}$ is the acceleration due to gravity. $\dot{M}_{imp}$ is the liquid mass source per unit area due to impingement of dispersed-phase fuel droplets, $\dot{M}_{vap}$ is the film evaporation rate/area, P_l

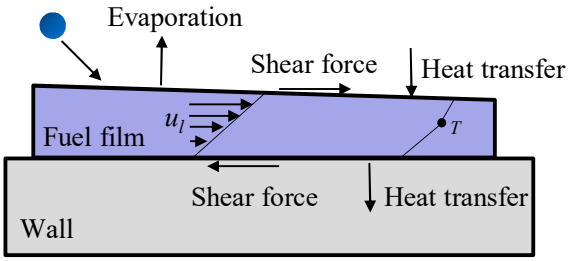

Figure 4.1: Schematic of major physical phenomena governing wall film flow.

is the film pressure arising from the impingement of fuel droplets, $\dot{\boldsymbol{P}}_{imp}$ is the momentum source/area due to collisions of the fuel droplets with the film, $\boldsymbol{n}$ is the unit vector normal to the wall surface, and δp_l is the pressure gradient across the film (in the direction perpendicular to the wall) to satisfy the condition of $\boldsymbol{u}_l \cdot \boldsymbol{n} = 0$. Finally, c_{vl} is the liquid specific heat capacity at constant volume (temperature-dependent), and $\dot{Q}_{imp}$ is the energy source term due to impingement of fuel droplets.

In this model, the particle numerical method [79, 80] is used to track the motion of the wall film, wherein the wall film is assumed to be constituted of several discrete particles as illustrated by the schematic diagram in Fig. 4.2. In this particle method, the dispersed-phase fuel droplets impinging on the solid wall/liquid film and undergoing either Stick, Spread or Splash phenomena, are converted into wall film particles. α denotes the computational cell face on the wall surface (see Fig. 4.2) over which the discrete film particles reside. Calculation method of the wall film source terms corresponding to mass, momentum, and energy, viz. $\dot{M}_{imp}$, $\dot{\boldsymbol{P}}_{imp}$ and $\dot{Q}_{imp}$, respectively, which arise from the

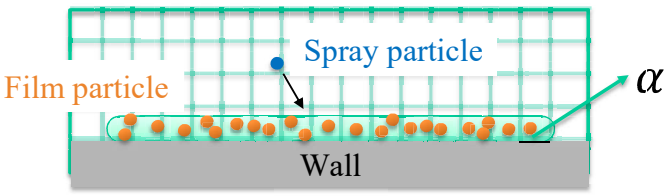

Figure 4.2: Schematic of liquid fuel film formed on the wall. A particle-based approach is used for calculating the wall film dynamics.

impingement of fuel droplets on the wall film surface, over any given computational cell face α, are detailed in [79, 80].

However, there is an important distinction between the numerical solution procedure applied by O'Rourke and Amsden [79], and that applied in our simulations pertaining to: (1) the gas-side heat flux to the liquid film $\dot{Q}_{gas}$, (2) the gas shear stress acting on the gas-film interface τ_w, and (3) the film particle evaporation rate $(\dot{M}_{vap})_p$ (subscript p denotes a wall film particle). In the RANS simulations performed by O'Rourke and Amsden [79], τ_w, $\dot{Q}_{gas}$ and $(\dot{M}_{vap})_p$ are computed using wall functions developed in the context of the K/ϵ turbulence model. However, in this study, τ_w and $\dot{Q}_{gas}$ are calculated directly from the real-time solutions of the numerical simulations, i.e., using the velocity and temperature gradients, respectively, on the gas-side of the gas-film interface, which can be readily computed in the simulations, since fine grid spacing in the wall-normal direction with DNS-like resolution is used. On the other hand, the film particle evaporation rate $(\dot{M}_{vap})_p$ is calculated in this study as [27, 81]:

$$(\dot{M}_{vap})_p = \frac{\rho D_F (\nabla Y_{F,g})_p \cdot \boldsymbol{n}_\alpha}{1 - (Y^{\Gamma}_{F,g})_p} \tag{4.25}$$

where ρ is the gas-phase density above the film surface, D_F is the diffusion coefficient of the fuel vapour calculated using Eq. (4.8), $\boldsymbol{n}_\alpha$ is the unit vector normal to the wall surface on cell face α, and $(Y^{\Gamma}_{F,g})_p$ is the equilibrium fuel vapour mass fraction at the gas-film interface calculated as:

$$(Y^{\Gamma}_{F,g})_p = \frac{(X^{\Gamma}_{F,g})_p}{(X^{\Gamma}_{F,g})_p + [1 - (X^{\Gamma}_{F,g})_p]\overline{W}/W_F} \tag{4.26}$$

$$(X^{\Gamma}_{F,g})_p = \frac{P_{sat,p}}{P} \tag{4.27}$$

where $(X^{\Gamma}_{F,g})_p$ is the fuel vapour mole fraction at the gas-film interface, $P_{sat,p}$ is the saturated vapour pressure corresponding to the gas-film interface temperature $T_{s,p}$, and W_F and $\overline{W}$ are the molecular mass of fuel vapour and the gas-phase's average molecular mass, respectively. In this study, the liquid film evaporation rate given in Eq. (4.25) is modelled under the assumption of vapour-liquid equilibrium at the gas-film interface. The physical meaning of Eq. (4.25) is that, film vaporization occurs due to the difference

between the mass fraction of fuel vapour at the gas-film interface and in the bulk gas above the film surface.

For further details pertaining to the wall film dynamics model, its sub-models and numerical implementation, interested readers are directed to the original works of O'Rourke and Amsden [79, 80]. Finally, using the solution of the wall film dynamics model, closures for the source terms required to couple the wall film with the gas-phase, i.e., $S_{\rho,l}$, $\boldsymbol{S}_{\rho\boldsymbol{u},l}$, $S_{\rho h,l}$ and $S_{\rho Z,l}$, appearing in Eqs. (4.9) - (4.12) can be computed as:

$$S_{\rho,l} = -\frac{1}{\Delta V}\sum_{N_{p,\alpha}} \frac{dm_p}{dt} \tag{4.28}$$

$$\boldsymbol{S}_{\rho\boldsymbol{u},l} = -\frac{1}{\Delta V}\sum_{N_{p,\alpha}} \left(\frac{dm_p}{dt}\boldsymbol{u}_p\right) \tag{4.29}$$

$$S_{\rho h,l} = -\frac{1}{\Delta V}\sum_{N_{p,\alpha}} \left(\frac{dm_p}{dt}h_p\right) \tag{4.30}$$

$$S_{\rho Z,l} = -\frac{1}{\Delta V}\sum_{N_{p,\alpha}} \frac{dm_p}{dt} \tag{4.31}$$

where $N_{p,\alpha}$ is the number of film particles residing on the cell face α (on the wall surface), and m_p, $\boldsymbol{u}_p$ and h_p are the mass, velocity and specific enthalpy of wall film particle p, respectively. The contribution of each wall film particle to the above source terms used for phase coupling, is then interpolated to the grid points of the gas-phase above the film surface, using the Gaussian distance function technique mentioned in Section 4.2.2.

4.2.4 Radiation and soot formation models

Models used in the present numerical simulations to account for radiation heat transfer and soot formation, are briefly described here, since extensive literature on these models already exist. For the computation of radiation heat transfer, the Radiative Transfer Equation (RTE) shown in Eq. (4.32) below, is solved by using the Discrete Ordinates (DO) method with S8 quadrature set [82].

$$\frac{dI_\lambda(\vec{r},\vec{s})}{ds} = \kappa_\lambda(\vec{r})\{I_{b\lambda}(\vec{r}) - I_\lambda(\vec{r},\vec{s})\} \tag{4.32}$$

Here, $I_\lambda(\vec{r},\vec{s})$ is the spectral radiation intensity, which is a function of the position vector $\vec{r}$ and the direction vector $\vec{s}$, $I_{b\lambda}(\vec{r})$ is the blackbody spectral intensity at the temperature of the medium, and κ_λ is the spectral Planck mean absorption coefficient. By integrating $I_\lambda(\vec{r},\vec{s})$ obtained from Eq. (4.32) over wavelength λ and solid angle Ω, the net radiant power per unit volume (ρQ_{rad}) can be calculated as shown below:

$$\rho Q_{rad} = -\int_{4\pi}\left[\int_0^\infty \kappa_\lambda(\vec{r})\left\{I_{b\lambda}(\vec{r}) - I_\lambda(\vec{r},\vec{s})\right\} d\lambda\right] d\Omega \tag{4.33}$$

where Q_{rad} is the radiative heat source term appearing in the gas-phase enthalpy conservation Eq. (4.5). Thus, the RTE is coupled with the gas-phase enthalpy conservation equation through Q_{rad}. The radiative wall heat flux $q_{w,rad}$ is calculated as shown in Eq. (4.34) below:

$$q_{w,rad} = \int_{\vec{s}\cdot\vec{n}<0} I_{absorbed}\left|\vec{s}\cdot\vec{n}\right| d\Omega - \int_{\vec{s}\cdot\vec{n}>0} I_{emitted}\left|\vec{s}\cdot\vec{n}\right| d\Omega \tag{4.34}$$

where, $\vec{n}$ is the wall-normal vector, and $I_{absorbed}$ and $I_{emitted}$ are the intensities of radiation absorbed and emitted by the wall surface. Dominant radiating entities considered in this study are soot and gas-phase species viz. CO, CO_2, and H_2O, all of which are assumed to be gray (Planck mean absorption coefficient of each gas-phase specie is calculated based on the data from HITEMP 2010 high-resolution database [83]) to keep computational costs realizable. The calculation methodology for the Planck mean absorption coefficients of gas-phase species (CO, CO_2, and H_2O) is described in [84], and that for the Planck mean absorption coefficient of soot is described in [85].

Soot formation is predicted using the Moss-Brookes model [86, 87] in the present simulations, in order to account for the radiative heat transfer from soot. In this model, the transport equations for the soot number density and mass density are solved for predicting soot formation due to inception, coagulation, surface growth, and oxidation as described in [27, 87, 88]. Precursor models based on Polycyclic Aromatic Hydrocarbons (PAH) [89] are employed for the computation of inception process. Mass fractions of C_2H_2, C_6H_5, C_6H_6, H_2 and OH, required for the computations of different processes in the soot model are obtained from the flamelet library [27, 87]. Although this soot

formation model cannot provide the soot particle size distribution, it is computationally less expensive than the other more sophisticated models.

4.2.5 Implementation of Conjugate Heat Transfer (CHT)

To couple the heat transfer occurring at the wall surface from the spray flame, liquid film formed on the wall surface, and radiation, with the unsteady heat conduction occurring inside the stationary solid wall, it is necessary to solve the 3-Dimensional transient heat conduction equation show in Eq. (4.35) below, along with the application of appropriate boundary conditions at the gas-wall and film-wall interfaces.

$$(\rho_{\mathrm{s}} c_{\mathrm{s}}) \frac{\partial T_{\mathrm{s}}}{\partial t} = \frac{\partial}{\partial x}\left(\lambda_{\mathrm{s}} \frac{\partial T_{\mathrm{s}}}{\partial x}\right) + \frac{\partial}{\partial y}\left(\lambda_{\mathrm{s}} \frac{\partial T_{\mathrm{s}}}{\partial y}\right) + \frac{\partial}{\partial z}\left(\lambda_{\mathrm{s}} \frac{\partial T_{\mathrm{s}}}{\partial z}\right) \tag{4.35}$$

Here, ρ_{s}, c_{s} and λ_{s} are the temperature-dependent density, specific heat capacity and thermal conductivity, respectively, of the wall material (iron), and T_{s} is the temperature inside the wall. By solving the above heat conduction equation, the temporal and spatial variations of temperature inside the wall can be computed. Total heat flux at the wall surface $q_{w,total}$ is calculated as the sum of the convective heat flux $q_{w,conv}$ and the radiative heat flux $q_{w,rad}$ as:

$$q_{w,total} = q_{w,conv} + q_{w,rad} \tag{4.36}$$

where the convective heat flux at the wall surface $q_{w,conv}$ is calculated using Eq. (4.37) based on Fourier's law, and the radiative heat flux at the wall surface $q_{w,rad}$ is calculated from Eq.(4.34) using the Discrete Ordinates method [82].

$$q_{w,conv} = -\lambda \left(\frac{\partial T}{\partial x}\right) \tag{4.37}$$

4.2.5.1 Interface boundary conditions

The schematic diagram in Fig. 4.3 illustrates the three phases (gas, liquid film and solid wall) among which heat transfer occurs. For coupling the heat exchange between the liquid film and the wall, the heat flux balance equation at the liquid film-wall interface must be solved implicitly, under the constraint that the liquid film temperature T_l and

the wall temperature T_s at the film-wall interface are equal, as shown below:

$$\begin{cases} q_{w,conv}\left(=\lambda_l \frac{\overline{T}_{l,c}-T_{l,w}}{h_l/2}\right)+q_{w,rad}=-\lambda_s\left(\frac{\partial T}{\partial x}\right)_s & \text{(at the wall surface)} \\ T_{l,w}=T_s \end{cases} \tag{4.38}$$

In the above equation, $\overline{T}_{l,c}$ represents the mean film temperature at the center of the film, and $T_{l,w}$ represents the liquid film temperature at the wall surface. A similar heat flux balance equation must be solved implicitly for the gas-wall interface, under the constraint of equal gas-phase temperature T_g and wall temperature T_s at the gas-wall interface, in order to couple the heat exchange between the gas-phase and wall:

$$\begin{cases} q_{w,conv}\left(=-\lambda_g\left(\frac{\partial T}{\partial x}\right)_g\right)+q_{w,rad}=-\lambda_s\left(\frac{\partial T}{\partial x}\right)_s & \text{(at the wall surface)} \\ T_g=T_s \end{cases} \tag{4.39}$$

In Eqs. (4.38) and (4.39) above, the subscripts l, g and s denote the physical quantities of the liquid fuel film, the gas-phase and the solid wall, respectively. The liquid film is thin enough to assume that its transmissivity is 1.0, and therefore, all the radiation penetrates the liquid film and reaches the wall.

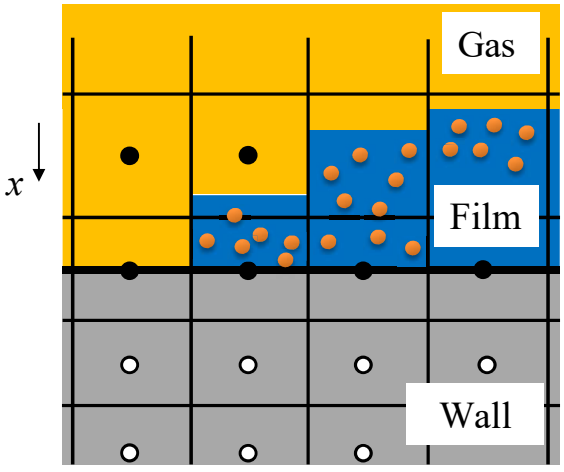

Figure 4.3: Schematic of conjugate heat transfer among gas, film and wall.

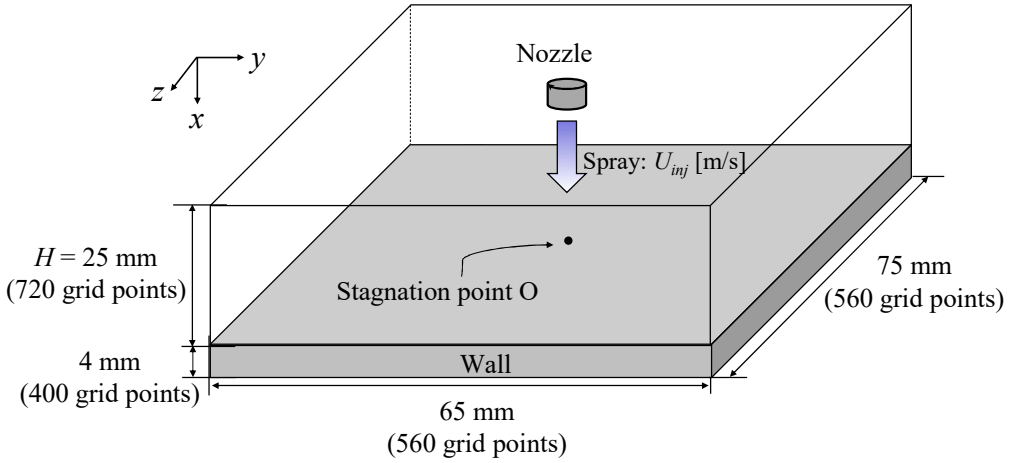

Figure 4.4: Schematic of the computational domain used in the simulations.

4.2.6 Computational configuration and solution algorithm

Schematic of the computational domain used in the present simulations is depicted in Fig. 4.4. The domain's dimensions are the same as those of the combustion chamber apparatus used in a previous experimental study by Inagaki et al. [15]. For the spray flame calculations, the computational domain measures 25 mm × 65 mm × 75 mm in the x-, y- and z-directions, respectively. The spray nozzle is located at the top as shown in the figure, and the point on the nozzle axis at the nozzle exit plane is the origin of the computational domain. The spray flame simulations are performed on a non-uniform staggered Cartesian grid consisting of 720 × 560 × 560 grid points in the x-, y- and z-directions, respectively, so the total number of grid points used for the gas-phase in each simulation case is approximately 226 Million. For the spray flame computations, minimum grid spacing of $\Delta x = 2.9$ μm, $\Delta y = \Delta z = 40$ μm are used, and the grid resolution is adequate in the core regions of the jet spray flames, near the wall and other regions where combustion occurs (discussed in Section 4.3.1.2). In the experiment [15], firstly, premixed Hydrogen-Air mixture was charged into the combustion chamber and ignited using a spark plug. Subsequently, the flame propagated throughout the chamber

creating a high pressure and temperature gas. The resulting ambient pressure and temperature inside the chamber were 3.0 MPa and 1600 K, respectively. Hence, ambient gas temperature and pressure of 1600 K and 3.0 MPa, respectively, are used in the simulations. The ambient gas initially consists of N_2, O_2, and H_2O, whose volume fractions are 0.60, 0.21, and 0.19, respectively.

Dimensions of the solid wall's computational domain are 4 mm × 65 mm × 75 mm in the x-, y- and z-directions, respectively. This means that the wall thickness is 4 mm and it is uniformly discretized using 400 grid points in the wall-normal x-direction, yielding a grid spacing of $\Delta x_{\text{wall}} = 10$ μm. The grid spacing and the number of grid points in the y- and z-directions are the same as those of the spray flame's computational domain (i.e., 560 grid points each in the y- and z-directions). No-slip velocity boundary condition is imposed on the upper wall surface which is exposed to the spray flame and the liquid fuel film. The initial temperature distribution inside the wall varies linearly in the x-direction, from 481 K at the upper surface (flame side) to 463 K at the bottom surface as depicted in Fig. 4.5. The bottom surface of the wall is kept isothermal at 463 K throughout the duration of each simulation (similar to the experiment), and the wall surface emissivity ε is assumed to be unity ($\varepsilon = 1.0$). In Fig. 4.4, the stagnation point "O" on the upper surface of the wall, refers to the point where the nozzle/spray axis intersects the wall surface (i.e., radial location $r = 0$). At the start of each simulation,

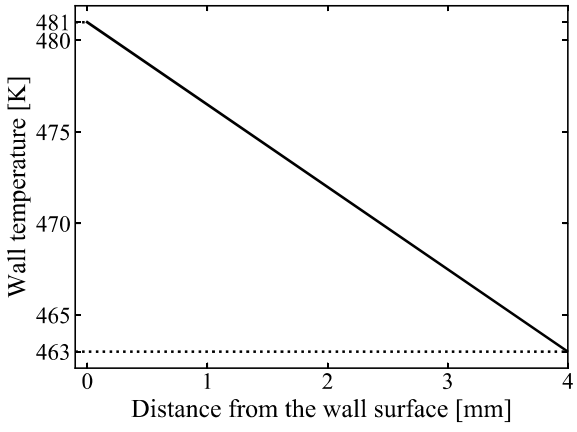

Figure 4.5: Initial temperature distribution inside the wall.

Table 4.1: Cases simulated in this study and their corresponding conditions and fuel injection parameters.

	Case1	Case2	Case3
Fuel injection velocity u_{inj} [m/s]	100	150	216
Fuel injection rate [mg/ms]	0.39	0.59	0.85
Fuel injection period [ms]	1.62	1.08	0.75
Injected fuel mass m_{inj} [mg]	0.64	0.64	0.64
Injection Mach number ($M_{inj} = u_{inj}/C_{amb}$)	0.126	0.189	0.272
Maximum Mach number observed in simulation	0.24	0.39	0.55
Spray cone angle θ [°]	3.94	4.54	5.16
Sauter Mean Diameter (SMD) [μm]	18.5	13.6	10.3
Xr	25.1	18.0	13.3
N	3	3	3
Wall clock time [hours]	258	315	363
CPU-hours	412,800	504,000	580,800

n-dodecane fuel droplets with an initial temperature of 330 K are injected into the computational domain from the nozzle exit plane at the top of the domain. The nozzle diameter is 0.083 mm, which is same as that of the experiment. Table 4.1 summarizes the cases simulated in this study in terms of their fuel injection parameters. In order to investigate the influence of fuel injection velocity u_{inj} on the wall heat loss, three cases with u_{inj} values of 100 m/s, 150 m/s and 216 m/s are considered. The injection Mach number M_{inj} based on the fuel injection velocity u_{inj} and the speed of sound in ambient gas $C_{amb} \approx 795$ m/s, for each case is listed in Table 4.1. The maximum Mach number observed in each case's simulation is also provided in Table 4.1. The time variations of injected fuel mass in all three cases are depicted in Fig. 4.6, where the slope of each line corresponds to the fuel injection rate listed in Table 4.1. In all three cases, the simulations are performed until 0.64 mg of fuel is injected, as shown in Fig. 4.6. The spray cone angle used for injecting the fuel droplets into the computational

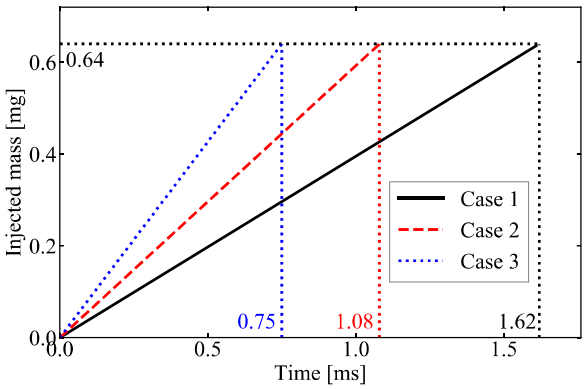

Figure 4.6: Time variations of injected fuel mass.

domain in each case, is calculated using the following empirical formula obtained from experiments [90]:

$$\theta = c\left(\frac{\rho_a}{\mu_a^2}\right)(P_{inj} - P_a)^{0.18}\left(\frac{L_n}{D_n}\right)^{-0.14} \tag{4.40}$$

where $c = 0.00121$, D_n is the nozzle diameter in meters ($D_n = 0.083 \times 10^{-3}$m), L_n is the nozzle length in meters ($L_n = 0.68 \times 10^{-3}$ m), P_a is the ambient pressure in Pascals, P_{inj} is the fuel injection pressure in Pascals, μ_a is the ambient gas-phase dynamic viscosity [Pa $\cdot$ s], and ρ_a is the ambient gas-phase density [kg/m^3]. The fuel injection pressure P_{inj} for a given fuel injection rate (or fuel injection velocity u_{inj}) can be calculated from Hiroyasu's equation [91]:

$$u_{inj} = 0.39\sqrt{2(P_{inj} - P_a)/\rho_d} \tag{4.41}$$

Distributions of the fuel droplet diameter d are prescribed using the Rosin-Rammler [92] volume-based Probability Density Function (PDF) $f_v(d)$, shown in Eq. (4.42) below. These size distribution PDFs for the fuel sprays that are injected from the nozzle exit, are obtained from the best-fit curves to the experimental data provided by Toyota Central R&D Labs., Inc. However, in the simulations, the volume-based PDFs are converted into number-based PDFs $f_n(d)$ using Eq. (4.43), while injecting the fuel droplets.

$$f_v(d) = \frac{N}{X_r}\left(\frac{d}{X_r}\right)^{N-1}\exp\left\{-\left(\frac{d}{X_r}\right)^N\right\} \tag{4.42}$$

$$f_n(d) = \frac{\frac{1}{d^3}f_v(d)}{\int_{d_{min}}^{d_{max}}\frac{1}{d^3}f_v(d)dd} \tag{4.43}$$

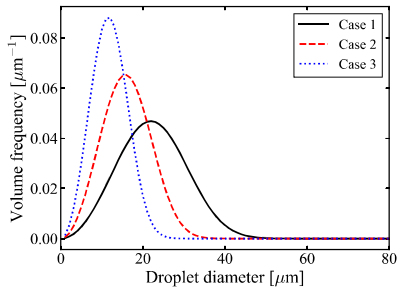

(a) Volume frequency

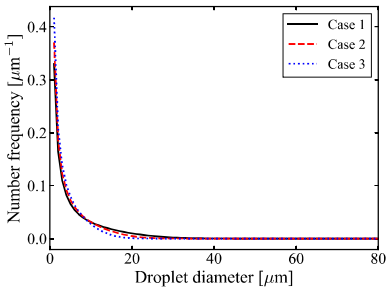

(b) Number frequency

Figure 4.7: Droplet size distributions of injected fuel droplets in all three cases.

In Eq. (4.42), N and X_r are the function parameters obtained from experimental measurements [15]. The minimum and maximum injected droplet diameters are $d_{min} = 1$ μm and $d_{max} = 80$ μm, respectively. Figure 4.7 shows both the volume-based and number-based droplet size distributions of the injected fuel spray, corresponding to the different fuel injection velocities u_{inj} of the three cases. It is evident from Fig. 4.7(a) that, the droplet size distribution becomes biased towards the smaller droplet diameters as the fuel injection velocity u_{inj} increases, and hence the reduction in the SMD of the injected fuel droplets with increasing u_{inj} in Table 4.1.

The fuel injection parameters listed in Table 4.1 are the same as those in the experiments of Inagaki et al. [15]. However, it can be seen that when the fuel injection velocity is changed, other parameters such as fuel injection rate, spray cone angle and SMD also change. This is a limitation of the fuel injector used in the experiment, wherein for a fuel injector of a given nozzle diameter, varying the fuel injection velocity will inevitably change the other parameters. So, it is very difficult to isolate the effect of fuel injection velocity alone, in the experiment. Main factors governing the heat transfer occurring during the interaction between impinging spray flame and wall, are the flame temperature and the velocity with which the flame impinges on the wall. The fuel injection velocity directly influences the impingement velocity of flame, and therefore it is obviously an important parameter. On the other hand, spray cone angle and SMD do not have strong effects on the impingement velocity of the flame. However, we do

acknowledge that the fuel injection rate and SMD affect the heat release rate, and hence the flame temperature. But, as will be shown later, the fuel injection velocity does not influence the flame temperature appreciably in the near wall region, in the present simulations. In the experiments, only the fuel injection velocity was varied and its effect on heat transfer to the wall was investigated. The simulations in this study are mimicking the experiments and therefore, we have only varied the fuel injection velocity and the other parameters which inevitably change as a consequence of varying the fuel injection velocity, have been matched with those of the experiments [15] and used as it is.

The simulations are performed using an in-house thermal flow analysis code called FK^3 [93]. The FK^3 code employs a pressure-based semi-implicit solver for compressible flows, whose algorithm consists of a fractional-step method [94]. The FK^3 code has been successfully applied for simulating various types of gaseous and spray combustion problems, and has also been extensively validated [93]. In the present simulations, the spatial derivatives of the convective terms in the momentum equation are evaluated using a 4^{th} order accurate finite difference scheme [95] that conserves kinetic energy locally, and the spatial derivatives of the convective terms in the governing equations of the scalar quantities are evaluated using the 5^{th} order WENO (Weighted Essentially Non-Oscillatory) scheme [96]. Time integration of the convective terms is performed using a 3^{rd} order explicit TVD Runge-Kutta scheme. Gas-phase thermophysical properties (c_p, c_v, λ and μ) taking temperature dependence into account are computed according to CHEMKIN [97, 98]. Thermopysical properties of liquid fuel (i.e., dispersed-phase droplets and wall film particles) are computed using temperature polynomial functions generated from the NIST database [99]. The solid wall's material is iron and its thermophysical properties, viz. density, specific heat capacity and thermal conductivity, are computed using temperature polynomial functions generated from the database of Valencia et al. [100]. Each simulation was performed using 1600 cores on the HPE SGI8600 supercomputer at the Central Research Institute of Electric Power Industry (CRIEPI), Japan. The wall clock time and CPU hours for each case are listed in Table 4.1.

4.3 Results and discussion

4.3.1 Combustion field

Analyses of the results pertaining to the spray combustion fields, obtained from the numerical simulations are now presented. Simulation results of Case 3 are also compared with available experimental measurements.

4.3.1.1 Features of wall impinging spray flames

Instantaneous distributions of gas-phase temperature in the central x-y plane and at progressing time instances, are shown for all the three cases in Figs. 4.8 to 4.10. Each time instance corresponds to a specific value of injected fuel mass, since (injected fuel mass) = (fuel injection rate) $\times$ (elapsed time). The white entities in these figures represent the dispersed-phase fuel droplets and the particles belonging to the liquid fuel film formed on the wall surface. It is evident from these figures that the gas-phase temperature in the spray jets' core regions, where majority of the fuel droplets exist, is relatively low owing to the latent heat of fuel droplet evaporation. Injected fuel droplets evaporate as they flow downstream and the evaporated fuel mixes with the surrounding hot ambient gas, and gets ignited by it. Subsequent combustion of the fuel vapours occurs as is evident from the high temperature regions in the figures. With increasing downstream distance from the nozzle exit, fuel droplet size decreases and a considerable reduction in the number density of fuel droplets is also observed, as a consequence of evaporation and combustion. In all the three cases, the vaporized fuel auto-ignited at some distance away from the spray nozzle exit, and no special treatment was applied for igniting the vaporized fuel. As time advances, it can be confirmed that the spray flames impinge on the flat wall surface at time instances $t \approx 0.38$ ms, $t \approx 0.27$ ms and $t \approx 0.19$ ms, respectively, in Case 1, Case 2 and Case 3. These time instances correspond to an injected fuel mass value of $m_{inj} = 0.15$ mg ~ 0.16 mg, among the three cases. After impinging on the wall, the flames start spreading in the direction parallel to the wall surface.

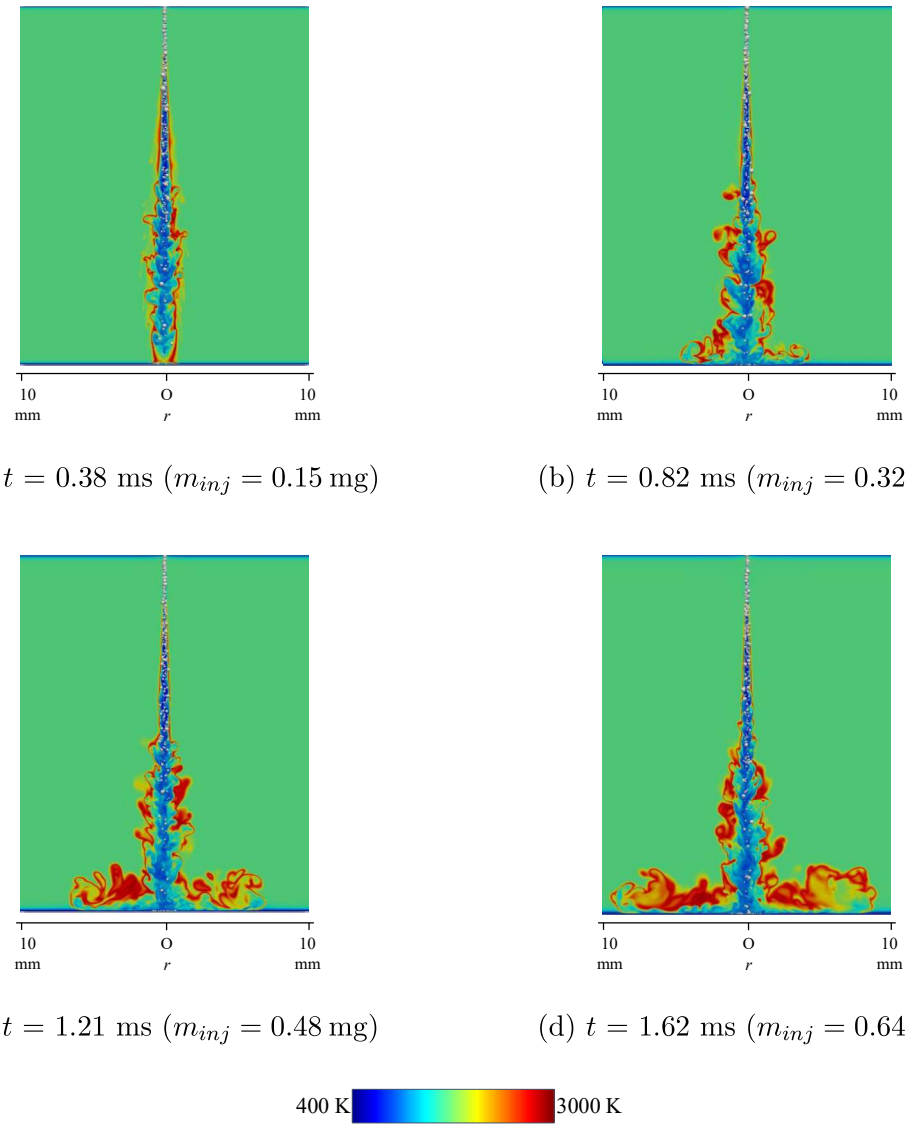

(a) $t = 0.38$ ms ($m_{inj} = 0.15$ mg)

(b) $t = 0.82$ ms ($m_{inj} = 0.32$ mg)

(c) $t = 1.21$ ms ($m_{inj} = 0.48$ mg)

(d) $t = 1.62$ ms ($m_{inj} = 0.64$ mg)

Figure 4.8: Instantaneous distributions of gas-phase temperature along with spray and film particles (particle sizes are exaggerated) in the central x-y plane for Case 1, at progressing time instances corresponding to increasing values of injected fuel mass m_{inj}. Only some fuel droplets are shown in these temperature distributions for the sake of clarity.

Since no significant qualitative differences can be discerned visually, among the combustion fields of the three cases in Figs. 4.8 - 4.10, the combustion field of Case 3 ($u_{inj} = 216$ m/s) alone will be analysed in the following for the sake of brevity. Instantaneous distributions of the iso-surfaces of gas-phase temperature at 1700 K (coloured in yellow) and 2200 K (coloured in red) are shown in Fig. 4.11, along with the dispersed-

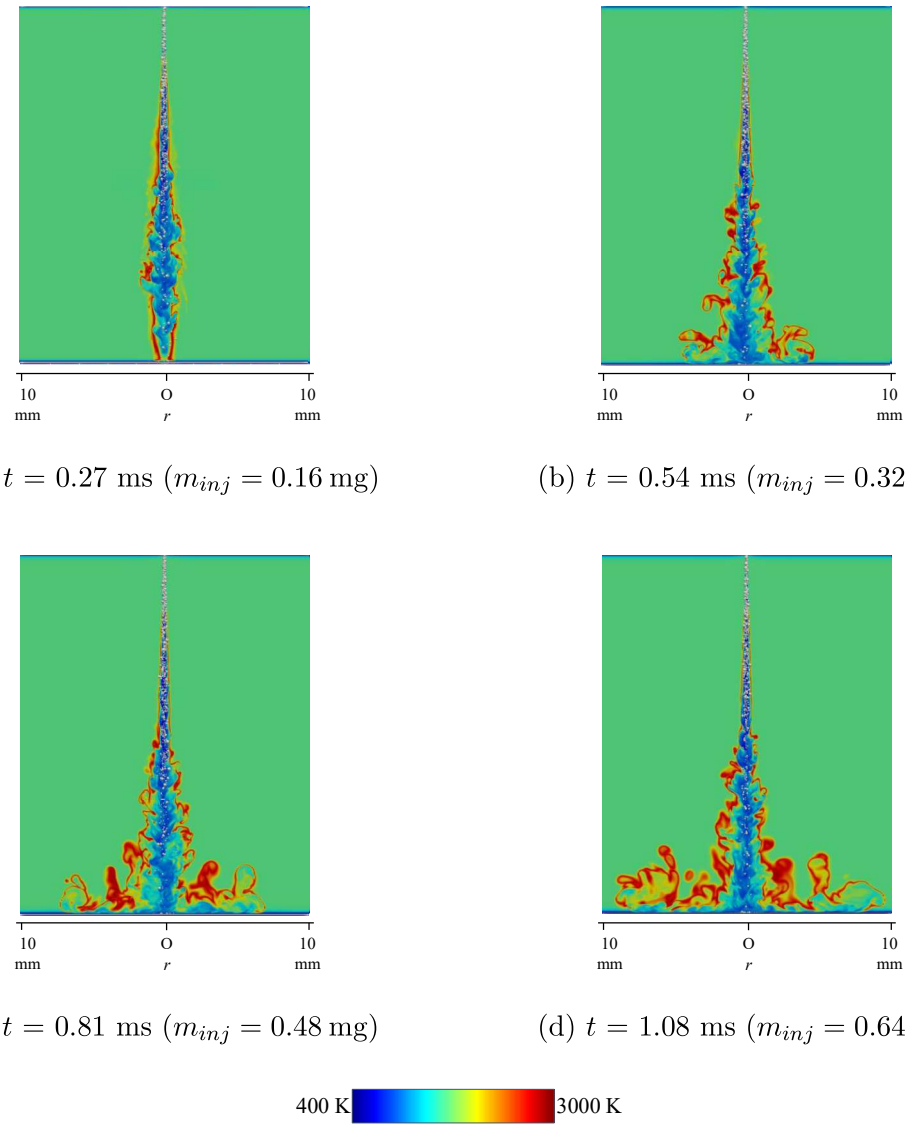

(a) $t = 0.27$ ms ($m_{inj} = 0.16$ mg)

(b) $t = 0.54$ ms ($m_{inj} = 0.32$ mg)

(c) $t = 0.81$ ms ($m_{inj} = 0.48$ mg)

(d) $t = 1.08$ ms ($m_{inj} = 0.64$ mg)

Figure 4.9: Instantaneous distributions of gas-phase temperature along with spray and film particles (particle sizes are exaggerated) in the central x-y plane for Case 2, at progressing time instances corresponding to increasing values of injected fuel mass m_{inj}. Only some fuel droplets are shown in these temperature distributions for the sake of clarity.

phase fuel droplets (coloured entities) which are coloured by their respective evaporation rate $\dot{m}_d$, for Case 3. The distributions are shown at the time instance when injected fuel mass $m_{inj} = 0.64$ mg. The red iso-surface for 2200 K envelopes the yellow iso-surface for 1700 K in most regions, which is why the overall colour of the temperature iso-surfaces appears to be orange. The figure reveals that the evaporation rate of the fuel droplets

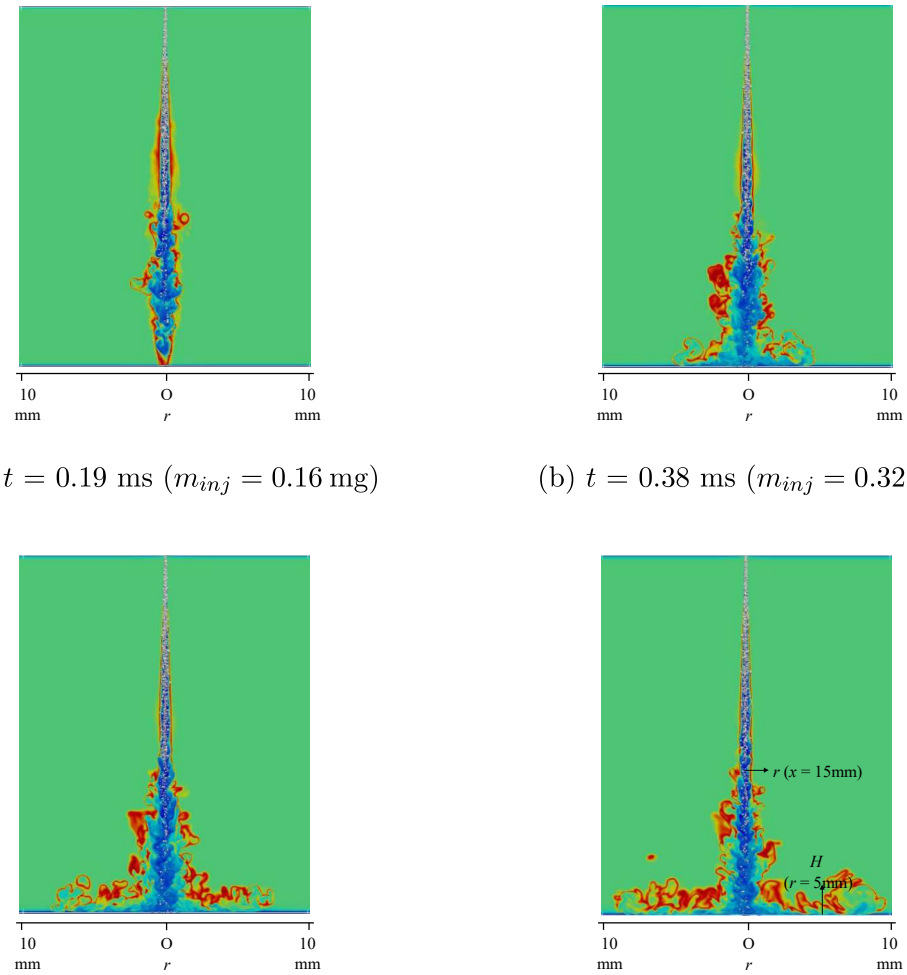

(a) $t = 0.19$ ms ($m_{inj} = 0.16$ mg)

(b) $t = 0.38$ ms ($m_{inj} = 0.32$ mg)

(c) $t = 0.56$ ms ($m_{inj} = 0.48$ mg)

(d) $t = 0.75$ ms ($m_{inj} = 0.64$ mg)

Figure 4.10: Instantaneous distributions of gas-phase temperature along with spray and film particles (particle sizes are exaggerated) in the central x-y plane for Case 3, at progressing time instances corresponding to increasing values of injected fuel mass m_{inj}. Only some fuel droplets are shown in these temperature distributions for the sake of clarity.

becomes higher in the streamwise direction as they move into the hotter regions of the combustion field. For the time instance at which these temperature iso-surfaces are shown, the spray flame has already impinged on the wall surface and started spreading over it. In order to investigate the combustion characteristics and the chemical structure of the flame, in the free shear layer of the spray jet flame in Case 3, Fig. 4.12 depicts

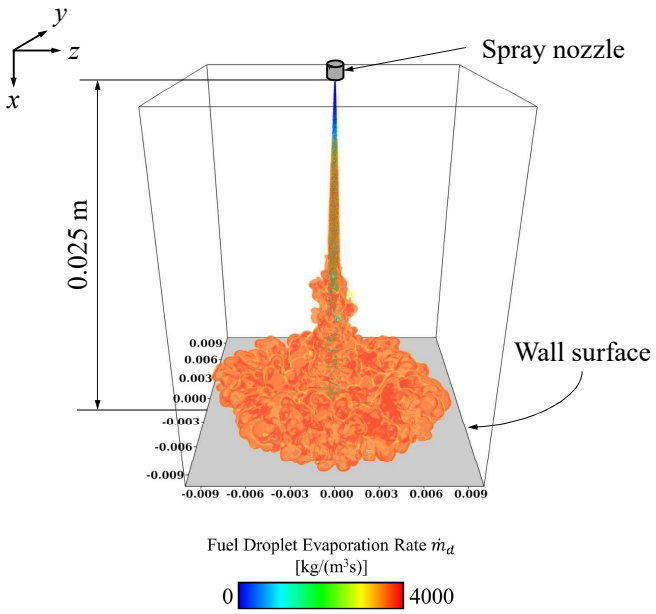

Figure 4.11: Instantaneous distributions of the iso-surfaces of gas-phase temperature at 1700 K (coloured in yellow) and 2200 K (coloured in red), along with the dispersed-phase fuel droplets coloured by their respective evaporation rate $\dot{m}_d$, at the time instance corresponding to injected fuel mass $m_{inj} = 0.64$ mg for Case 3. (Dimensions shown in all Cartesian directions are in meters).

the radial (r-direction) distributions of spatially averaged mass fractions of $C_{12}H_{26}$, O_2, OH, CO, and CO_2 (i.e., $Y_{C_{12}H_{26}}$, Y_{O_2}, Y_{OH}, Y_{CO}, and Y_{CO_2}, respectively), and the radial distributions of spatially averaged reaction rate of progress variable $\dot{\omega}_C$, evaporation rate of dispersed-phase fuel droplets $\dot{m}_d$, and gas-phase temperature T. Radial distributions of all these quantities are plotted for the streamwise location of $x = 15$ mm from the nozzle exit, and at the time instance corresponding to $m_{inj} = 0.64$ mg [see Fig. 4.10(d)]. Here, "spatial averaging" implies averaging performed along the circumference of a circle of a given radius r, whose center is situated at $r = 0$ (i.e., at the axis of the nozzle/spray jet). Figure 4.12(a) shows that the mass fraction of gaseous fuel $Y_{C_{12}H_{26}}$ is higher in the central region of the spray jet, due to the high evaporation rate of fuel droplets $\dot{m}_d$ in that region, and decreases towards the ambient. On the other hand, the mass fraction of oxidizer O_2 (i.e., Y_{O_2}) is larger outside the jet, and decreases to a small value towards the axis of the spray jet (i.e., at $r = 0$). Therefore, the radial distributions of the mass fractions of both fuel ($Y_{C_{12}H_{26}}$) and oxidizer (Y_{O_2}), decrease towards the region of the mixing layer where the reaction zone represented by the high value of reaction rate $\dot{\omega}_C$

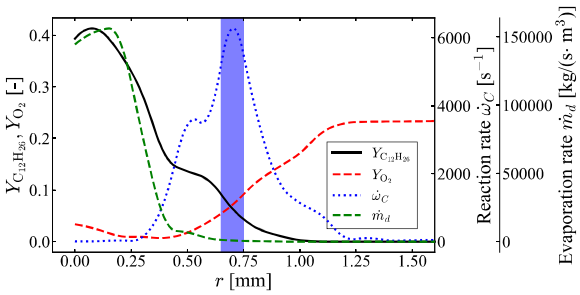

(a) $Y_{C_{12}H_{26}}$, Y_{O_2}, $\dot{\omega}_C$, $\dot{m}_d$

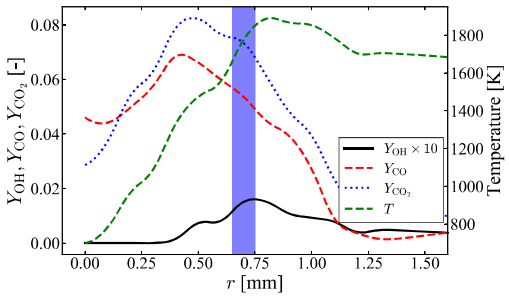

(b) Y_{OH}, Y_{CO}, Y_{CO_2}, T

Figure 4.12: Radial distributions of spatially averaged (a) mass fraction of $C_{12}H_{26}$, $Y_{C_{12}H_{26}}$, mass fraction of O_2, Y_{O_2}, reaction rate of progress variable, $\dot{\omega}_C$ and evaporation rate, $\dot{m}_d$, and (b) mass fraction of OH, Y_{OH}, mass fraction of CO, Y_{CO}, mass fraction of CO_2, Y_{CO_2} and temperature, T at $x = 15$ mm for Case 3. Regions marked by blue bands in (a) and (b) indicate the location of peak reaction rate, $\dot{\omega}_C$.

exists, thereby indicating the formation of a diffusion flame. The blue bands in Figs. 4.12(a) and 4.12(b) indicate the radial location of peak reaction rate $\dot{\omega}_C$. Moreover, the radial distribution of $\dot{\omega}_C$ shows that combustion reaction does not occur in the center of the jet where many fuel droplets are present, because the high evaporation rate $\dot{m}_d$ in this region leads to fuel-rich conditions that are unconducive for combustion to occur. On the contrary, combustion occurs at the outer edge of the free shear layer where the most favourable mixing of fuel and oxidizer can be achieved, such that the mass fractions of fuel and oxidizer are closer to their stoichiometric proportions. Furthermore, from Fig. 4.12(b) it can be confirmed that the mass fraction of OH (an intermediate radical

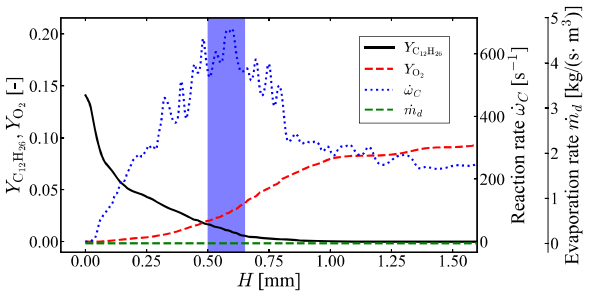

(a) $Y_{C_{12}H_{26}}$, Y_{O_2}, $\dot{\omega}_C$, $\dot{m}_d$

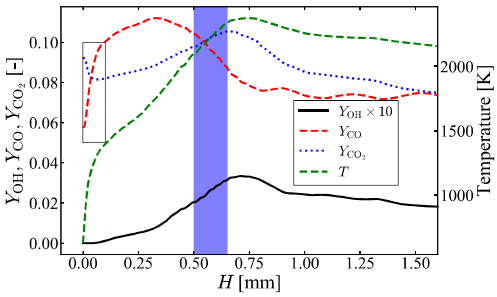

(b) Y_{OH}, Y_{CO},Y_{CO_2}, T

Figure 4.13: Streamwise distributions of spatially averaged (a) mass fraction of $C_{12}H_{26}$, $Y_{C_{12}H_{26}}$, mass fraction of O_2, Y_{O_2}, reaction rate of progress variable, $\dot{\omega}_C$ and evaporation rate, $\dot{m}_d$, and (b) mass fraction of OH, Y_{OH}, mass fraction of CO, Y_{CO}, mass fraction of CO_2, Y_{CO_2} and temperature, T at $r = 5$ mm for Case 3. H is the height above the wall surface. Regions marked by blue bands in (a) and (b) indicate the location of peak reaction rate, $\dot{\omega}_C$.

specie of combustion reaction) attains maxima very close to the reaction zone, and so does the gas-phase temperature T, due to the heat released by combustion.

Next, to investigate the combustion characteristics and the chemical flame structure in the near wall region of Case 3, the streamwise distributions of spatially averaged values of $Y_{C_{12}H_{26}}$, Y_{O_2}, Y_{OH}, Y_{CO}, Y_{CO_2}, $\dot{\omega}_C$, $\dot{m}_d$ and T, at the radial location of $r = 5$ mm from the spray axis and the time instance corresponding to $m_{inj} = 0.64$ mg [see Fig. 4.10(d)], are shown Fig. 4.13. In other words, these streamwise distributions represent the variations of the aforementioned quantities with height H above the wall surface

(where $H = 0$ represents the wall surface). In Fig. 4.13(a), it is observed that $\dot{m}_d$ is zero at all heights above the wall surface in the near wall region, because there are no fuel droplets or liquid film particles at this radial location ($r = 5$ mm). However, gaseous fuel exists at this location's near wall region which is a result of the convection of vaporized fuel from the center region of the spray jet. Additionally, it can be seen that $Y_{C_{12}H_{26}}$ has maximum value very close to the wall surface (i.e., $H = 0$), and a reaction zone representative of a diffusion flame similar to that in Fig. 4.12(a), is formed between the maximum values of $Y_{C_{12}H_{26}}$ and Y_{O_2} in their respective streamwise distributions. Once again, the blue bands in Figs. 4.13(a) and 4.13(b) indicate the height above the wall surface where the peak reaction rate $\dot{\omega}_C$ occurs. Even though the peak reaction rate in the near wall region is an order of magnitude smaller compared to that at the streamwise location of $x = 15$ mm [Fig. 4.12(a)], its presence alone indicates that chemical reactions are active in the vicinity of the wall surface. Such occurrences of heat release close to the wall surface will influence the velocity and thermal boundary layers, and the flow-field in the near wall region in general. Furthermore, in Fig. 4.13(b), a phenomenon is observed in the vicinity of the wall surface (indicated by the black rectangle very close to $H = 0$) in which, the mass fraction of CO_2 (Y_{CO_2}) increases towards the wall, while that of CO (Y_{CO}) decreases towards the wall. This is caused by the oxidation of CO into CO_2 according to the following exothermic reaction:

$$\mathrm{CO} + \frac{1}{2}\mathrm{O_2} \rightarrow \mathrm{CO_2} + 283\mathrm{kJ} \tag{4.44}$$

Occurrence of the above oxidation reaction can be attributed to the fact that, the reduction in gas-phase temperature T due to the wall heat loss, works in favor of this exothermic reaction to proceed (in order to mitigate the effect of wall heat loss based on Le Chatelier's principle). However, the amount of heat loss to the wall is considerably larger than the amount of heat generated by this exothermic reaction, due to which T near the wall surface decreases despite the progress of the above exothermic reaction.

To examine the behaviour of turbulence in the flow field, the instantaneous distributions of the gas-phase velocity magnitude in the central x-y plane, and the iso-surfaces of the second invariant of the velocity gradient tensor Q_2 are shown in Fig. 4.14 for Case

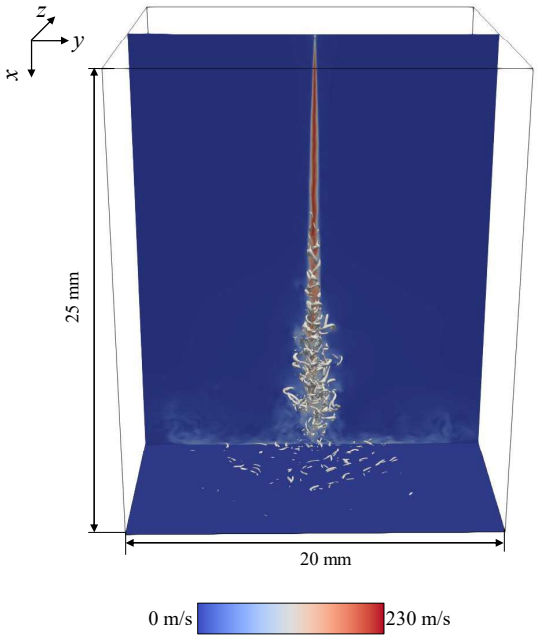

Figure 4.14: Instantaneous distributions of gas-phase velocity magnitude in the central x-y plane, and iso-surfaces of the second invariant of the velocity gradient tensor Q_2 for Case 3.

3. Here, Q_2 is defined as:

$$Q_2 = \frac{1}{2}\left[-S_{ij}S_{ij} + \left(-\frac{\partial u_i}{\partial x_i}\right)^2 + \omega_{ij}\omega_{ij}\right] \tag{4.45}$$

where, $\left(-\frac{\partial u_i}{\partial x_i}\right)$ is the 1$^{\text{st}}$ invariant, S_{ij} is the strain rate tensor and ω_{ij} is the rotation rate tensor. Q_2 represents the turbulent flow structure with $Q_2 > 0$ indicating the vorticity-dominated regions of the flow field, and $Q < 0$ indicating the strain rate-dominated regions. In Fig. 4.14, the iso-surfaces of Q_2 are shown for a positive value (i.e., $Q_2 > 0$), which implies that the turbulent structures in the vorticity-dominated regions are depicted. Initially, when the fuel spray is injected from the nozzle into the quiescent gas-phase, the momentum exchange occurring between the dispersed-phase fuel droplets and the gas-phase is responsible for imparting velocity to the gas-phase. From the gas-phase velocity magnitude distribution in Fig. 4.14, formation of the mixing layer between the spray jet axis and the ambient gas, which is caused by the velocity

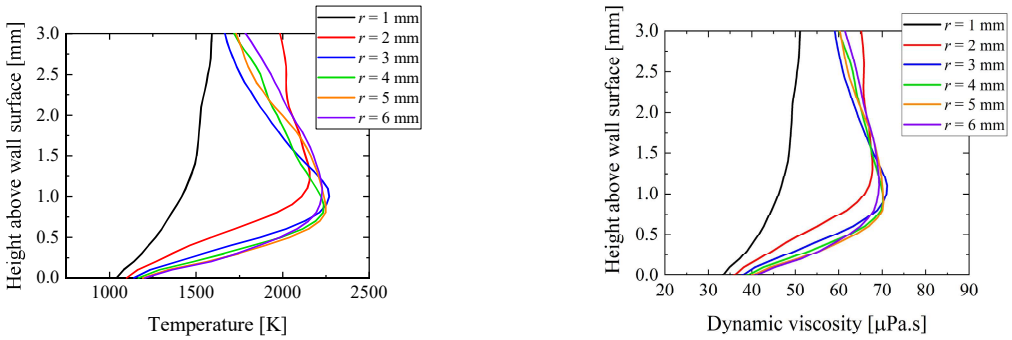

Figure 4.15: Streamwise distributions of time-averaged temperature and dynamic viscosity of gas-phase in the near wall region, at various radial locations for Case 3.

gradients between the spray jet and the quiescent ambient gas, is evident. After the spray flame collides with the wall surface, its mostly streamwise momentum (before collision) gets converted into momentum in the wall-parallel direction in the near-wall region.

The distribution of Q_2 iso-surfaces shows that turbulence is generated in the free shear layer (or mixing layer) of the spray jet flame, and develops in the downstream direction. However, turbulence starts decaying in the near wall region (with increasing radial distance from the spray jet axis in the wall-parallel direction) after the spray jet flame impinges on the wall surface, and spreads over the wall. The streamwise distributions of time-averaged gas-phase temperature and viscosity in the near wall region are plotted in Fig. 4.15, at various radial locations for Case 3. It is evident that with increasing radial distance from the spray jet axis ($r = 0$ mm), the gas-phase temperature increases and so does the viscosity, because viscosity is a temperature-dependent property. The gas-phase temperature increases with radial distance because chemical reactions are active in the vicinity of the wall surface (as already shown in Fig. 4.13), and progress as the radial distance from the spray jet axis increases. Therefore, as the viscosity becomes larger with increasing radial distance, it will play a major role in decaying the turbulence in the boundary layer formed on the wall surface. Furthermore, there is also evidence of turbulence decay brought about by chemical reactions (heat release) occurring in the vicinity of wall, from a previous DNS study on boundary layer

flashback in a turbulent channel flow [101], by our group.

4.3.1.2 Grid resolution requirements

As mentioned in Section 4.2, neither subgrid-scale turbulence model nor turbulence chemistry interaction model is employed in the present simulations of wall impinging spray flames. Computational grid used for the simulations of all the three cases is representative of that used for coarse DNS. At this stage, the grid resolution requirements are analysed for the simulation of Case 3, since the fuel injection velocity is highest in Case 3 among the three cases investigated in this study. Additionally, results of a grid sensitivity test conducted on Case 3 are also presented. Firstly, the Kolmogorov length scale η and the Kolmogorov time scale t_η are estimated as $\eta = (\nu^3/\epsilon)^{1/4}$, and $t_\eta = (\nu/\epsilon)^{1/2}$, where ν and ϵ are the mean kinematic viscosity and the mean dissipation rate of turbulent kinetic energy, respectively, at a given location in the flow-field. Evolutions of the computed Kolmogorov length scale η and Kolmogorov time scale t_η along the free shear layer of the spray jet flame in Case 3 are depicted in Fig. 4.16. It can be seen that, the size of the Kolmogorov length scale η gradually decreases with streamwise distance form the nozzle exit, due to increasing turbulence and lower temperatures in the central regions of the spray jet flame (caused by the latent heat of fuel droplet vaporization). However, η becomes nearly constant for $x > 18$ mm, and the Kolmogorov time scale t_η first decreases with streamwise distance form the nozzle exit and then increases slightly. The Kolmogorov length scales are smaller than the local grid size of $\Delta x = \Delta y = \Delta z = 40$ μm, but these grid sizes are a necessary trade-off when performing spray combustion simulations.

It should be emphasized that the present simulations have been considered in the context of turbulent spray combustion. When performing coarse DNS of turbulent spray combustion, the grid size should be capable of resolving the Kolmogorov length scales. But, at the same time, due to the two-way coupling strategy retained between the gas and dispersed phases using the PSI-Cell approach [72], the grid size must ideally be 10 times larger than the droplet size in order to accurately capture the droplet evaporation

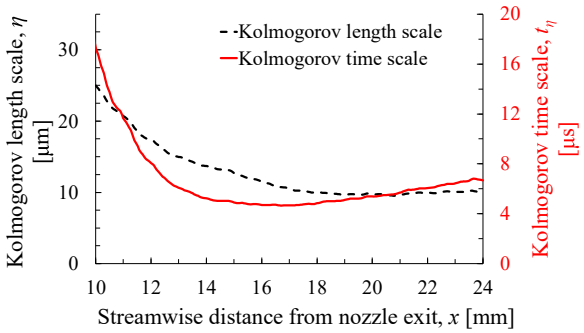

Figure 4.16: Evolutions of Kolmogorov length η and time t_η scales along the free shear layer of the spray jet flame in Case 3.

dynamics [73, 74]. For the present spray flame simulations to match the experiments, the fuel droplets are injected into the computational domain in a polydisperse manner using droplet size distribution PDFs (see Section 4.2.6), and the SMD of the injected fuel droplets ranges from 18.5 μm in Case 1 to 10.3 μm in Case 3. This puts a constraint on how small of a grid size can be used and hence, we have avoided using smaller grid sizes that are of the same order of the droplet diameters, in the core regions of the spray jet flame (for $x < 20$ mm) where majority of the fuel droplets are present. Otherwise, the predictions for droplet dynamics will be significantly erroneous. The wall-normal grid size Δx in the near wall regions becomes very fine, and can be of the order of droplet sizes or even smaller than the droplet sizes. The fuel droplets existing in those locations are treated using the Gaussian distance function technique explained in Section 4.2.2. This technique is computationally expensive and therefore, has been applied only in the near wall regions where Δx becomes equal to or smaller than twice the SMD of the injected fuel droplets.

Additionally, the radial distributions of η and t_η at various streamwise locations in the near wall region for Case 3, are presented in Fig. 4.17. In the central region of the spray jet flame, closer to the spray jet axis ($r = 0$ mm) where the temperatures are relatively low, and many fuel droplets exist, the Kolmogorov length scales η are smaller. However, η and t_η increase with radial distance from the spray jet axis at all streamwise locations, due to increasing temperature (caused by heat release from combustion). At

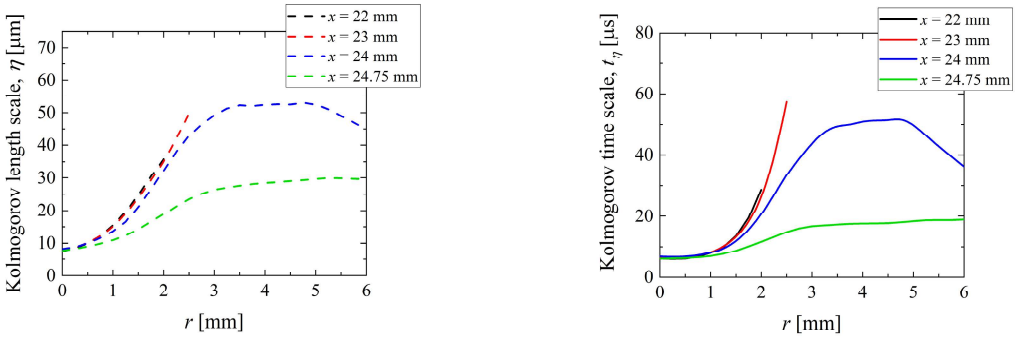

Figure 4.17: Radial distributions of Kolmogorov length η and time t_η scales, at various streamwise locations in the near wall region for Case 3.

Table 4.2: Various time scales encountered in the simulation of Case 3.

Time scales	Values
Injection time scale, $t_{inj} = D_n/u_{inj}$	0.384 μs
Minimum evaporation time scale, $\min(t_{evap} = \rho/S_\rho)$	$\approx$ 7 μs
Ignition delay time, τ_{id}	22.14 μs
Minimum Kolmogorov time scale, $\min(t_\eta)$	4.67 μs
Simulation time step value, Δt	$\approx$ 0.01 μs

the radial locations $r > 1$ mm, the grid sizes (Δx, Δy and Δz) are either less than or equal to twice the Kolmogorov length scale, which is often used in DNS of turbulent combustion [29, 102], and within the range recommended by Pope [103]. Therefore, resolution of the grid is adequate for performing the simulations of Cases 1 - 3. A summary of the various time scales encountered in the simulation of Case 3, such as injection time scale ($t_{inj} = D_n/u_{inj}$), minimum evaporation time scale ($t_{evap} = \rho/S_\rho$), ignition delay time (τ_{id}, discussed in detail later), minimum Kolmogorov time scale (t_η), and the time step value (Δt) used for time marching of the solution in the simulation of Case 3, are provided in Table 4.2. As evident from Table 4.2, the time step value Δt used in the simulation is sufficiently small to ensure accurate temporal resolution of all the relevant time scales.

Next, to check whether the grid resolution is adequate for resolving the velocity and

thermal boundary layers formed on the wall surface, results of a grid sensitivity test conducted on Case 3 are discussed. For this grid sensitivity test, another simulation was performed using the same conditions, computational domain configuration and fuel spray injection parameters as those in Case 3. But, the grid size Δx, in the wall normal x-direction is made much finer in the near wall region, i.e., for $x > 20$ mm (grid sizes in the y- and z-directions are kept the same). This finer grid simulation is designated as Case 3'. The simulation of Case 3' is performed using a Cartesian grid consisting of $840 \times 560 \times 560$ grid points in the x-, y- and z-directions, respectively, compared to $720 \times 560 \times 560$ grid points in the original Case 3. The minimum grid size in the x-direction $\Delta x_{min} = 0.93$ μm in Case 3' (compared to $\Delta x_{min} = 2.9$ μm in Case 3).

Figure 4.18 shows the comparisons between results computed in Case 3 and Case

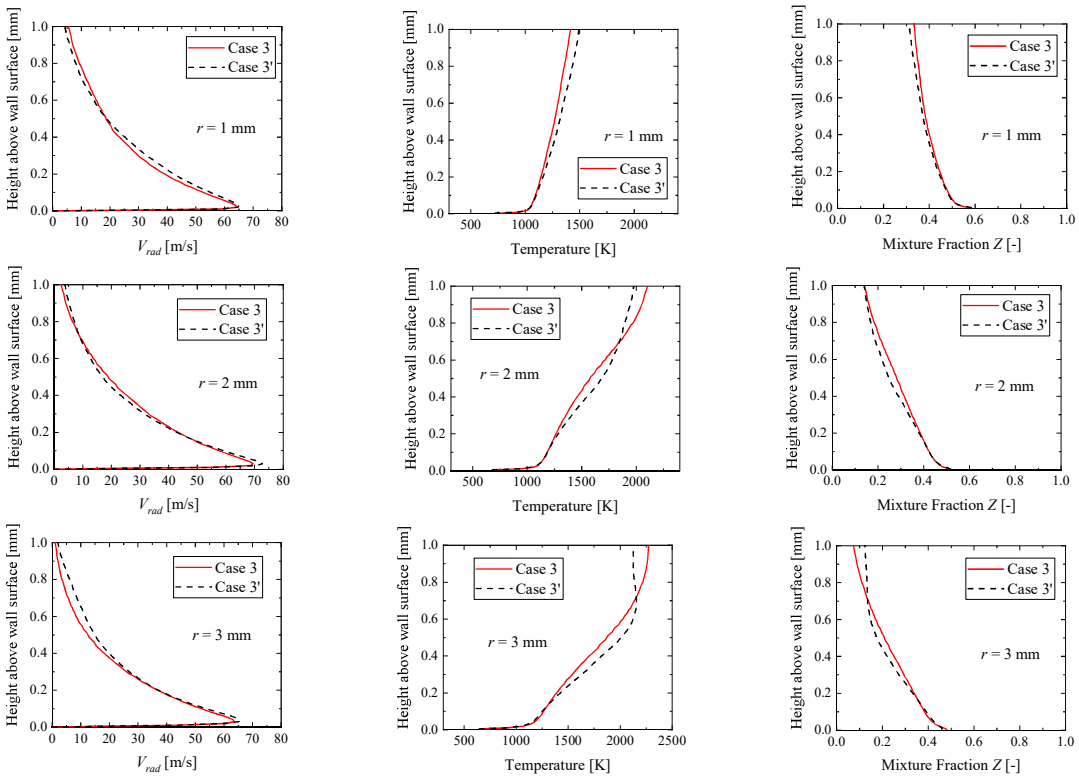

Figure 4.18: Comparisons of the streamwise distributions of mean radial velocity V_{rad} (wall-parallel component), mean temperature and mean mixture fraction close to the wall surface, at different radial locations between Case 3 and Case 3'.

3', for the streamwise profiles of mean wall-parallel radial velocity component V_{rad}, temperature and mixture fraction Z, close to the wall surface and at different radial locations (r = 1 mm, 2 mm and 3 mm) from the spray jet axis. The results do not show any drastic differences and are mostly similar between the original Case 3 and the finer grid Case 3'. There are some minor discrepancies though (especially in the temperature profiles), which are mainly due to the fact that the number of snapshots in time available for averaging in Case 3' were lesser than those in Case 3. The computational cost of simulating Case 3' was exorbitant, and we were able to perform the simulation of Case 3' for a physical time of 0.4 ms only, compared to 0.75 ms for Case 3. However, the results of Case 3 are nearly the same as those of Case 3', and hence, the resolution of the original grid of Case 3 is sufficient for the analysis presented in this study.

4.3.1.3 Comparisons with experiment

Results obtained from the simulation of Case 3 (u_{inj} = 216 m/s) are now compared with measurements obtained from an experiment conducted by Toyota Central R&D Labs., Inc., for the same conditions as that in Case 3's simulation, except for the fuel. Experimental data for the other two cases were unavailable due to proprietary reasons, so we are only able to show the comparisons for Case 3. Additionally, we would like to emphasize that the fuel used in the experiment was Diesel, while that used in the simulations is n-dodecane. Since data of the different hydrocarbon constituents of Diesel used in the experiment, and their exact proportions were unknown, n-dodecane has been chosen as the fuel for the simulations. Figure 4.19 illustrates the instantaneous distributions of computed soot radiation emission E_{soot} (line of sight integrated emissive power) for Case 3 at progressing time instances, along with the luminous flame photographs at the same time instances obtained from the experiment conducted by Toyota Central R&D Labs., Inc. Here E_{soot} is calculated as:

$$E_{soot} = \int_{-37.5\times10^{-3}}^{37.5\times10^{-3}} \kappa_{soot}\sigma T^4 dz \tag{4.46}$$

where κ_{soot} is the Planck mean absorption coefficient of soot and $\sigma = 5.669 \times 10^{-8}$ W/(m^{2}K^4) is the Stefan-Boltzmann constant. In the above Eq. 4.46, the term $\kappa_{soot}\sigma T^4$

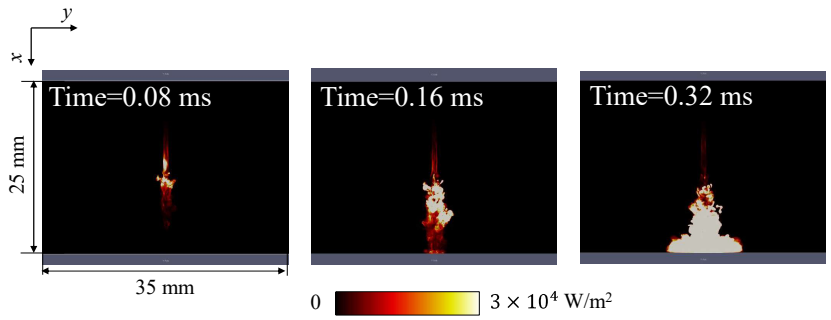

(a) Soot radiation emission (simulation)

(b) Luminous flame phtographs (experiment)

Figure 4.19: Comparison between (a) computed soot radiation emission distributions (line of sight integrated) of Case 3 in the x-y plane at different time instances, and (b) Luminous flame photographs of experiment [15] conducted by Toyota Central R&D Labs., Inc. at the same time instances.

represents the radiant power emitted by soot per unit volume, and E_{soot} is obtained by integrating this value in the z-direction, which implies that E_{soot} is the line of sight integrated soot emissive power. The brightness of the luminous flame in the experimental flame photographs, can be considered to be proportional to the soot emissive power E_{soot}, however, it is not an accurate representation of the flame's radiant power. Therefore, the comparison shown in Fig. 4.19 is for qualitative purpose only. From the figure, it can be confirmed that after the evaporated fuel auto-ignites, combustion occurs and then the spray flame impinges on the wall. Additionally, the distributions of computed soot emissive power E_{soot} show reasonable qualitative agreement with the experimental luminous flame photographs, in terms of the temporal evolution of the flame and its

brightness caused by the soot radiation emission.

Quantitative comparisons are also performed between the simulation and experiment as shown in Fig. 4.20. In Fig. 4.20(a), the time variation of temperature at the stagnation point O on the wall surface (point on the wall surface where the spray jet flame impinges directly, also refer Fig. 4.4), obtained from the simulation of Case 3 is compared with experimental data. The simulation result shows an overall good agreement with measurements, however, the stagnation point temperature is slightly under-predicted by the simulation for time after start of injection (ASOI) greater than 0.6 ms. Similar comparison is performed between the computed and measured time variations of wall heat flux at the stagnation point as shown in Fig. 4.20(b). The simulation result shows features similar to that of the experiment, like the initial steep rise of the wall heat flux when the spray flame comes in contact with the stagnation point, followed by the wall heat flux getting stabilized and becoming nearly constant in time. In this sense, the simulation is able to capture the time variation trends of the stagnation point's wall heat flux reasonably well. However, the simulation under-predicts the wall heat flux for time ASOI greater than 0.5 ms. This is a direct consequence of the under-predicted

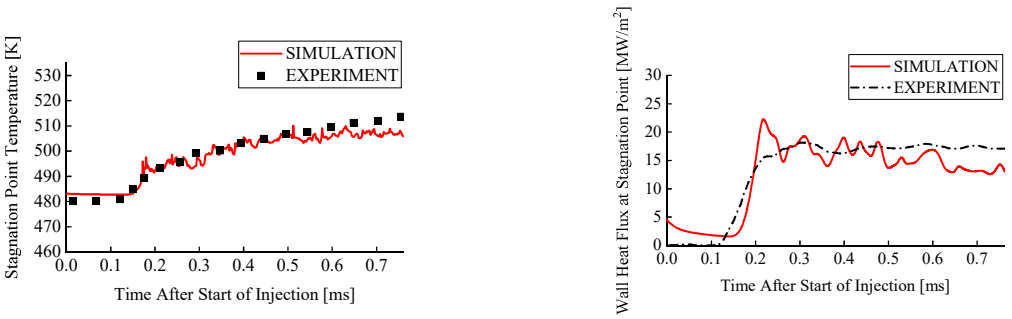

(a) Stagnation point temperature

(b) Wall heat flux at stagnation point

Figure 4.20: Comparisons of the time variations of (a) temperature of the stagnation point on wall surface, and (b) total wall heat flux at the stagnation point in Case 3, with experimental measurements [16] made by Toyota Central R&D Labs., Inc.

temperature in Fig. 4.20(a), because the wall heat flux result of the simulation in Fig. 4.20(b), has been computed using the wall-side temperature gradient at the wall surface (i.e., by applying Fourier's law of heat conduction). The most likely reasons for the discrepancies in the results of the stagnation point's temperature and wall heat flux in Fig. 4.20 are as follows:

1. As mentioned earlier, the fuel used in the simulations is n-dodecane while that used in the experiment is Diesel (a blend of various hydrocarbons). Hence, relevant fuel vapour properties such as density, thermal conductivity, specific heat capacities, viscosity, calorific value, etc. are different, and are bound to influence the results. Thermophysical properties and transport coefficients of the fuel droplets and the liquid fuel film formed on the wall surface, will also be different from that of Diesel.

2. In Fig. 4.20(b), it can be seen that the stagnation point's wall heat flux in the experiment is zero at time ASOI = 0, but that in the simulation is non-zero at time ASOI = 0. This is because in the simulation, the initial gas-phase temperature is set to be 1600 K uniformly throughout the computational domain, and the initial temperature distribution inside the wall is assumed to vary linearly from 481 K at the top surface to 463 K at the bottom surface (refer Section 4.2.6). However, at time ASOI = 0 in the experiment, the gas-phase temperature in the near wall regions might not have been 1600 K, and the temperature profile inside the wall might not necessarily be linear. Since detailed descriptions of the initial spatial distribution of gas-phase temperature in the near wall region, and the initial temperature distribution in the wall are unknown from the experiment, the aforementioned assumptions had to be made for the initial conditions in the simulations. As these initial conditions will also dictate how the solution evolves over time, they constitute another source of the discrepancies in Fig. 4.20.

Next, the ignition delay time obtained from the simulation is compared with the measured value. In the simulation, ignition delay time τ_{id} is defined as the time after start of fuel injection to the time when the maximum rate of maximum temperature rise

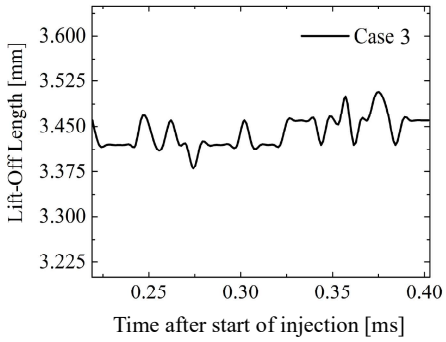

Figure 4.21: Time variation of the flame lift-off length obtained from the simulation of Case 3.

occurs in the domain, i.e., the following mathematical expression:

$$\tau_{id} = \tau_{\left(\frac{dT_{max}}{dt}\right)_{max}} - \tau_{SOI} \tag{4.47}$$

where τ_{SOI} is the time at start of injection (SOI) and for the present simulation $\tau_{SOI} = 0$, and T_{max} is the maximum gas-phase temperature in the combustion field, i.e. $T_{max}(t) = \max(T(x, y, z, t))$. The ignition delay time τ_{id} computed for Case 3 is 22.14 μs ($\tau_{id} = 34.9$ μs for Case 1, and $\tau_{id} = 26.43$ μs for Case 2), while τ_{id} measured in the experiment is 60 μs (data provided by Toyota Central R&D Labs., Inc.). The simulation of Case 3 yields faster ignition of the evaporated fuel compared to the experiment, since the NA-FPV approach is used as the combustion model. Although the NA-FPV approach is unable to accurately reproduce τ_{id} of spray combustion, the predicted ignition delay time (22.14 μs) is of the same order of magnitude as that of the experiment (60 μs). Moreover, the main objective of this study is to analyze the wall heat transfer characteristics when spray flames impinge on a wall, so in this context the NA-FPV approach is adequate. Another plausible reason as to why the simulation yields shorter ignition delay time, is the assumption that a spray is already established at the nozzle exit (whose size distribution is given by fitting the measured data with a Rosin-Rammler PDF, see Section 4.2.6). In other words, the atomization process at the nozzle exit is assumed to be instantaneous and its time scale is not considered in the simulation.

Figure 4.21 depicts the computed time variation of the flame lift-off length in Case

3. In the simulation, flame lift-off length (LOL) is defined as the streamwise distance from the spray nozzle exit to the location of 14% of the maximum OH radical mass fraction corresponding to the quasi-steady state [44]. From the result in Fig. 4.21, the quasi-steady LOL is calculated, which comes out to be approximately 3.441 mm. The predicted flame lift-off length is in close agreement with the experimental value of 4.4 mm (data provided by Toyota Central R&D Labs., Inc.), although it's slightly under-predicted. Such an under-prediction is attributed to the limitations of the applied combustion model, i.e., the NA-FPV approach. This flame LOL analysis is presented nonetheless, to check how close the prediction is to the experimental value.

4.3.2 Wall heat flux

4.3.2.1 Dependence of total wall heat flux on fuel spray injection velocity

Temporal variations of the total wall heat flux at different radial locations on the wall surface from the stagnation point O (i.e., r = 0, 2, 4, 6, 8 and 10 mm), are presented in Fig. 4.22 for all the three cases. Here, the radial location of r = 0 mm on the wall surface corresponds to the stagnation point O (refer Fig. 4.4). Total wall heat flux is the sum of the convective and radiative heat fluxes at the wall surface, and the injected fuel mass is representative of time. From Figs. 4.22(a) to (d), it can be seen that at the radial locations of r = 0, 2, 4 and 6 mm on the wall surface, the total wall heat flux increases rapidly after the flame reaches the respective radial locations in each case. Thereafter, the total wall heat flux gradually approaches a quasi-steady state and becomes roughly constant in each case. The general trend observed from this figure is that, at any given radial location, the total heat flux is larger for the case with the higher fuel injection velocity. At the radial location of r = 8 mm in Fig. 4.22(e), the total wall heat flux has not yet reached a steady value in any of the cases. On the other hand, as evident from Fig. 4.22(f), the flames are yet to arrive at the radial location of r = 10 mm in all the three cases, which is why the total heat flux has not increased in any of them. Therefore, in the following, wall heat fluxes (total, convective and radiative heat fluxes)

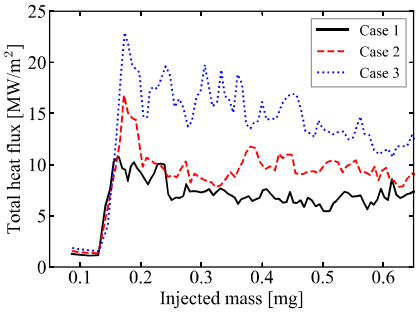

(a) $r = 0$ mm

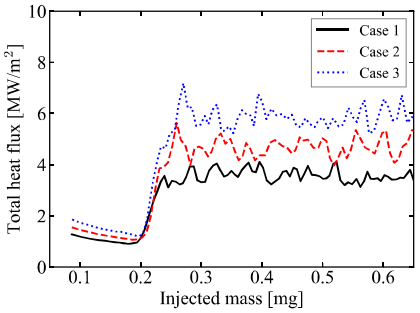

(b) $r = 2$ mm

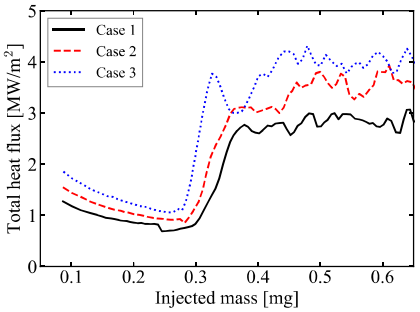

(c) $r = 4$ mm

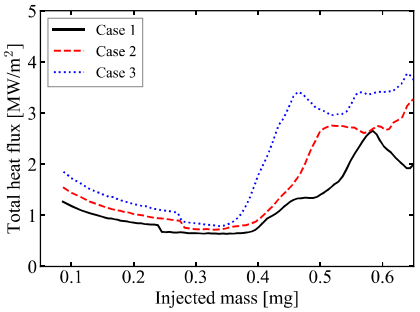

(d) $r = 6$ mm

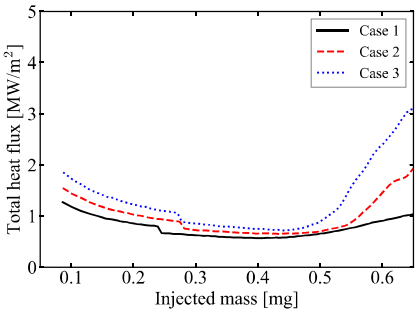

(e) $r = 8$ mm

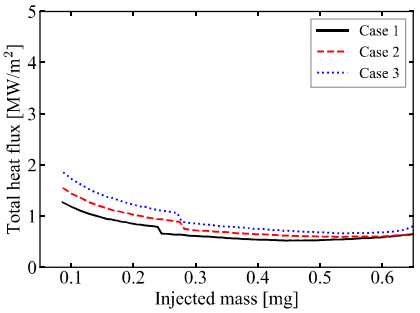

(f) $r = 10$ mm

Figure 4.22: Time variations of total heat flux at the wall surface at different radial locations for each case. Here, injected mass of fuel is representative of time.

in the region corresponding to 0 mm $\leq r \leq$ 6 mm are discussed.

Radial distributions of time-averaged total heat flux (quasi-steady condition) at the

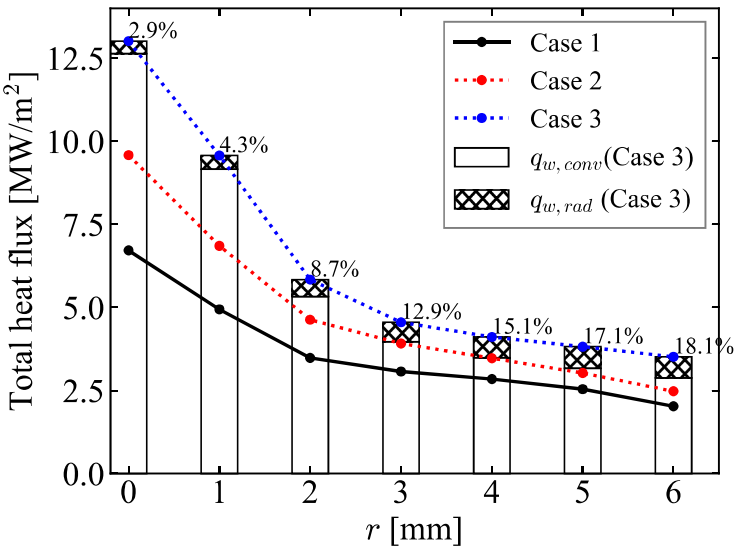

Figure 4.23: Radial distributions of time-averaged total heat flux at the wall surface for all three cases, with the stacked column bar graph showing the contributions of convective heat flux $q_{w,conv}$ and radiative heat flux $q_{w,rad}$ to the total heat flux in Case 3. The percentages above the stacked columns for the different radial locations on the wall surface, indicate the ratio of radiative heat flux to total heat flux at the respective radial locations in Case 3.

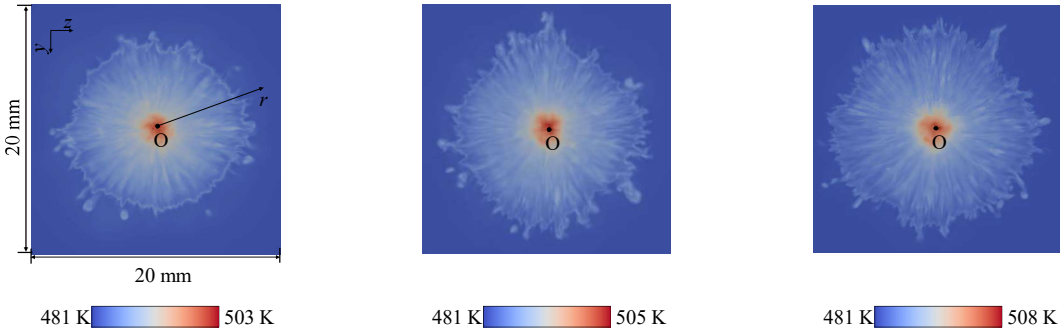

(a) Case 1 ($u_{inj} = 100$ m/s) (b) Case 2 ($u_{inj} = 150$ m/s) (c) Case 3 ($u_{inj} = 216$ m/s)

Figure 4.24: Instantaneous distributions of wall surface temperature in the y-z plane for each case, at the time instance when injected fuel mass $m_{inj} = 0.64$ mg.

wall surface are presented in Fig. 4.23 for all the three cases. Here, time-averaging of the total heat flux at a given radial location, is performed after the total heat flux reaches a roughly steady value at that particular radial location, as mentioned previously for Fig. 4.22. Additionally, to analyze the individual contributions of the convective $q_{w,conv}$ and radiative $q_{w,rad}$ heat fluxes to the total wall heat flux, breakdown of the total heat flux at various radial locations are shown in Fig. 4.23 for Case 3, in the form of a stacked column bar graph. The percentage above each stacked column represents the ratio of the radiative heat flux to the total heat flux, at the respective radial location on the wall surface in Case 3. The other two cases exhibited similar qualitative trends, in terms of the radial distributions of the contributions from $q_{w,conv}$ and $q_{w,rad}$ to the total wall heat flux, and hence breakdowns of the total heat flux in Cases 1 and 2 are not shown here. From Fig. 4.23, it is found that the total wall heat flux is maximum at the stagnation point O ($r = 0$ mm), and decreases with increasing radial distance form the stagnation point in all the cases. Furthermore, with increasing fuel injection velocity u_{inj}, a marked increase in the total wall heat flux is observed. This is why at any given radial location on the wall surface, the total heat flux in Case 3 ($u_{inj} = 216$ m/s) is the largest, followed by the total heat flux in Case 2 ($u_{inj} = 150$ m/s), and then the total heat flux in Case 1 ($u_{inj} = 100$ m/s) which has the smallest value. The instantaneous distributions of wall surface temperature at the time instance corresponding to injected fuel mass $m_{inj} = 0.64$ mg in each case, are depicted in Fig. 4.24. In each case, it can be seen that the temperature at and around the vicinity of the stagnation point O is the highest, and it decreases with increasing radial distance. Moreover, the higher the fuel injection velocity, the higher the wall surface temperature. Thus, the wall surface temperature trends are consistent with those of the total wall heat flux in Fig. 4.23.

Since the total heat flux is expressed as the sum of the convective and radiative heat fluxes, the features of radiative heat flux in Case 3 shown in Fig. 4.23 are analyzed next. It is observed that the radiative heat flux accounts for a small fraction (2.9%) of the total wall heat flux at the stagnation point, but the magnitude of the radiative heat flux as well as its contribution to the total wall heat flux, increase with radial distance from the

stagnation point ($r = 0$ mm). The same features were observed for the radiative heat flux in Cases 1 and 2, and the differences among the three cases are only quantitative. To understand why the radial distribution of radiative heat flux exhibits a trend opposite to that of the total heat flux, the streamwise distributions (i.e., variations with height above the wall surface) of spatially averaged gas-phase temperature at different radial locations of $r = 0$ mm and $r = 6$ mm, are analyzed in Fig. 4.25. Spatial averaging of temperature in this figure bears the same meaning as the spatial averaging of the quantities presented in Figs. 4.12 and 4.13. From Fig. 4.25, it is evident that in each case, the gas-phase temperature in the near wall region is higher at the radial location of $r = 6$ mm, compared to the radial location of $r = 0$ mm (i.e., above the stagnation point). This happens because, combustion reaction progresses as the radial distance from the spray jet axis increases, due to the availability of vaporized fuel that gets convected from the central region of the spray jet flame, to the radial locations farther away from the spray axis ($r = 0$ mm) in the wall-parallel direction, as seen in Fig. 4.13. Consequently, the radiation intensity and hence, the radiative heat flux are smaller at the stagnation point, and the radiative heat flux at the wall surface becomes larger with increasing radial distance from the stagnation point. However, the major contribution to the total wall heat flux comes from the convective heat flux rather than the radiative

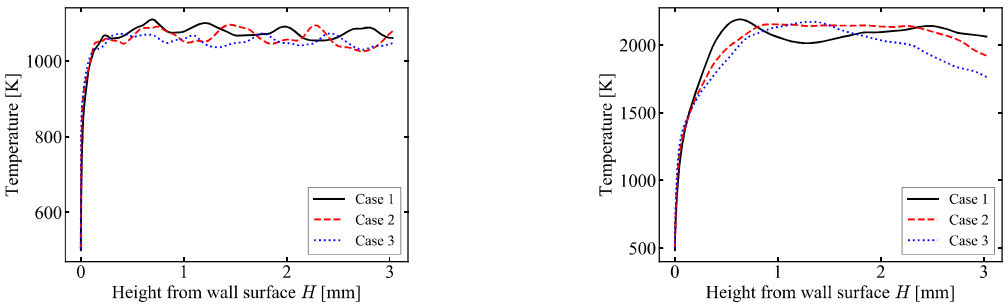

(a) $r = 0$ mm (b) $r = 6$ mm

Figure 4.25: Streamwise distributions of spatially averaged temperature at different radial locations of (a) $r = 0$ mm and (b) $r = 6$ mm, for each case at the time instance when injected fuel mass $m_{inj} = 0.64$ mg.

heat flux, so the features of convective heat flux are examined next.

4.3.2.2 Dependence of convective heat flux on fuel spray injection velocity

Figure 4.26 depicts the time variations of convective heat flux $q_{w,conv}$ at the radial locations of r = 0, 2, 4, 6, 8 and 10 mm on the wall surface, for all the three cases. The temporal variation trends of $q_{w,conv}$ are the same as those of the total wall heat flux observed in Fig. 4.22, such as, at the radial locations of r = 0, 2, 4 and 6 mm, the convective heat flux rises rapidly after the flame arrives at the respective radial locations, and subsequently attains a roughly steady value in each case. Furthermore, at any given radial location, the convective heat flux is largest in Case 3 (u_{inj} = 216 m/s) followed by Case 2 (u_{inj} = 150 m/s) and then Case 1 (u_{inj} = 100 m/s), which is similar to observation made in Fig. 4.22 for the total wall heat flux. As with the total heat flux, the convective heat flux in all the cases is yet to reach steady values at the radial location of r = 8 mm, as depicted in Fig. 4.26(e). Similarly, as shown in Fig. 4.26(f), the convective heat flux has not increased in any of the cases at r = 10 mm, because the flames have not yet reached this radial location. Hence, the following discussion pertains to convective heat flux at the wall surface, in the region corresponding to r = 0 mm $\sim$ 6 mm.

Analyzing the radial distributions of time-averaged convective heat flux (quasi-steady condition) at the wall surface for all the three cases in Fig. 4.27, in the same manner as those of the time-averaged total heat flux in Fig. 4.23, the exact same trends can be seen to emerge. The convective heat flux is largest at the stagnation point O and reduces with increasing radial distance from the stagnation point, in each case. Comparing the convective heat flux at any given radial location on the wall surface among the three cases, it is clear that the higher the fuel injection velocity u_{inj}, the larger the convective heat flux. Therefore, the reason as to why the total wall heat flux exhibits characteristics similar to those of the convective heat flux is that, the contribution of convective heat flux to the total wall heat flux is dominant compared to that of the radiative heat flux.

Next, the reason for the radial distribution trend of convective heat flux at the wall

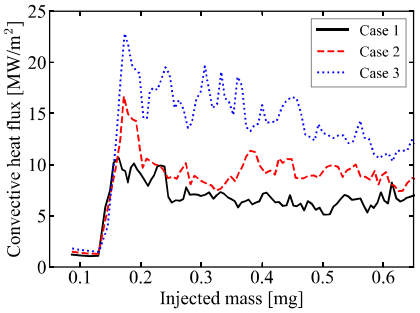

(a) $r = 0$ mm

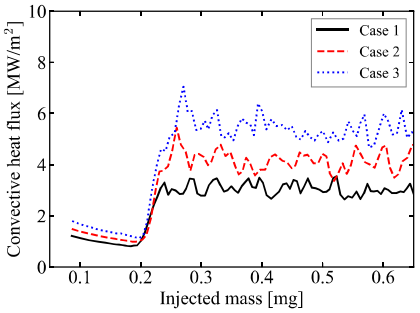

(b) $r = 2$ mm

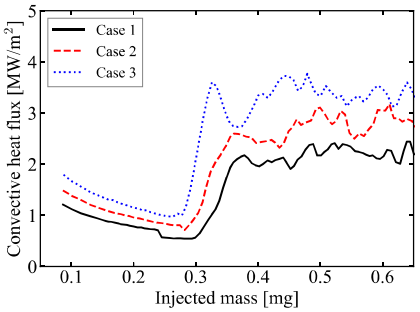

(c) $r = 4$ mm

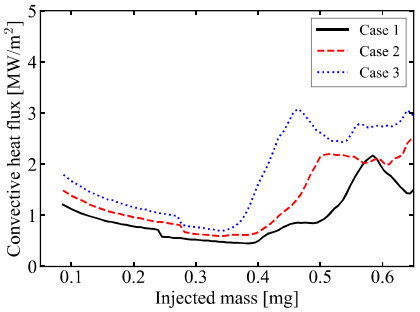

(d) $r = 6$ mm

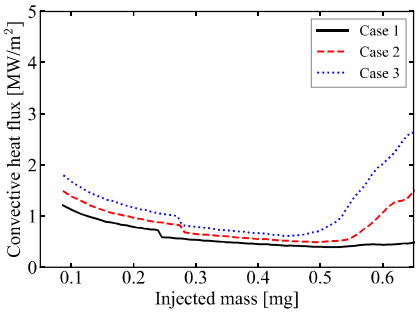

(e) $r = 8$ mm

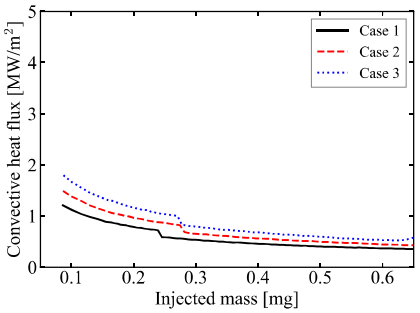

(f) $r = 10$ mm

Figure 4.26: Time variations of convective heat flux at the wall surface at different radial locations for each case. Here, injected mass of fuel is representative of time.

surface, and the reason for the increase in convective heat flux with increasing fuel spray injection velocity are investigated. The wall-normal turbulent heat flux arises from the

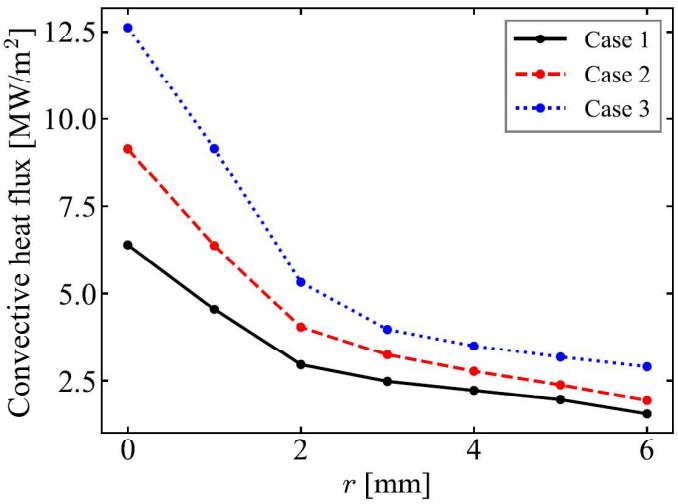

Figure 4.27: Radial distributions of time-averaged convective heat flux at the wall surface for all three cases.

activation of turbulent heat transport in the wall-normal direction by coherent vortical structures near the wall surface [104]. Therefore, an intuitive way to understand the role of turbulent heat transport in promoting the convective heat flux, is to analyze the sweep and ejection events close to the wall surface. Firstly, to understand the dependence of convective heat flux on the fuel injection velocity, the joint probability density function (PDF) distributions of temperature fluctuation T' and the wall-normal (x-direction) component of velocity fluctuation u', close to the wall surface above the stagnation point (i.e., at $r = 0$mm) are illustrated in Fig. 4.28 for all the three cases. The first quadrant of this joint PDF distribution marked by the red square in Fig. 4.28(c) corresponds to sweep, and the third quadrant marked by the green square corresponds to ejection. Sweep is the wallward interaction motion that supplies hot gas to the vicinity of the wall surface (i.e., when $u' > 0$ and $T' > 0$), and ejection represents the roll-up motion that causes the relatively cold gas in the vicinity of the wall surface to get entrained away from the wall surface (i.e., when $u' < 0$ and $T' < 0$). From Fig. 4.28, it is clear that the higher the fuel injection velocity u_{inj}, the stronger the correlation between u' and T'. A stronger correlation between u' and T' indicates larger contributions of the sweeps and

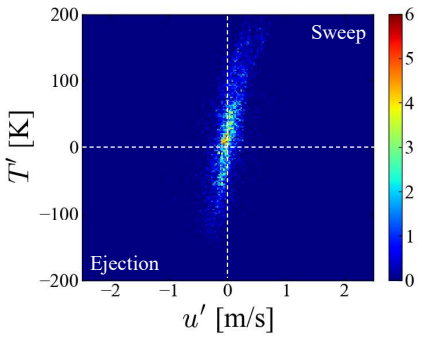

(a) Case 1, $u_{inj} = 100$ m/s ($r = 0$ mm)

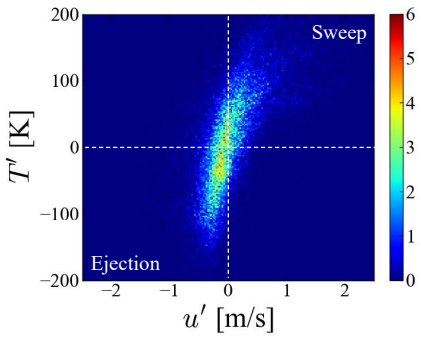

(b) Case 2, $u_{inj} = 150$ m/s ($r = 0$ mm)

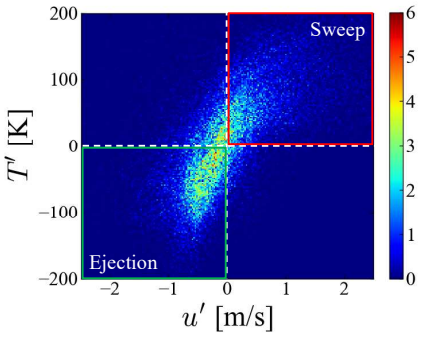

(c) Case 3, $u_{inj} = 216$ m/s ($r = 0$ mm)

Figure 4.28: Joint probability density function distributions of wall-normal component of velocity fluctuation u' and temperature fluctuation T' for (a) Case 1 ($u_{inj} = 100$ m/s), (b) Case 2 ($u_{inj} = 150$ m/s) and (c) Case 3 ($u_{inj} = 216$ m/s), at the radial location of $r = 0$ mm (above the stagnation point O).

ejections to the turbulent heat transport in the wall-normal direction, which results in the enhancement of convective heat flux.

Next, to understand why the convective heat flux is maximum at the stagnation point and decreases with increasing radial distance from the stagnation point, Fig. 4.29 shows the joint PDF distributions of u' and T' close to the wall surface at different radial locations of $r = 0$ mm, 3 mm and 6mm, for Case 3. From the figure, it is evident that the correlation between u' and T' is the strongest at $r = 0$ mm, i.e., above the stagnation point O, and this correlation becomes weaker with increasing radial distance from the nozzle axis ($r = 0$ mm). Therefore, wall-normal turbulent heat flux is greatly enhanced

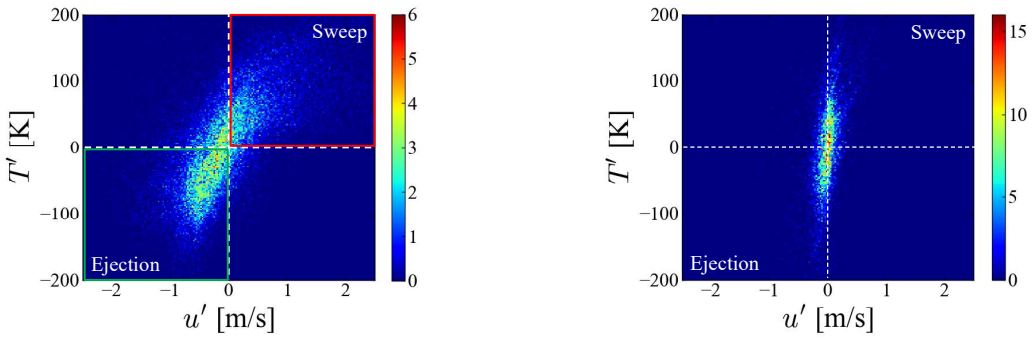

(a) $r = 0$ mm (Case 3)

(b) $r = 3$ mm (Case 3)

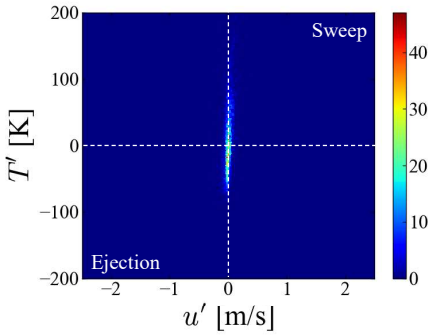

(c) $r = 6$ mm (Case 3)

Figure 4.29: Joint probability density function distributions of wall-normal component of velocity fluctuation u' and temperature fluctuation T', at different radial locations of (a) $r = 0$ mm, (b) $r = 3$ mm and (c) $r = 6$ mm for Case 3 ($u_{inj} = 216$ m/s).

in the vicinity of the stagnation point, due to the largest contributions of sweeps and ejections to the wall-normal turbulent heat transport. This is the reason as to why the convective heat flux is maximum at the stagnation point, and decreases with increasing radial distance from the stagnation point.

4.3.3 Wall heat flow rate

Description of the wall heat flow rate Q_w for all the three case is now presented. Wall heat flow rate Q_w is defined as the amount of thermal energy or heat being transferred to the wall per unit time, and is calculated by integrating the wall heat flux over the

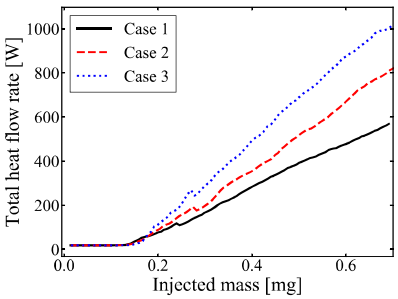

(a) Total heat flow rate

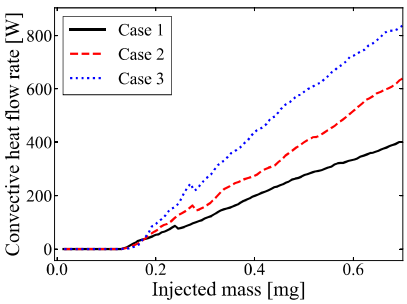

(b) Convective heat flow rate

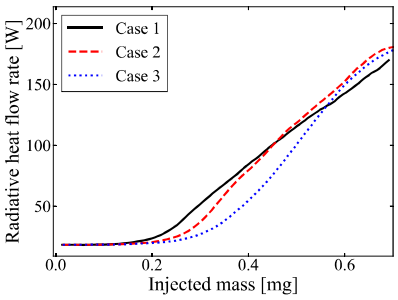

(c) Radiative heat flow rate

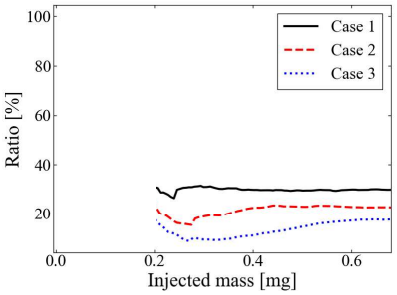

(d) Ratio

Figure 4.30: Time variations of (a) total heat flow rate, (b) convective heat flow rate, (c) radiative heat flow rate, and (d) ratio of radiative heat flow rate to total heat flow rate. Here, injected mass of fuel is representative of time.

wall surface area A through which heat transfer occurs, as follows:

$$Q_w = \int_A q_w dA \tag{4.48}$$

4.3.3.1 Dependence of wall heat flow rate on fuel injection velocity

Figure 4.30 depicts the temporal variations of total heat flow rate, convective heat flow rate, radiative heat flow rate, and the ratio of radiative heat flow rate to total heat flow rate at the wall surface. Here, total heat flow rate is simply the sum of convective and radiative heat flow rates. In Fig. 4.30(d), the ratio of radiative heat flow rate to total heat flow rate is shown only for the time after the spray flame impinges on the wall surface, and the convective and total heat flow rates begin to increase in each case. In terms of the injected fuel mass m_{inj}, the time around which these heat flow rates begin

to increase roughly corresponds to $m_{inj} = 0.2$ mg. From Fig. 4.30, it can be seen that the total, convective and radiative heat flow rates increase steadily with time in all the three cases, because once the flame has impinged on the wall surface, the flame and the hot gas mixture begin to propagate in the wall-parallel direction with time, thereby increasing the wall surface area through which heat loss occurs in each case. Comparing the total and convective heat flow rates in Figs. 4.30(a) and 4.30(b), respectively, among the three cases at any given time instance, Case 3 ($u_{inj} = 216$ m/s) exhibits the highest values of these heat flow rates followed by Case 2 ($u_{inj} = 150$ m/s), and then Case 1 ($u_{inj} = 100$ m/s) which has the lowest values of these heat flow rates. On the other hand, the radiative heat flow rates of all the three cases shown in Fig. 4.30(c) are not significantly different from one another, and approach nearly the same value with time. Consequently, the ratio of radiative heat flow rate to total heat flow rate in each case, shown in Fig. 4.30(d) becomes roughly constant with time, with Case 1 having the highest ratio followed by Case 2 and then Case 3.

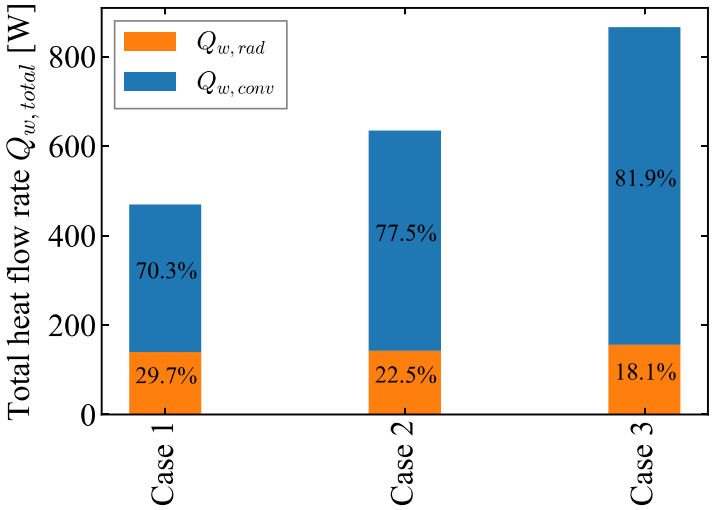

Figure 4.31: Total heat flow rate ($Q_{w,total}$) and its contributions from radiative ($Q_{w,rad}$) and convective ($Q_{w,conv}$) heat flow rates, at the time instance when injected fuel mass $m_{inj} = 0.64$ mg in each case. The percentages in each stacked column indicate the ratios of radiative and convective heat flow rates to total heat flow rate.

Figure 4.31 shows the breakdown of the total heat flow rate $Q_{w,total}$ in terms of its contributions from the convective $Q_{w,conv}$ and radiative $Q_{w,rad}$ heat flow rates for all the three cases, at the time instance when the injected fuel mass $m_{inj} = 0.64$ mg in each case. It is evident that, the higher the fuel injection velocity, the larger the total and convective heat flow rates through the wall surface. In Section 4.3.2.2, the influence of fuel injection velocity on the convective heat flux at the wall surface was discussed, and it was found that the convective heat flux increases with increasing fuel injection velocity. As shown in Fig. 4.31, the convective heat flow rate accounts for about 70% $\sim$ 82% of the total heat flow rate (depending on the case), while the contribution of radiative heat flow rate to the total heat flow rate remains nearly the same in all the three cases (magnitude-wise). Therefore, the total heat flow rate also increases with increasing fuel injection velocity.

On the contrary, the influence of fuel injection velocity on the radiative heat flow rate seems rather insignificant from Fig. 4.31. This is due to the fact that, the fuel injection velocity does not have an appreciable influence on the flame/gas-phase temperature, as shown previously in Fig. 4.25, and thus, the intensity of radiation emitted by soot and the gas-phase species does not change significantly among the three cases. Consequently, the ratio of radiative heat flow rate to total heat flow rate is larger when the fuel injection velocity is smaller. In the present simulations, this ratio lies in the range of 18.1% (for Case 3) to 29.7% (for Case 1), which is in good agreement with the values measured in previous experiments [105, 106].

4.3.3.2 Correlation between Nu and Re

The relation between Nusselt number Nu and Reynolds number Re corresponding to heat loss at the wall surface, during spray flame-wall interaction is now examined. In an attempt to estimate the heat loss through the walls of IC engines, previous experimental studies [7–12, 15–17] have investigated the relation between Nu and Re based on the principle of convective heat transfer, under the assumptions of quasi-steady conditions and a constant Prandtl number. These investigations led to the development of empiri-

cal correlations for calculating the heat transfer coefficient, and showed that Nu has a power law dependence on Re as expressed in Eq. (4.1). The present simulations mimic the phenomenon of spray flames impinging on a wall under CI engine-like conditions, occurring during the combustion period of a CI engine. It should be noted that the correlation shown in Eq. (4.1), is applicable for pure convection heat transfer problems and not for situations in which radiative heat transfer is also involved, because strictly speaking, the Nusselt number Nu is a parameter that provides a measure of the convection heat transfer occurring at a surface, and radiation heat transfer is not a function of Re. However, in the experiments, the measured wall heat flux might implicitly include the contribution of radiation heat transfer. Furthermore, as described in Section 4.3.3.1, the contribution of radiative heat flow rate to the total heat flow rate at the wall surface varies from 18.1% to 29.7% (depending on the case), and as also pointed out by some previous experimental studies [18, 105, 106], such contributions from the radiation heat transfer certainly cannot be neglected.

Therefore, in the following, two types of Nusselt number are defined and their dependence on Re is analyzed. The first Nusselt number Nu_{total} is calculated based on the average total heat flux at the wall surface (i.e, convective heat flux + radiative heat flux) in the quasi-steady state, while the second Nusselt number Nu_{conv} is calculated based on the average convective heat flux in the quasi-steady state (i.e., the conventional definition). These two Nusselt numbers and the Reynolds number Re are expressed as:

$$Nu_{total} = \frac{h_{heat} H}{\lambda} = \frac{q_{w,total}}{T - T_w} \frac{H}{\lambda} \tag{4.49}$$

$$Nu_{conv} = \frac{h_{heat} H}{\lambda} = \frac{q_{w,conv}}{T - T_w} \frac{H}{\lambda} \tag{4.50}$$

$$Re = \frac{\rho U H}{\mu} \tag{4.51}$$

where h_{heat} is the average heat transfer coefficient, H is the characteristic length, T is the average gas-phase temperature (in quasi-steady state) in the near wall region and is used as the characteristic temperature, T_w is the wall temperature, $q_{w,total}$ and $q_{w,conv}$ are the average total wall heat flux and convective heat flux (in quasi-steady

state), respectively, U is the characteristic velocity, and ρ, μ and λ are the gas-phase density, dynamic viscosity and thermal conductivity, respectively. Following previous experiments [16, 17], the characteristic length H used in Eqs. (4.49) - (4.51) is set equal to the spray impingement distance value of 0.025 m (i.e., the distance from the spray nozzle exit to the wall surface) in this study. In the previous experiments [16, 17], the local gas-phase velocity and thermophysical properties such as ρ, μ and λ could not be measured directly. Hence, values of the thermophysical properties corresponding to either air [17] or the ambient conditions [16] were used to calculate Nu and Re. To get an estimate for the characteristic flow velocity U, Mahmud et al. [17] used the waveform signals of wall heat flux measured by the thermocouple heat flux sensors embedded in the flat wall. On the other hand, Inagaki et al. [16] used the flame snapshots in the near wall region at different time instances (obtained from high-speed imaging) to estimate U. However, in this study, the maximum value of average radial velocity (wall-parallel component) in the velocity boundary layer is chosen for the characteristic velocity U in Eq. (4.51). λ in Eqs. (4.49) and (4.50) is the average gas-phase thermal conductivity at the wall surface.

Furthermore, for the present analysis, the values of gas-phase density ρ, dynamic viscosity μ and characteristic temperature T are obtained by temporal and spatial averaging. Here, spatial averaging implies averaging over a cylindrical volume of radius $r = 6$ mm, with the axis of this imaginary cylinder being coaxial with the spray nozzle axis. Different values for the height of this imaginary cylinder in the wall-normal x-direction (starting from the wall surface) are used for the spatial averaging of these quantities, such as 0.5 mm, 1 mm, 2 mm and 3 mm. This is done in order to check the dependence of Nu - Re correlations, on the height of the imaginary cylinder used for the spatial averaging of ρ, μ and T, since some of these quantities (ρ, μ and λ) are defined differently in the previous experimental studies [16, 17], as mentioned above. However, in this study, complete descriptions of the spatial and temporal variations of all the quantities are readily available from the simulation results, hence temporal and spatial averaging of the relevant quantities can be performed in the near wall regions of interest, and used

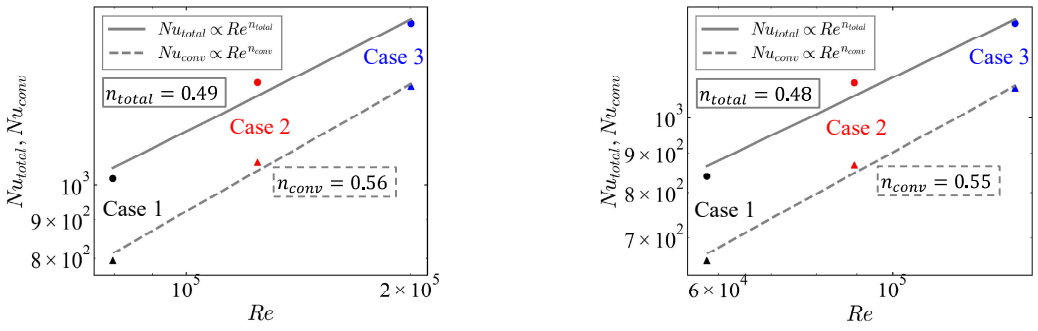

(a) 0.5 mm

(b) 1 mm

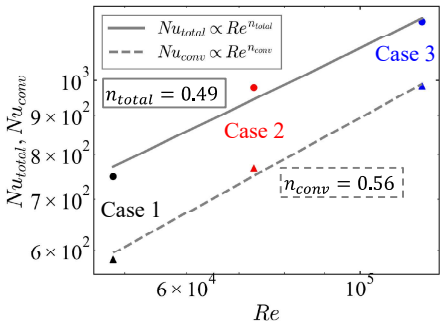

(c) 2 mm

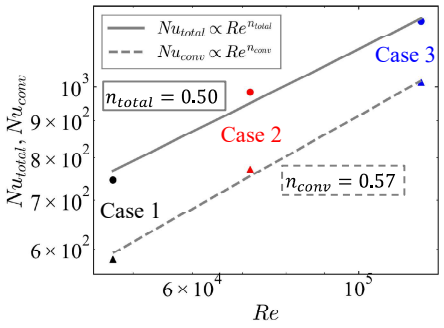

(d) 3 mm

Figure 4.32: Dependence of the total Nusselt number Nu_{total} and convective Nusselt number Nu_{conv} on the Reynolds number Re. Spatial averaging of the relevant quantities is performed over a cylindrical volume of radius $r = 6$ mm, with height of the cylinder above the wall surface equal to (a) 0.5 mm, (b) 1 mm, (c) 2 mm, and (d) 3 mm. Data points for the relation between Nu_{total} and Re are represented by circles, and those for the relation between Nu_{conv} and Re are represented by triangles. Meaning of symbol colours: Black = Case 1, Red = Case 2, Blue = Case 3.

for calculating Nu_{total}, Nu_{conv} and Re in Eqs. (4.49) - (4.51). It should be noted that in the present simulations, the reaction zones in the near wall region exist up to a height of 1 mm $\sim$ 2 mm above the wall surface.

Figure 4.32 illustrates the dependences of Nu_{total} and Nu_{conv} on Re by plotting the pairs of (Nu_{total}, Re) and (Nu_{conv}, Re) values calculated for each simulation case. The sub-figures (a) to (d) in Fig. 4.32 show the relation between Nu_{total} and Re,

as well as the relation between Nu_{conv} and Re, when spatial averaging of the quantities ρ, μ and T are performed using different heights of the imaginary cylindrical volume explained above. The solid lines represent the best fit lines for the correlation: $Nu_{total} = C_{total}Re^{n_{total}}$, while the dashed lines represent the best fit lines for the correlation: $Nu_{conv} = C_{conv}Re^{n_{conv}}$. Here, C_{total} and C_{conv} are the regression coefficients, and n_{total} and n_{conv} are the correlation indices of the respective correlations. It can be seen that the value of the correlation index n_{total} ranges from 0.48 to 0.50, indicating that n_{total} does not vary drastically depending on the height of the aforementioned cylindrical volume used for the spatial averaging of density ρ, dynamic viscosity μ and characteristic temperature T, in the near wall region. Considering the dependence of Nu_{conv} on Re in Fig. 4.32, as in the case of correlation index n_{total} (corresponding to the relation between Nu_{total} and Re), the correlation index n_{conv} corresponding to the relation between Nu_{conv} and Re, also does not show any significant variation depending on how the spatial averaging is performed in the near wall region, i.e., sub-figures (a) to (d) in Fig. 4.32. The value of n_{conv} ranges from 0.55 to 0.57. The regression coefficients (C_{total} and C_{conv}) and correlation indices (n_{total} and n_{conv}) of the best fit lines for the respective Nu - Re correlations, are summarised in Table 4.3 for the corresponding sub-figures in Fig. 4.32. From Fig. 4.32, the mean value of n_{total} is 0.49 and the mean value of n_{conv} is 0.56, indicating that the value of correlation index n_{total} is smaller than that of n_{conv}. The reason for this is that, Nu_{total} is calculated based on the total heat flux at the wall surface, which includes the contribution from the radiative heat flux as well. As described previously in Section 4.3.3.1, the radiative heat flow rates were nearly the same among all the three cases investigated in this study, which means that the average radiative heat flux at the wall surface is approximately constant regardless of Re. So, when a correlation of the form shown in Eq. (4.1) is applied to Nu_{total} and Re as in the previous experimental studies, the value of its correlation index n_{total} will deviate from the correlation index value defined in the conventional sense (i.e., for pure convection heat transfer). The extent to which the value of n_{total} deviates, will depend on the ratio of radiative heat flux to the total heat flux, which in turn depends on the

Table 4.3: Correlation indices and regression coefficients of the best fit lines for correlations: $Nu_{total} = C_{total}Re^{n_{total}}$ and $Nu_{conv} = C_{conv}Re^{n_{conv}}$ in Fig. 4.32.

Height above wall surface for averaging	Regression coefficients		Correlation indices	
	C_{total}	C_{conv}	n_{total}	n_{conv}
0.5 mm	4.143	1.479	0.49	0.56
1 mm	4.44	1.598	0.48	0.55
2 mm	3.934	1.434	0.49	0.56
3 mm	3.301	1.236	0.50	0.57

combustion conditions such as flame temperature, ambient pressure, fuel type, etc. Furthermore, the present value of correlation index $n_{total} = 0.49$ is not that far off from the value of $n = 0.4$ reported in the experiments by Inagaki et al. [15, 16]. Therefore, it becomes necessary to distinguish between the contributions of convective and radiative heat fluxes, if reliable correlations between Nu and Re are to be formulated.

4.4 Conclusions

In this study, a 3-D numerical analysis of *n*-dodecane wall impinging spray flames under CI engine-like conditions, was carried out to investigate the combustion characteristics, and the effect of fuel spray injection velocity on the wall heat flux (convective, radiant, and total heat fluxes). The dependence of wall heat flow rate (convective, radiative and total heat flow rates) on fuel injection velocity was also examined. The present simulations incorporated models for considering radiative heat transfer from soot and gas-phase species, and liquid fuel film formation on the wall surface. Additionally, Conjugate Heat Transfer (CHT) was also incorporated in the simulations for coupling the heat transfer occurring at the wall surface from the gas-phase (convective and radiative) and the liquid fuel film, with the heat conduction occurring inside the solid wall. Simulations were performed for three cases with fuel injection velocities of 100 m/s (Case 1), 150 m/s (Case 2) and 216 m/s (Case 3). The main findings of this research are as follows:

1. Total wall heat flux is largest in the vicinity of the stagnation point and reduces with increasing radial distance from the stagnation point in each case. This feature is consistent with that of the convective heat flux, which has the major contribution to the total wall heat flux, and is caused by the fact that the sweep and ejection events which characterize the turbulent heat transport near the wall surface, are largest near the stagnation point and decrease with increasing radial distance from the stagnation point in each case. Furthermore, the convective heat flux (and hence the total wall heat flux) increases with the fuel injection velocity, because with increasing fuel injection velocity, these sweep and ejection events become more frequent and enhance the convective heat flux.

2. Radiative heat flux at the wall surface becomes larger as the radial distance from the stagnation point increases in all the cases, because the flame temperature increases with increasing radial distance from the stagnation point in each case. The influence of fuel injection velocity on the radiative heat flow rate is found to be

rather insignificant. This is due to the fact that the radiative heat flux is determined by the flame temperature, and the flame temperature is not significantly affected by the fuel injection velocity among the three cases. However, because the total heat flow rate increases with the fuel injection velocity, the ratio of radiative heat flow rate to the total heat flow rate decreases from 29.7% in Case 1 to 18.1% in Case 3, meaning this ratio decreases with increasing fuel injection velocity.

3. The contribution of radiative heat flow rate to the total heat flow rate is non-negligible for the conditions under which each case is simulated. So, when the average total wall heat flux is used for constructing a correlation between Nu and Re of the form $Nu \propto Re^n$ (based on the principle of convective heat transfer), corresponding to heat loss through the wall, the value of its correlation index n will be different from that of the conventional Nu - Re correlation applicable for pure convection heat transfer. Therefore, it is necessary to clearly distinguish between the contributions of convective and radiative heat flow rates, in order to construct a robust correlation between Nu and Re that can be used for calculating the heat transfer coefficient accurately.

This work has investigated the dependence of heat loss through the wall on fuel injection velocity (and hence the fuel injection pressure), and attempted to elucidate the relation between Nusselt number Nu and Reynolds number Re relating to wall heat transfer during spray flame-wall interaction process. However, there are several other parameters which influence the wall heat loss in CI engines, such as fuel temperature at injection, spray nozzle diameter, impingement distance and fuel spray impingement angle, radiative properties of the wall surface, bore size, operating pressure and temperature, etc. In order to develop robust and improved correlations between Nu and Re that take into to account the influences of the aforementioned parameters on wall heat transfer, much more work is needed. Such correlations can be used for accurate predictions of the heat transfer coefficient in CI engines, which will have strong implications on designing low-emission CI engines with better thermal efficiencies. The above issues are open questions in the fields of thermal, combustion, fluid and automotive engineering,

and researches pertaining to these issues will form part of our future work. With the ever-increasing capabilities of computing resources around the world, the application of numerical simulation tools such as Large-Eddy Simulation (LES) and Direct Numerical Simulation (DNS), open up new possibilities for investigating various mechanisms associated with complex spray combustion problems involving flame-wall interactions in detail. One aspect that is integral to spray combustion problems and of particular interest to the combustion engineering community, is the liquid atomization process. The computational cost of accurately reproducing fuel atomization process (both primary and secondary atomization) using fully-resolved simulations has been quite prohibitive until now. Moreover, for precise evaluation of the effects of spray nozzle parameters, fuel injection pressure, etc. on liquid fuel atomization and spray combustion itself, the use of presumed droplet size distribution PDFs or even existing liquid atomization/breakup models may not be adequate for certain applications. Therefore, numerical simulations of spray combustion incorporating well-resolved methods that can accurately capture the physics of liquid atomization process are strongly desired. Such simulations will soon be possible by using recently developed state-of-the-art supercomputers. Findings from these numerical investigations will no doubt complement those of experimental studies which are ever so indispensable, and will be essential for addressing challenges related to energy-efficiency, pollution and CO_2 emissions control.

References

[1] United Nations Environment Programme, 2019.

[2] United Nations Framework Convention on Climate Change, 2015.

[3] International Energy Agency, 2015.

[4] Annual Energy Outlook 2015 with projections to 2040. *U.S. Energy Information Administration*, DOE/EIA–0383(2015), 2015.

[5] International Organization of Motor Vehicle Manufacturers, 2019.

[6] J. B. Heywood. *Internal Combustion Engine Fundamentals*. McGraw-Hill Inc., London, 1988.

[7] G. Eichelberg. Some new investigations on old combustion engine problems. *Engineering*, 148:446–463, 1939.

[8] T. Oguri. On the coefficient of heat transfer between gases and cylinder walls of the spark-ignition engine. *Bulletin of JSME*, 3:363–369, 1960.

[9] W. J. D. Annand. Heat transfer in the cylinders of reciprocating internal combustion engines. *Proceedings of the Institution of Mechanical Engineers*, 177:973–990, 1963.

[10] G. Woschni. A universally applicable equation for the instantaneous heat transfer coefficient in the internal combustion engine. In *SAE Technical Paper*. SAE International, 02 1967.

[11] G. Sitkei and G. V. Ramanaiah. A rational approach for calculation of heat transfer in diesel engines. In *SAE Technical Paper*. SAE International, 02 1972.

[12] G. F. Hohenberg. Advanced approaches for heat transfer calculations. In *SAE Technical Paper*. SAE International, 02 1979.

[13] M. S. Lounici, K. Loubar, M. Balistrou, and M. Tazerout. Investigation on heat transfer evaluation for a more efficient two-zone combustion model in the case of natural gas si engines. *Applied Thermal Engineering*, 31:319–328, 2011.

[14] F. Baldi, G. Theotokatos, and K. Andersson. Development of a combined mean value–zero dimensional model and application for a large marine four-stroke diesel engine simulation. *Applied Energy*, 154:402 – 415, 2015.

[15] K. Inagaki, J. Mizuta, and T. Hashizume. Theoretical study on spray design for small-bore-size diesel engines (fourth report). *Transactions of Society of Automotive Engineers of Japan*, 47:1297–1303 (in Japanese), 2016.

[16] K. Inagaki, J. Mizuta, Y. Nomura, T. Ikedo, and R. Ueda. Proposal of wall heat transfer coefficient applicable to spray-wall interaction process in diesel engines. *Transactions of Society of Automotive Engineers of Japan*, 49:1120–1125 (in Japanese), 2018.

[17] R. Mahmud, T. Kurisu, K. Nishida, Y. Ogata, J. Kanzaki, and O. Akgol. Effects of injection pressure and impingement distance on flat-wall impinging spray flame and its heat flux under diesel engine-like condition. *Advances in Mechanical Engineering*, 11:1–15, 2019.

[18] J. Yan and G. Borman. A new instrument for radiation flux measurement in diesel engines. *SAE Transactions*, 1862–1877, 1989.

[19] W. K. Melville and K. N. C. Bray. The two-phase turbulent jet. *International Journal of Heat and Mass Transfer*, 22:279 – 287, 1979.

[20] W. K. Melville and K. N. C. Bray. A model of the two-phase turbulent jet. *International Journal of Heat and Mass Transfer*, 22:647 – 656, 1979.

[21] M. Zhu, K. N. C. Bray, O. Rumberg, and B. Rogg. PDF transport equations for two-phase reactive flows and sprays. *Combustion and Flame*, 122:327 – 338, 2000.

[22] T. Kitano, J. Nishio, R. Kurose, and S. Komori. Effects of ambient pressure, gas temperature and combustion reaction on droplet evaporation. *Combust. Flame*, 161(2):551–564, 2014.

[23] T. Kitano, J. Nishio, R. Kurose, and S. Komori. Evaporation and combustion of multicomponent fuel droplets. *Fuel*, 136:219–225, 2014.

[24] T. Kitano, K. Kaneko, R. Kurose, and S. Komori. Large-eddy simulations of gas– and liquid–fueled combustion instabilities in back-step flows. *Combustion and Flame*, 170:63–78, 2016.

[25] Y. Hu and R. Kurose. Nonpremixed and premixed flamelets LES of partially premixed spray flames using a two-phase transport equation of progress variable. *Combustion and Flame*, 188:227–242, 2018.

[26] A. L. Pillai and R. Kurose. Numerical investigation of combustion noise in an open turbulent spray flame. *Applied Acoustics*, 133:16–27, 2018.

[27] Y. Haruki, A. L. Pillai, T. Kitano, and R. Kurose. Numerical investigation of flame propagation in fuel droplet arrays. *Atomization and Sprays*, 28:357–388, 2018.

[28] Y. Hu and R. Kurose. Large-eddy simulation of turbulent autoigniting hydrogen lifted jet flame with a multi-regime flamelet approach. *Int. J. Hydrog. Energy*, 44(12):6313–6324, 2019.

[29] A. L. Pillai and R. Kurose. Combustion noise analysis of a turbulent spray flame using a hybrid DNS/APE-RF approach. *Combustion and Flame*, 200:168 – 191, 2019.

[30] C. T. d'Auzay, U. Ahmed, A. L. Pillai, N. Chakraborty, and R. Kurose. Statistics of progress variable and mixture fraction gradients in an open turbulent jet spray flame. *Fuel*, 247:198–208, 2019.

[31] Y. Hu, R. Kai, R. Kurose, E. Gutheil, and H. Olguin. Large eddy simulation of a partially pre-vaporized ethanol reacting spray using the multiphase DTF/flamelet model. *International Journal of Multiphase Flow*, 125:103216, 2020.

[32] A. L. Pillai, J. Nagao, R. Awane, and R. Kurose. Influences of liquid fuel atomization and flow rate fluctuations on spray combustion instabilities in a backward-facing step combustor. *Combustion and Flame*, 220:337 – 356, 2020.

[33] J. Nagao, A. L. Pillai, and R. Kurose. Investigation of temporal variation of combustion instability intensity in a back step combustor using LES. *Journal of Thermal Science and Technology*, 15:JTST0036–JTST0036, 2020.

[34] S. Malkeson, U. Ahmed, A. Pillai, N. Chakraborty, and R. Kurose. Evolution of surface density function in an open turbulent jet spray flame. *Flow, Turbulence and Combustion*, 106:207–229, 2021.

[35] S. Malkeson, U. Ahmed, C. Turquand d'Auzay, A. Pillai, N. Chakraborty, and R. Kurose. Displacement speed statistics in an open turbulent jet spray flame. *Fuel*, 286:119242, 2021.

[36] J. Wen, Y. Hu, A. Nakanishi, and R. Kurose. Atomization and evaporation process of liquid fuel jets in crossflows: A numerical study using eulerian/lagrangian method. *International Journal of Multiphase Flow*, 129:103331, 2020.

[37] Z. Yuan, J. Wen, M. Matsumoto, and R. Kurose. Anti-wetting ability of the hydrophobic surface decorated by submillimeter grooves. *International Journal of Multiphase Flow*, 131:103404, 2020.

[38] Z. Yuan, M. Matsumoto, and R. Kurose. Directional migration of an impinging droplet on a surface with wettability difference. *Phys. Rev. Fluids*, 5:113605, Nov 2020.

[39] C. S. Chang, Y. Zhang, K. N. C. Bray, and B. Rogg. Modelling and simulation of autoignition under simulated diesel-engine conditions. *Combustion Science and Technology*, 113:205–219, 1996.

[40] M. Zhu, K. N. C. Bray, and B. Rogg. PDF modelling of spray autoignition in high pressure turbulent flows. *Combustion Science and Technology*, 120:357–379, 1996.

[41] F. P. Kärrholm, F. Tao, and N. Nordin. Three-dimensional simulation of diesel spray ignition and flame lift-off using OpenFOAM and KIVA-3V CFD codes. In *SAE Technical Paper*. SAE International, 04 2008.

[42] F. Bottone, A. Kronenburg, D. Gosman, and A. Marquis. The numerical simulation of diesel spray combustion with LES-CMC. *Flow, Turbulence and Combustion*, 89:651 – 673, 2012.

[43] J. Tillou, J.-B. Michel, C. Angelberger, and D. Veynante. Assessing LES models based on tabulated chemistry for the simulation of diesel spray combustion. *Combustion and Flame*, 161:525 – 540, 2014.

[44] Y. Pei, S. Som, E. Pomraning, P. K. Senecal, S. A. Skeen, J. Manin, and L. M. Pickett. Large eddy simulation of a reacting spray flame with multiple realizations under compression ignition engine conditions. *Combustion and Flame*, 162:4442 – 4455, 2015.

[45] T. Hori, K. Fujiwara, M. Tsubokura, K. Kuwahara, E. Matsumura, and J. Senda. Three-dimensional simulation of heat transfer in diesel-spray flame impinging on flat wall using skeletal mechanism of n-tridecane. *The Proceedings of the International symposium on diagnostics and modeling of combustion in internal combustion engines*, 2017.9:B107, 2017.

[46] K. M. Pang, M. Jangi, X.-S. Bai, J. Schramm, J. H. Walther, and P. Glarborg. Effects of ambient pressure on ignition and flame characteristics in diesel spray combustion. *Fuel*, 237:676 – 685, 2019.

[47] B. Tekgül, H. Kahila, O. Kaario, and V. Vuorinen. Large-eddy simulation of dual-fuel spray ignition at different ambient temperatures. *Combustion and Flame*, 215:51 – 65, 2020.

[48] K. N. C. Bray, M. Champion, and P. A. Libby. Premixed flames in stagnating turbulence part III—the k - ϵ theory for reactants impinging on a wall. *Combustion and Flame*, 91:165 – 186, 1992.

[49] A. S. Wu and K. N. C. Bray. Application of a coherent flame model to premixed turbulent combustion impinging on a wall. *Combustion Science and Technology*, 113:367–392, 1996.

[50] K. Bray, M. Champion, and P. A. Libby. Premixed flames in stagnating turbulence part II. The mean velocities and pressure and the Damköhler number. *Combustion and Flame*, 112:635 – 653, 1998.

[51] Y. Zhang, K. N. C. Bray, and B. Rogg. Temporally and spatially resolved investigation of flame propagation and extinction in the vicinity of walls. *Combustion Science and Technology*, 113:255–271, 1996.

[52] E. J. Stevens, K. N. C. Bray, and B. Lecordier. Velocity and scalar statistics for premixed turbulent stagnation flames using PIV. *Symposium (International) on Combustion*, 27:949 – 955, 1998. Twenty-Seventh Sysposium (International) on Combustion Volume One.

[53] Y. Zhang and K. N. C. Bray. Characterization of impinging jet flames. *Combustion and Flame*, 116:671 – 674, 1999.

[54] P. Pantangi, A. Sadiki, J. Janicka, M. Mann, and A. Dreizler. LES of premixed methane flame impinging on the wall using non-adiabatic flamelet generated manifold (FGM) approach. *Flow, Turbulence and Combustion*, 92:805–836, 2014.

[55] U. Ahmed, N. A. K. Doan, J. Lai, M. Klein, N. Chakraborty, and N. Swaminathan. Multiscale analysis of head-on quenching premixed turbulent flames. *Physics of Fluids*, 30:105102, 2018.

[56] P. Zhao, L. Wang, and N. Chakraborty. Analysis of the flame-wall interaction in premixed turbulent combustion. *Journal of Fluid Mechanics*, 848:193–218, 2018.

[57] R. Kai, R. Masuda, T. Ikedo, and R. Kurose. Conjugate heat transfer analysis of methane/air premixed flame – wall interaction: A study on effect of wall material. *Applied Thermal Engineering*, 181:115947, 2020.

[58] R. Kai, A. Takahashi, and R. Kurose. Numerical investigations of C1-C3 alkanes and H_2 premixed flame-wall interaction: Effectiveness of insulation wall on heat loss reduction. *Journal of Thermal Science and Technology*, 15:JTST0033–JTST0033, 2020.

[59] I. Konstantinou, U. Ahmed, and N. Chakraborty. Effects of fuel lewis number on the near-wall dynamics for statistically planar turbulent premixed flames impinging on inert cold walls. *Combustion Science and Technology*, 193:235–265, 2021.

[60] R. S. Miller, K. Harstad, and J. Bellan. Evaluation of equilibrium and non-equilibrium evaporation models for many-droplet gas-liquid flow simulations. *International Journal of Multiphase Flow*, 24:1025–1055, 1998.

[61] H. Moriai, R. Kurose, H. Watanabe, Y. Yano, F. Akamatsu, and S. Komori. Large-eddy simulation of turbulent spray combustion in a subscale aircraft jet engine combustor-predictions of no and soot concentrations. *J. Eng. Gas Turbines Power*, 135:091503, 2013.

[62] A. Kishimoto, H. Moriai, K. Takenaka, T. Nishiie, M. Adachi, A. Ogawara, and R. Kurose. Application of a nonadiabatic flamelet/progress-variable approach to large-eddy simulation of H2/O2 combustion under a pressurized condition. *J. Heat Transfer*, 139:124501, 2017.

[63] H. Pitsch. FlameMaster: A C++ computer program for 0D combustion and 1D laminar flame calculations. *Cited in*, 81, 1998.

[64] K. Narayanaswamy, P. Pepiot, and H. Pitsch. A chemical mechanism for low to high temperature oxidation of n-dodecane as a component of transportation fuel surrogates. *Combustion and Flame*, 161:866–884, 2014.

[65] R. S. Miller and J. Bellan. Direct numerical simulation of a confined three-dimensional gas mixing layer with one evaporating hydrocarbon-droplet laden stream. *Journal of Fluid Mechanics*, 384:293–338, 1999.

[66] W. E. Ranz and W. R. Marshall. Evaporation from drops: Part I. *Chemical Engineering Progress*, 48:141–146, 1952.

[67] W. E. Ranz and W. R. Marshall. Evaporation from drops : Part II. *Chemical Engineering Progress*, 48:173–180, 1952.

[68] R. Kurose, H. Makino, S. Komori, M. Nakamura, F. Akamatsu, and M. Katsuki. Effects of outflow from the surface of a sphere on drag, shear lift, and scalar diffusion. *Phys. Fluids*, 15(8):2338–2351, 2003.

[69] M. Nakamura, F. Akamatsu, R. Kurose, and M. Katsuki. Combustion mechanism of liquid fuel spray in a gaseous flame. *Phys. Fluids*, 17(12):123301, 2005.

[70] J. Bellan and M. Summerfield. Theoretical examination of assumptions commonly used for the gas phase surrounding a burning droplet. *Combust. Flame*, 33:107–122, 1978.

[71] J. Bellan and K. Harstad. Analysis of the convective evaporation of nondilute clusters of drops. *International Journal of Heat and Mass Transfer*, 30:125–136, 1987.

[72] C. T. Crowe, M. P. Sharma, and D. E. Stock. The Particle-Source-In Cell (PSI-Cell) model for gas-droplet flows. *J. Fluids Eng.*, 99:325–332, 1977.

[73] K. Luo, O. Desjardins, and H. Pitsch. DNS of droplet evaporation and combustion in a swirling combustor. In *Annual Research Briefs*. Center for Turbulence Research, NASA Ames/Stanford University, 2008.

[74] K. Luo, H. Pitsch, M. G. Pai, and O. Desjardins. Direct numerical simulations and analysis of three-dimensional n-heptane spray flames in a model swirl combustor. *Proc. Combust. Inst.*, 33:2143–2152, 2011.

[75] G. Borghesi, E. Mastorakos, and R. S. Cant. Complex chemistry DNS of n-heptane spray autoignition at high pressure and intermediate temperature conditions. *Combustion and Flame*, 160:1254 – 1275, 2013.

[76] Y. Wang and C. Rutland. Direct numerical simulation of ignition in turbulent n-heptane liquid-fuel spray jets. *Combustion and Flame*, 149:353 – 365, 2007.

[77] F. Mashayek. Numerical investigation of reacting droplets in homogeneous shear turbulence. *Journal of Fluid Mechanics*, 405:1–36, 2000.

[78] D. W. Stanton and C. J. Rutland. Modeling fuel film formation and wall interaction in diesel engines. *SAE transactions*, 808–824, 1996.

[79] P. J. O'Rourke and A. A. Amsden. A particle numerical model for wall film dynamics in port-injected engines. *SAE transactions*, 2000–2013, 1996.

[80] P. J. O'Rourke and A. A. Amsden. A spray/wall interaction submodel for the KIVA-3 wall film model. *SAE transactions*, 281–298, 2000.

[81] S. Tanguy, T. Ménard, and A. Berlemont. A level set method for vaporizing two-phase flows. *Journal of Computational Physics*, 221:837 – 853, 2007.

[82] W. A. Fiveland. Discrete-ordinates solutions of the radiative transport equation for rectangular enclosures. *J. Heat Transfer*, 106:699–706, 1984.

[83] L. Rothman, I. Gordon, R. Barber, H. Dothe, R. Gamache, A. Goldman, V. Perevalov, S. Tashkun, and J. Tennyson. HITEMP, the high-temperature

molecular spectroscopic database. *Journal of Quantitative Spectroscopy and Radiative Transfer*, 111:2139–2150, 2010.

[84] M. Chmielewski and M. Gieras. Planck mean absorption coefficients of H_2O, CO_2, CO and NO for radiation numerical modeling in combusting flows. *Journal of Power Technologies*, 95:97–104, 2015.

[85] D. Byun and S. W. Baek. Numerical investigation of combustion with non-gray thermal radiation and soot formation effect in a liquid rocket engine. *Int. J. Heat Mass Transfer*, 50:412–422, 2007.

[86] S. Brookes and J. Moss. Predictions of soot and thermal radiation properties in confined turbulent jet diffusion flames. *Combustion and Flame*, 116:486–503, 1999.

[87] H. Watanabe, R. Kurose, S. Komori, and H. Pitsch. Effects of radiation on spray flame characteristics and soot formation. *Combust. Flame*, 152:2–13, 2008.

[88] M. Muto, K. Yuasa, and R. Kurose. Numerical simulation of soot formation in pulverized coal combustion with detailed chemical reaction mechanism. *Advanced Powder Technology*, 29:1119 – 1127, 2018.

[89] R. J. Hall, M. D. Smooke, and M. B. Colket. Predictions of soot dynamics in opposed jet diffusion flames. *F. L. Dryer, R. F. Sawyer (Eds.), Physical and Chemical Aspects of Combustion: A Tribute to Irvin Glassman, Gordon and Breach, Amsterdam*, 4:189–230, 1997.

[90] K. Inagaki, J. Mizuta, T. Hashizume, and T. Tomoda. Theoretical study on spray design for small-bore-size diesel engines (second report). *Transactions of Society of Automotive Engineers of Japan*, 47:31–37 (in Japanese), 2016.

[91] H. Hiroyasu. Fuel spray penetration and spray angle in diesel engines. *Transactions of the Society of Automotive Engineers of Japan, Inc.*, 21:5–11 (in Japanese), 1980.

[92] P. Rosin and E. Rammler. The laws governing the fineness of powdered coal. *Journal of the Institute of Fuel*, 7:29–36, 1933.

[93] R. Kurose. FK^3, http://www.tse.me.kyoto-u.ac.jp/members/kurose/link_e.php, 2020.

[94] V. Moureau, C. Bérat, and H. Pitsch. An efficient semi-implicit compressible solver for large-eddy simulations. *Journal of Computational Physics*, 226(2):1256–1270, 2007.

[95] Y. Morinishi, T. Lund, O. Vasilyev, and P. Moin. Fully conservative higher order finite difference schemes for incompressible flow. *Journal of Computational Physics*, 143:90 – 124, 1998.

[96] G.-S. Jiang and C.-W. Shu. Efficient implementation of weighted ENO schemes. *J. Comput. Physics*, 126:202–228, 1996.

[97] R. J. Kee, G. Dixon-Lewis, J. Warnatz, M. E. Coltrin, and J. A. Miller. A Fortran computer code package for the evaluation of gas-phase multicomponent transport properties. *Sandia National Laboratories Report SAND86-8246*, 1986.

[98] R. J. Kee, F. M. Rupley, and J. A. Miller. Chemkin-II: A Fortran chemical kinetics package for the analysis of gas-phase chemical kinetics. *Sandia National Laboratories Report SAND89-8009*, 1989.

[99] National Institute of Standards and Technology Webbook. https://webbook.nist.gov/chemistry/fluid/.

[100] J. J. Valencia and P. N. Quested. *Thermophysical Properties*, volume 22B. ASM International, 2010.

[101] U. Ahmed, A. L. Pillai, N. Chakraborty, and R. Kurose. Statistical behavior of turbulent kinetic energy transport in boundary layer flashback of hydrogen-rich premixed combustion. *Phys. Rev. Fluids*, 4:103201, Oct 2019.

[102] K. Luo, T. Jin, S. Lu, and J. Fan. DNS analysis of a three-dimensional supersonic turbulent lifted jet flame. *Fuel*, 108:691–698, 2013.

[103] S. B. Pope. *Turbulent flows*. Cambridge University Press, UK, 2000.

[104] H. Hattori and Y. Nagano. Direct numerical simulation of turbulent heat transfer in plane impinging jet. *International Journal of Heat and Fluid Flow*, 25:749–758, 2004.

[105] T. Oguri and S. Inaba. Radiant heat transfer in diesel engines. *SAE Transactions*, 81:127–147, 1972.

[106] C. R. Ferguson and A. T. Kirkpatrick. *Internal Combustion Engines: Applied Thermosciences*. John Wiley & Sons, West Sussex, United Kingdom, 2015.

Nomenclature

B_M	: Mass transfer number [-]	Q_2	: Second invariant of
C	: Progress variable [-]		velocity gradient tensor [$1/s^2$]
c	: Heat capacity [J/(K kg)]	q	: Heat flux [W/m^2]
c_p	: Specific heat capacity	Re	: Reynolds number [-]
	at constant pressure [J/(K kg)]	r	: Radius [m]
c_v	: Specific heat capacity	S	: Evaporation source term
	at constant volume [J/(K kg)]	Sc	: Schmidt number [-]
D	: Diffusion coefficient [m^2/s]	Sh	: Sherwood number [-]
D_n	: Nozzle diameter [m]	T	: Temperature [K]
d	: Droplet diameter [m]	t	: Time [s]
E_{soot}	: Soot radiation emission [W/m^2]	t_η	: Kolmogorov time scale [s]
e	: Specific internal energy [J/kg]	$\boldsymbol{u}$	: Velocity [m/s]
f_1	: Correction of Stokes drag [-]	W	: Molecular Mass [kg/mol]
f_2	: Correction of heat transfer [-]	We	: Weber number [-]
$\boldsymbol{g}$	: Gravitational acceleration [m/s2]	Y	: Mass fraction [-]
H	: Channel half height [m]	X	: Mole fraction [-]
h	: Specific enthalpy [J/kg]	Z	: Mixture fraction [-]
h_{heat}	: Heat transfer coefficient [W/ (m^2 K)]	γ	: Surface tension [kg/s^2]
I	: Spectral radiation intensity [W/(m^2 sr)]	Δh	: Enthalpy loss [J/kg]
L_V	: Latent heat [J/kg]	ϵ	: dissipation rate of
m	: Mass [kg]		turbulent kinetic energy [m^2/s^3]
Nu	: Nusselt number [-]	η	: Kolmogorov length scale [m]
$\boldsymbol{n}$	: Wall normal vector [-]	θ	: Spray cone angle [$^\circ$]
n	: Correlation index [-]	κ	: Planck mean
P	: Pressure [Pa]		absorption coefficient [1/m]
Pr	: Prandtl number [-]	λ	: Thermal conductivity [W/(m K)]
Q_{rad}	: Radiative heat source [W/kg]	μ	: Viscosity [Pa s]
Q_w	: Wall heat flow rate [W]	ν	: Kinematic viscosity [m^2/s]

Nomenclature

ρ	: Density [kg/m^3]	F	: Fuel
σ	: Stefan-Boltzmann constant [W/(m^2 K^4)]	g	: Gas
$\boldsymbol{\tau}$	: Viscous stress tensor [kg/(m^2 s^2)]	imp	: Impingement of droplet
τ	: Response time [s]	inj	: Injection
τ_{ig}	: Ignition delay time [s]	vap	: Film evaporation
Ω	: Solid angle [sr]	l	: Liquid film
$\dot{\omega}$	: Reaction rate [1/s]	p	: Film particle
		rad	: Radiation
Subscripts		s	: Solid wall
C	: Progress variable	$total$	: Total value
b	: Blackbody	w	: Wall
$conv$	: Convection	λ	: Wavelength λ
d	: Droplet		

Chapter 5

Conclusions

5.1 Summary and conclusions

To investigate the FWI characteristics of laminar premixed flames, turbulent premixed flames, and turbulent spray flames, numerical simulations were performed without any turbulence model. To investigate the influence of wall material on the premixed FWI, one- and two-dimensional numerical simulations of premixed flames were performed incorporating conjugate heat transfer. In addition to these numerical simulations, to investigate the turbulent FWI, DNS of premixed flame in a turbulent channel flow and DNS of spray flames impinging on the wall were performed.

In Chapter 2, the characteristics of the reduction in wall heat loss by heat insulation wall were described. The effects of fuel properties (C1 to C3 alkanes and H_2), equivalence ratios ($\phi = 0.6$, 0.8, 1.0, and 1.2), and ambient pressure conditions (1, 2, and 4 MPa) on the reduction in wall heat loss were investigated by one- and two-dimensional numerical simulations of propagating premixed flames incorporating conjugate heat transfer. For the simulations to investigate the effects of fuel and equivalence ratio, the detailed chemical reaction mechanisms that consider 70 chemical species and 321 reactions for alkane combustion [1], and 9 chemical species and 19 reactions for the H_2 combustion [2] were used. For the simulations to investigate the effect of pressure, a two-step global reaction model [3] was used to calculate the methane reaction. Numerical results reveal

the following:

1. For all the alkanes and H_2 flames, the temperature at the surface of the insulation wall increased more and faster than that of the Al alloy wall, and the heat loss through the wall was reduced by the insulation.

2. The heat loss reduction rate for the insulation wall to the Al alloy wall Λ became higher with both increase and decrease in the equivalence ratio from the stoichiometric ratio, regardless of the fuel. The insulation worked more efficiently under higher pressure condition. The value of Λ reached up to 2.1%, and this order matched well with the existing experiment. The reason for this tendency of Λ against the equivalence ratio was explicitly explained by the time variations of the gas thermal conductivity and the gas temperature gradient in the vicinity of the wall, which controlled the heat flux through the wall.

In Chapter 3, the statistical behavior of the near-wall surface density function in a turbulent channel flow was described. A three-dimensional DNS of turbulent premixed V-flame interacting with an isothermal inert wall in the wall-bounded turbulent channel flow at $Re_\tau = 395$ for the stoichiometric CH_4-air flame was performed. For the calculation of the reactions, a two-step global reaction model [3] was used. Numerical results reveal the following:

1. The streamwise vortices strongly affected the flame behavior near the wall. The sweep enhanced flame propagation toward the wall, and the ejection raised unburnt gas away from the wall.

2. The mean value of SDF in the outer layer (at $y^+ = 71$) in progress variable space matched with that of one-dimensional laminar planar flame, whereas the mean values of SDF in the buffer layer (at $y^+ = 20$) and viscous sublayer (at $y^+ = 0.6$) were almost 90% and 10% of that of the planar flame, respectively. In all three layers, the local mean value of SDF has been found to decrease in the downstream direction.

3. The mean value of effective normal strain rate a_n^{eff} $(= \boldsymbol{n} \cdot \nabla S_d + a_n)$, whose increase tends to decrease the value of SDF, was much higher at $y^+ = 0.6$ than those at $y^+ = 71$ and 21. This meant that the SDF steeply decreased in the viscous sublayer. In the viscous sublayer, the contribution of the gradient of displacement speed in flame-normal direction $\boldsymbol{n} \cdot \nabla S_d$ to the normal strain rate a_n^{eff} was more dominant than that of normal strain rate a_n. This tendency was qualitatively similar to the analysis of the previous study for $Re_\tau = 110$ [4], however the maximum value of a_n^{eff} for $Re_\tau = 395$ was approximately twice that for $Re_\tau = 110$.

In Chapter 4, the FWI for the spray flame impinging to the wall was described. The relationship between Re and Nu was investigated using DNS of n-dodecane spray flame impinging on the wall for different injection velocity u_{inj} conditions. As a turbulent combustion model, a non-adiabatic flamelet progress variable (NA-FPV) approach [5] was employed. For the generation of the flamelet database, the detailed chemical reaction mechanism consisting 255 chemical species and 2289 reactions [6] was considered to represent n-dodecane reaction. Numerical results reveal the following:

1. Total wall heat flux was largest in the vicinity of the stagnation point in each case. This feature was consistent with that of the convective heat flux, which had the major contribution to the total wall heat flux, and was caused by the fact that the sweep and ejection events were largest near the stagnation point in each case. Furthermore, the convective heat flux increased with u_{inj}, because with increasing u_{inj}, these sweep and ejection events became more frequent.

2. Radiative heat flux at the wall surface became larger as the radial distance from the stagnation point r increased in all the cases, because the flame temperature T increased with increasing r in each case. The influence of u_{inj} on the radiative heat flow rate was found to be rather insignificant. This was due to the fact that the radiative heat flux was determined by T, and the T was not significantly affected by u_{inj} among the three cases. However, because the total heat flow rate increased with the u_{inj}, the ratio of radiative heat flow rate to the total heat flow rate

decreased from 29.7% in Case 1 to 18.1% in Case 3, meaning this ratio decreased with increasing u_{inj}.

3. The contribution of radiative heat flow rate to the total heat flow rate was non-negligible for the conditions under which each case is simulated. So, when the average total wall heat flux was used for constructing a correlation between Nu and Re of the form $Nu \propto Re^n$, the value of its correlation index n was different from that of the conventional Nu - Re correlation applicable for pure convection heat transfer. Therefore, it is necessary to clearly distinguish between the contributions of convective and radiative heat flow rates.

5.2 Suggestions for future research

Conducting research into the following areas could extend the progress made in the current study.

1. In Chapter 2, the reduction in the wall heat flux by the insulation wall was investigated for various fuel compositions under various pressure conditions by performing one- and two-dimensional simulations. To further understand the effect of the insulation wall on the wall heat flux in actual IC engines, it is important to investigate the cycle-to-cycle variation of wall heat flux and temperature distribution in an actual combustor configuration.

2. In Chapter 3, the statistical behavior of the near-wall surface density function (SDF) in a turbulent channel flow was investigated by performing a three-dimensional DNS of turbulent premixed V-flame interacting with an isothermal inert wall in a wall-bounded turbulent channel flow at $Re_\tau = 395$ for the stoichiometric CH_4-air flame . However, the statistical behavior of the SDF was qualitatively similar to that at $Re_\tau = 110$, contrary to expectation. Therefore, numerical analysis for higher Re_τ values is required to investigate the flame quenching due to turbulence in the vicinity of the wall. Moreover, in the present DNS, the preferential diffusion effect was neglected and simple reaction model was used. Performing DNS considering the preferential diffusion effect employing the detailed chemical reaction mechanism is also future task. Further investigations focusing on H_2 flames, whose near-wall reaction characteristics are different from methane flame, is also future work.

3. In Chapter 4, the dependence of heat loss through the wall on fuel injection velocity, and attempted to elucidate the relation between the Nusselt number Nu and Reynolds number Re relating to wall heat transfer during spray FWI process was investigated by performing three-dimensional DNS of spray flame impinging on the wall. However, there are several other parameters which influence the wall

heat loss in CI engines, such as fuel temperature at injection, spray nozzle diameter, impingement distance and fuel spray impingement angle, radiative properties of the wall surface, bore size, operating pressure, and temperature, etc. In order to develop robust and improved correlations between Nu and Re that take into to account the influences of the aforementioned parameters on wall heat transfer, much more work is needed. Such correlations can be used for accurate predictions of the heat transfer coefficient in CI engines, which will have strong implications on designing low-emission CI engines with better thermal efficiencies.

References

[1] "chemical-kinetic mechanisms for combustion applications", san diego mechanism web page, mechanical and aerospace engineering (combustion research), university of california at san diego.

[2] M. Ó Conaire, H. J. Curran, J. M. Simmie, W. J. Pitz, and C. K. Westbrook. A comprehensive modeling study of hydrogen oxidation. *International journal of chemical kinetics*, 36(11):603–622, 2004.

[3] B. Franzelli, E. Riber, M. Sanjosé, and T. Poinsot. A two-step chemical scheme for kerosene–air premixed flames. *Combustion and Flame*, 157(7):1364–1373, 2010.

[4] U. Ahmed, N. Chakraborty, and M. Klein. Scalar gradient and strain rate statistics in oblique premixed flame–wall interaction within turbulent channel flows. *Flow, Turbulence and Combustion*, 106(2):701–732, 2021.

[5] A. Kishimoto, H. Moriai, K. Takenaka, T. Nishiie, M. Adachi, A. Ogawara, and R. Kurose. Application of a nonadiabatic flamelet/progress-variable approach to large-eddy simulation of H2/O2 combustion under a pressurized condition. *J. Heat Transfer*, 139:124501, 2017.

[6] K. Narayanaswamy, P. Pepiot, and H. Pitsch. A chemical mechanism for low to high temperature oxidation of n-dodecane as a component of transportation fuel surrogates. *Combustion and Flame*, 161:866–884, 2014.